Universidade de São Paulo
Instituto de Física

# Reconstrução da matriz de covariância de luz não-clássica gerada em oscilador paramétrico óptico em *chip*

Roger Alfredo Kögler

Orientador: Prof. Dr. Paulo Alberto Nussenzveig

Tese de doutorado apresentada ao Instituto de Física da Universidade de São Paulo, como requisito parcial para a obtenção do título de Doutor(a) em Ciências.

Prof. Dr. Paulo Alberto Nussenzveig (IFUSP)
Prof. Dr. Gabriel Teixeira Landi (IFUSP)
Prof. Dr. Ben Hur Viana Borges (EESC USP)
Prof. Dr. Felippe Alexandre Silva Barbosa (UNICAMP)
Prof. Dr. Sebastião José Nascimento de Pádua (UFMG)

São Paulo
2022

**FICHA CATALOGRÁFICA**
**Preparada pelo Serviço de Biblioteca e Informação**
**do Instituto de Física da Universidade de São Paulo**

Kögler, Roger Alfredo

Reconstrução da matriz de covariância de luz não-clássica gerada em oscilador paramétrico óptico em chip / Covariance matrix reconstruction of nonclassical light generated in an on-chip optical parametric oscillator São Paulo, 2022.

Tese (Doutorado) – Universidade de São Paulo. Instituto de Física. Depto. de Física Experimental.

Orientador: Prof. Dr. Paulo Alberto Nussenzveig

Área de Concentração: Óptica

Unitermos: 1. Física experimental; 2. Óptica quântica; 3. Óptica não-linear; 4. Informação quântica

USP/IF/SBI-030/2022

University of São Paulo
Physics Institute

# Covariance matrix reconstruction of nonclassical light generated in an on-chip optical parametric oscillator

Roger Alfredo Kögler

Supervisor: Prof. Dr. Paulo Alberto Nussenzveig

Thesis submitted to the Physics Institute of the University of São Paulo in partial fulfillment of the requirements for the degree of Doctor of Science.

Prof. Dr. Paulo Alberto Nussenzveig (IFUSP)
Prof. Dr. Gabriel Teixeira Landi (IFUSP)
Prof. Dr. Ben Hur Viana Borges (EESC USP)
Prof. Dr. Felippe Alexandre Silva Barbosa (UNICAMP)
Prof. Dr. Sebastião José Nascimento de Pádua (UFMG)

São Paulo
2022

À memória de meu pai

Alfredo Kögler

# Acknowledgments

I thank my family for all the support they provided along all these years. My mother, Cristiane Loechelt Stüker, and her husband, Henri Stüker, have always been there to help me through the hard times and to cheer the good moments. I am very lucky to have people in my life who always point me in the right direction when I am lost. Without the wise advice of José Donizete Pinto, I would still be adrift. To my partner, Mayara Santana Pinto, there is no word in the dictionary that defines the absolute joy that is to have you by my side. I hope we can create one together.

All the work developed in the LMCAL would not be possible without the idealization and guidance of great scientists. I had the privilege of having two mentors, each one responsible for different aspects of my growth as a researcher. I value every teaching, they helped me to become an experimentalist that I could not even imagine four years ago. To professors Paulo Alberto Nussenzveig and Marcelo Martinelli, my deepest gratitude.

During the past years I had the opportunity to work with several awesome people, which were there to discuss physics and experimental challenges. You guys kept the daily live in around the lab always interesting. I want to namely thank the chips crew for all your hard work. Renato Ribeiro Domeneguetti introduced me to the area and taught me where to start (and a bunch of steps forward). I am very grateful for your patience, availability, late night works and indications of pizzas and hamburgers in Guarulhos. Carlos Andres González-Arciniegas has done the theoretical work that guided the project and has been always available to discuss his results. Curiously, he was building an optical cavity when I first started in the laboratory and allowed me to "help". So it was the theory guy who introduced me to the experimental work in the LMCAL. Pablo Jaime Palacios Avila skillfully assembled part of the experiment during his master's program and introduced me to all the work that he's done. Thank you, the three of you, for setting the beginnings of my work and for always being willing to help. My job has been so much easy Gabriel Couto Rickli joined the chip team. He worked hard in all the steps of the experiment and discussed all the data analysis with me. Furthermore, he has kindly reviewed this hole thesis text. I am truly happy to leave the future of this project in his more than capable

hands. I am obviously thankful for your hard and quality work, but more than that, I am thankful for your friendship. Wilder Rodrigues Cardoso followed and worked in the project for a while as a post-doc researcher, thank you for the helping hand. Although not officially in the team chips, Gabriel da Cruz Borba de Andrade accepted the brave task to adapt the acquisition data software for our system. Thank you for the helpfulness and for realizing a very good job. The newest member to pursue a future in the integrated systems part of the lab is Yuri Sacha Corrêa Lopes da Silva. I am eager that he joined us demonstrating a high will achieve quality results. For the past and present members of this project, my sincere wishes for success.

Thanks to the receptivity of the other members of the group, I could feel at home. I learned a lot with all of you that were willing to discuss physics (lots of politics and trivia included) and I must give a special thanks to the people that I was able to get close on a very personal level. To Alvaro Montaña Guerrero, Felipe Lucas Gewers, Lucas Nunes Faria, Luiz Couto Corrêa Pinto Filho, Raúl Leonardo Rincón Celis, thanks for receiving me into your lives. I want to extend my gratitude to Bárbara Abigail Ferreira Ribeiro, Beatriz Vilela de Moura, Breno Marques Gonçalves Teixeira, Emmi Herterich, Hans Marin Florez, Igor Koniecznia k, Pedro Antonio Jármy Derani, Rayssa Bruzaca de Andrade, Renné Luiz Câmara Medeiros de Araújo, Théo Louzada Meireles and Túlio Brito Brasil. I will not forget the unique, pleasant moments that I had with every one of you.

For the newest members of the laboratory, Ángel Manuel Gálvez Límaco, Gabriel Moniz Arantes and Luca Hullen Panuci, to which I did not have the opportunity to interact much, I wish you all the luck and success in this environment called LMCAL that can be harsh, embracing, frustrating, rewarding, confusing and cozy at the same time. Somehow, an uncomfortably pleasant Herculean job.

I further wish to thank all the administrative, technical and maintenance professionals of the physics institute, you are essential to keep the place running. Marcos Santos de Souza, Eduardo Monteiro and Sergio Kunihiro Korogui provided essential assistance respectively to mechanical, electronic and computational challenges that often arise in laboratory work. Thank you for your competence and willingness to help whenever needed. I also wish to namely thank Edneia Alves de Rezende and Luiz Antônio de Queiroz e Silva for all the helpful administrative assistance.

This study was financed in part by the *Coordenação de Aperfeiçoamento de Pessoal de Nível Superior - Brasil* (CAPES) - Finance Code 001 and by the São Paulo Research Foundation (FAPESP).

# Abstract

The increasing development of novel quantum technologies encourages the research in nonclassical states sources, being quantum correlated light one of the main resources for several applications of quantum mechanics. Silicon based integrated systems present huge potential for the further development of optical quantum communication, as they are compatible with microelectronic devices and telecommunication band wavelengths. The current capability of low loss waveguides production plus strong nonlinear coefficients makes this platform ideal for the generation of nonclassical states. Integrated microcavities can be tailored to act as low threshold optical parametric oscillators, where intense signal and idler modes are easily excited. Due to the parametric character of the physical process responsible for these oscillations, strong correlations are expected between the generated modes. We use resonator assisted detection systems to reconstruct the covariance matrices of the generated continuous variables states in order to retrieve the full quantum description of the system. Up to our knowledge, this is the first full tomography of states generated in an integrated third order optical parametric oscillator operating above threshold.
Keywords: Quantum Optics, Silicon Photonics, Optical Parametric Oscillator, Squeezing.

# Resumo

O crescente desenvolvimento de novas tecnologias quânticas encoraja a pesquisa em fontes de luz não-clássica, uma vez que estados correlacionados da luz representam um dos principais recursos para aplicações de mecânica quântica. Sistemas integrados baseados em silício apresentam grande potencial para ampliação do desenvolvimento de comunicações quânticas ópticas, já que são compatíveis com dispositivos microeletrônicos e com comprimentos de onda na banda de telecomunicações. A atual capacidade de manufatura de guias de onda com baixas perdas acrescida de altos coeficientes não-lineares fazem com que essas plataformas sejam ideais para a geração de estados não-clássicos. Microcavidades integradas podem ser desenvolvidas em ordem de atuar como osciladores paramétricos ópticos com baixo limiar de oscilação. Devido ao caráter paramétrico do processo físico responsável por tais oscilações, fortes correlações entre os modos gerados são esperadas. Nós utilizamos sistemas de detecção assistidos por ressonadores para reconstruir as matrizes de covariância dos estados gerados descritos por variáveis contínuas a fim de recuperar a descrição quântica completa do sistema. Até onde sabemos, esta é a primeira tomografia completa de estados gerados em um oscilador paramétrico óptico integrado de terceira ordem operando acima do limiar.
Palavras-Chave: Óptica Quântica, Fotônica baseada em Silício, Oscilador Paramétrico Óptico, Compressão de Ruído.

# Contents

# Introduction

The interest in novel quantum technologies plays a central role in several research aspects, ranging from fundamental aspects of quantum mechanics to the development of consumer products. The main domains of the field comprises communication, computation, simulation and sensing, which are explored with the help of several different experimental interfaces, such as trapped ions, atomic vapors, quantum dots, superconducting circuits, solid state impurities and integrated photonics [1]. Among these platforms, the use of photonic quantum states is of great prominence, since they represent the most suitable medium to transfer information between different devices for future quantum networks [2], as light weakly couples to the environment avoiding decoherence without the need of operating at low temperatures or in vacuum.

Sources of nonclassical light are the backbone for optical quantum applications and encompass two main branches: discrete variables states and continuous variables states. The first one is mainly directed to generation of single photons, which, in general, has a probabilistic character once their generation is usually based on spontaneous emission processes. On the other hand, the generation of continuous variables states is utterly deterministic. Although both kinds of states have been successfully employed in diverse experiments [3], we will focus on the latter. Nonclassical properties of continuous variables optical states, such as squeezing and entanglement [4–7], are of vast technological interest. They have applications in precision metrology [8], in gravitational wave detection [9], and are suitable to be used in scalable quantum communication, simulation and computation [10] protocols, such as one-way quantum computing [11].

Platforms compatible with the currently on development telecommunication technologies are of vast interest. In particular, silicon photonics are proving to be a strong platform to explore both generation and manipulation of quantum states of light [12]. Several features contributes to the interest on such systems. They are compatible with CMOS (complementary metal–oxide–semiconductor) fabrication process currently employed in the microelectronics industry, enabling seamless integration of photonics and electronics in the same chip. With the current maturity of manufacturing techniques, ultra-low

loss waveguides are routinely fabricated. Currently, complex optical circuits can be constructed, including thousands of optical components and microelectronic controls occupying centimeter- to millimeter-scale footprints, indicating the potential for scalability. Despite the quality of the in bulk optical devices, it is worth to emphasize that squeezing and continuous variables entanglement are strongly susceptible to optical losses, therefore long distance communications that preserve these properties are still a challenge. In that sense nonclassical light may exercise a central role in future technologies as quantum information carriers that interconnect different on-chip quantum systems in future integrated quantum networks [2]. A recent review exploring the different aspects of several materials that are used in quantum photonics can be found in [13]

The Laboratory of Coherent Manipulation of Atoms and Light (LMCAL) is specialized in the generation of bright nonclassical light by means of optical parametric oscillation [14–19], achieved by continuously pumping non-linear media in an optical resonator [20, 21] above a certain optical power threshold. Low-threshold oscillation is attained by taking advantage of silicon-based materials third-order nonlinearity, dispersion group velocity [22] and the high confinement of light in integrated optical microcavities [23, 24]. Through a collaboration with professors Michal Lipson and Alexander Gaeta from Columbia University we have access to high quality factors integrated optical parametric oscillators (OPOs). In the present thesis we will characterize pairs of bright modes generated in such devices by means of the reconstruction of their covariance matrix [25, 26]. Up to our knowledge, this is the first tomography of bipartite states generated in an integrated OPO operating above threshold. Our results reveal aspects of the dynamics of the two-mode states and enlighten the bottlenecks hindering the deterministic generation of entangled states.

This work is organized as follows. In the first chapter we will present the treatment for continuous variables Gaussian states and will show how they can be employed in quantum information protocols. Next, in chapter 2, we will explore the properties of microresonators in silicon photonics, their classical characterization, parametric oscillation condition and the dynamics of two-mode states. The optical setup is described in detail in chapter 3 and the data analysis and results are shown in chapter 4.

# Chapter 1

# Introduction to Continuous Variables Quantum Information

Information processing and sharing are some of the pillars of modern society and are present in most of people's daily lives. From air traffic control to remote surgery, from massive amounts of economic transactions to everyday online trivia, computational power dictates the majority of current technological activities and advances. Naturally, as more sophisticated applications are developed, more computational power is required. A consequence of this intricate relation between society and computing is the need of efficient cybersecurity. Nowadays, in parallel to surprisingly more efficient usage of CPUs, information processing has entered into quantum realm.

For decades now, the idea of information processing using degrees of freedom described by the laws of quantum mechanics is under investigation [27]. Recently, a major milestone was reached with the construction of quantum experiments capable of performing specific tasks more efficiently than any existent classical computer [28–31], where the latter [31] uses photonic technology. This is among one of the most shocking results of the field, which ignites strong academic and industrial activity towards useful application of quantum information technologies.

Among several different physical platforms to study quantum information, the use of light is particularly appealing. Since light is vastly employed in the context of classical communications, many advances in quantum optics take advantage of an already developed industry. Light usually interacts weakly with its environment, presenting smaller losses than alternative quantum systems. Also, the intrinsic relativistic character of the electromagnetic field makes it the fastest carrier of information available, as well as making it difficult to use for information storage. Nevertheless, light can be used to transfer information and interconnect different physical systems capable of storing its quantum state [2].

It is intuitive to approach quantum computing by quantizing the fundamental information unit. This gave birth to the *qubit*, which is generically associated to a two-level quantum system. In optical systems, one can encode a qubit in the polarization degree of freedom of single photons. That is, each quantized bit of information is represented by a photon in a certain polarization. Such encoding is vastly employed in quantum optics experiments and led to several important results in past decades [3]. Uncertainties in the single photon generation as well as the susceptibility of photons to experimental losses that completely destroy the information carrier, leads to the intrinsic probabilistic aspect to these experiments and to post selection necessity.

Within the same quantum information context, continuous quantum variables are continuous. Such variables belong to an infinite Hilbert space, limited to finite degrees of freedom of a finite set of physical systems. Although also subjected to decoherence induced by optical losses, continuous variables states are not completely lost (up to certain limits). Hence, one of the advantages in exploring the application of continuous variables (CV) to quantum information is their deterministic character, excluding the necessity of post selecting the data. However, the correlations between systems are naturally hindered to achieve the same levels as in corresponding discrete variables systems. Losses introduce errors on the experiment, leading to smaller figures of merit than those obtained by the discrete counterpart. Some breakthroughs in the exploration of CV systems for quantum information are the successful implementation of quantum teleportation [32] and the theoretical proof of universal quantum computation [33]. In the present thesis, we will explore the fluctuations in the amplitude and phase quadratures of the electromagnetic field as the quantized carriers of information.

This chapter will be organized as follows. First, we will introduce the notation and principal tools for the treatment of continuous variables systems. Posterior sections will treat some of the applications of continuous variables to quantum information. Quantum teleportation will be approached in section 1.2 followed by the entanglement swapping protocol. In the last section we will briefly discuss quantum cryptography schemes.

## 1.1 Gaussian States

In this section we will describe how Gaussian states are related to the covariance matrix and which kind of information about the physical system can be obtained from it. The treatment presented here follows the textbooks [5, 7]. We start the description of CV states with a finite set of observables that describe pairs of degrees of freedom within

infinite Hilbert spaces. We then organize the variables in a vector containing all the operators as

$$\hat{\mathbf{x}} = [\hat{p}_1, \hat{q}_1, \hat{p}_2, \hat{q}_2, \ldots, \hat{p}_n, \hat{q}_n]^{\mathrm{T}}. \tag{1.1}$$

A set that completely specifies the state of a system is bounded by canonical commutation relations that, in general can be written in their symplectic form as:

$$\left[\hat{\mathbf{x}}, \hat{\mathbf{x}}^T\right] = i\Omega, \tag{1.2}$$

with

$$\Omega = \bigoplus_{j=1}^{n} \Omega'_j, \qquad \Omega'_j = \begin{bmatrix} 0 & 1 \\ -1 & 0 \end{bmatrix}, \tag{1.3}$$

where $\bigoplus$ is the direct sum operator leading to a block diagonal matrix composed of all $\Omega'_j$ entries. Identity matrices needed for dimensional accordance are implicit. The symplectic group is defined by the set of transformations $S$ that preserves the canonical commutation relations, that is $S\Omega S^{\mathrm{T}} = \Omega$.

Of particular interest is a class of states known as Gaussian states. From the quasi-probability distribution perspective, as in the Wigner representation of optical states [4], Gaussian states are those that respect Gaussian statistics. While that seems to be limiting, the restriction to Gaussian states accurately describes most of optical systems. Several important states in quantum optics, including those relevant for the experimental results of this work, are included in this classification, for example vacuum, thermal, coherent, squeezed and squeezed-thermal states of the optical field [4, 7]. Furthermore, interactions described by linear or bilinear Hamiltonians do not change the Gaussianity of states. Hence, Gaussian states can be obtained by acting with these classes of interactions on a vacuum state. It is worth to emphasize that all operations of the system under study, described in chapter 2, are Gaussian. Although the deterministic generation of non-Gaussian states are a relevant challenge for information processing, Gaussian states are applicable on tasks as communication protocols and precise measurements [7, 34, 35].

Gaussian states are completely defined by their first and second order moments. Furthermore, physical properties that are invariant under local unitary transformations, such as purity and entanglement, are completely characterized by their second order moments, represented by a $2n \times 2n$ covariance matrix ($\mathbb{V}$), where $n$ is the number of modes being described. Each entry of the covariance matrix is given by the usual relation

$$\mathbb{V}_{j,k} = \left\langle \hat{\mathbf{x}}_j \hat{\mathbf{x}}_k \right\rangle - \left\langle \hat{\mathbf{x}}_j \right\rangle \left\langle \hat{\mathbf{x}}_k \right\rangle. \tag{1.4}$$

For $\mathbb{V}$ to be a valid representation of a physical density matrix, the uncertainty relation

$$\mathbb{V} + i\Omega \geq 0, \tag{1.5}$$

namely the Robertson-Schrödinger uncertainty relation, must be fulfilled. Alternatively, by Williamson's theorem [36], any $n$-mode Gaussian state can be represented in a diagonal form undergoing a transformation

$$\mathbb{V}_D = S\mathbb{V}S^{\mathrm{T}} = \mathrm{Diag}\{\nu_1, \nu_1, \nu_2, \nu_2, \ldots, \nu_n, \nu_n\} \tag{1.6}$$

where $S$ and $S^{\mathrm{T}}$ are symplectic operations. The uncertainty relation of equation (1.5) holds in this representation since $\Omega$ is invariant under symplectic transformations. Therefore, the eigenvalues of $\mathbb{V}_D$ must respect the condition $\nu_j \geq 1, j = \{1, 2, \ldots, n\}$. A practical way to determine the symplectic eigenvalues is by diagonalizing the matrix $(\mathbb{V}\Omega)^2$ whose eigenvalues are given by $(-\nu_j^2), j = \{1, 2, \ldots, n\}$ [35].

Several physical properties can be retrieved from covariance matrices that properly describes a Gaussian state. The purity of the state, that is, how close the system is to a pure state is given by [37, 38]

$$\mathfrak{p} = \frac{1}{\sqrt{\mathrm{Det}(\mathbb{V})}} = \frac{1}{\Pi_{j=0}^{n}\nu_j^2}. \tag{1.7}$$

A Gaussian state is pure if and only if its covariance matrix has unitary determinant. On the other hand, mixed states, statistical ensembles of pure states, are characterized by $\mathfrak{p} < 1$ . For a completely mixed state the purity tends to $\mathfrak{p}_{\mathrm{cm}} = 1/d$, where $d$ is the dimension of the Hilbert space of the system. Hence, $\mathfrak{p}_{\mathrm{cm}} = 0$ in the continuous variables limit.

Another important use of the covariance matrix is the determination of entanglement. First discussed by founding fathers of quantum mechanics [39–41], quantum entanglement is a characteristic of composite quantum systems that cannot be completely described by only knowing its subsystems. That is, any local attempt to describe the global system entails information loss. From the works of John S. Bell [42, 43], a series of inequalities must be fulfilled to proof the local nature of a physical system. The violation of such inequalities is a sufficient criterion for a quantum system to be entangled.

In the formalism of density operators [4, 27], the global state ($\rho_{\mathrm{G}}$) laying in the Hilbert space $\mathcal{H}_{\mathcal{G}} = \mathcal{H}_1 \otimes \mathcal{H}_2 \otimes \ldots \otimes \mathcal{H}_{\mathrm{N}}$ is said to be separable if it can be written as a tensor product of density operators of the subspaces, that is

$$\rho_{\mathrm{G}} = \sum_i p_i \left(\rho_1^i \otimes \rho_2^i \otimes \ldots \otimes \rho_{\mathrm{N}}^i\right), \tag{1.8}$$

where mixed states are included with the sum over a statistical ensemble of pure states ($\sum_i p_i = 1$). Any state that cannot be written in the form of equation (1.8) is said to be entangled. An equivalent separability condition can be formulated with the covariance matrix of Gaussian states. A Gaussian state is separable if and only if there exists the covariance matrices $\mathbb{V}_A$ and $\mathbb{V}_B$ for the respective subsystems $A$ and $B$ such that they respect the inequality [44]

$$\mathbb{V} \geq \mathbb{V}_A \oplus \mathbb{V}_B. \tag{1.9}$$

Although general for Gaussian states, this criterion is not very useful in practice. Restricting the number of degrees of freedom of the system, more applicable criteria can be used.

A practical approach is done by the analysis of the partial transposition of $\mathbb{V}$ with a method known as positive partial transpose (PPT) criterion [45]. The partial transposition of a quantum state of $(m+n)$ modes with respect to the $n$ partition is calculated as

$$\tilde{\mathbb{V}} = T\mathbb{V}T, \tag{1.10}$$

with

$$T = \mathbb{1}_{2m} \oplus \Sigma_n, \quad \Sigma_n = \bigoplus_{j=1}^{n} \sigma_z, \tag{1.11}$$

where $\sigma_z$ is the Pauli-z matrix given by

$$\sigma_z = \begin{bmatrix} 1 & 0 \\ 0 & -1 \end{bmatrix}. \tag{1.12}$$

For the special case of two-mode Gaussian states with dimension $2 \otimes 2$, the subsystems are separable if and only if equation (1.5) holds for $\tilde{\mathbb{V}}$ [45]. Extensions of the PPT to special cases of systems in higher dimensions can be derived, but they will not be approached in this work.

Another entanglement criterion, known as the Duan-Giedke-Cirac-Zoller (DGCZ) inseparability criterion [46], is given by

$$\Delta^2 \hat{p}_- + \Delta^2 \hat{q}_+ \geq 1, \tag{1.13}$$

where $\Delta^2$x is the variance of $x$ equivalent to equation (1.4) and

$$\hat{p}_\pm = \frac{\hat{p}_A \pm \hat{p}_B}{\sqrt{2}}, \tag{1.14}$$

$$\hat{q}_\pm = \frac{\hat{q}_A \pm \hat{q}_B}{\sqrt{2}}, \tag{1.15}$$

with

$$\left[\hat{p}_\pm, \hat{q}_\mp\right] = 0. \tag{1.16}$$

Although restricted to robust entangled states [17], and hence less general than the PPT criterion, this method will serve as a visually resource when discussing the experimental results in chapter 4.

In this section we introduced the covariance matrix to verify simple properties of Gaussian states. This mathematical object is specially interesting since it can be experimentally reconstructed. Although the presented notation is sufficient to describe the system that we will analyze in this thesis, we will often recur to a more usual operator formalism without any extensive introduction to it. Of special importance are the displacement and the single- and two-mode squeezing operators, which will be used in the next sections. Thorough exposure of such theoretical framework can be found in traditional quantum optics textbooks [4].

Entangled states are one of the building blocks for quantum information applications and are of extremely interest in quantum optics experiments. As a motivation for the generation of such states, we will present next two quantum information protocols and a cryptography scheme using two-mode entangled Gaussian states.

## 1.2 Quantum Teleportation

Quantum entanglement is a core resource for quantum information protocols. Taking advantage of nonclassical correlations one can perform certain communication tasks more efficiently than an equivalent attempt with local states and classical communication. A notorious example is the teleportation protocol, which allows the transferring of an unknown quantum state between two distant parties that share an entangled state and a classical communication channel [47].

The full protocol is described as follows:

1. An entangled state is distributed between a sender (Alice) and a receiver (Bob).
2. Alice performs a joint measurement in a maximally entangled basis between her part of the shared state and the unknown state ($|\psi\rangle$) she desires to teleport.
3. Alice communicates her result to Bob through a classical communication channel.
4. Bob performs a unitary operation in his part of the entangled state conditioned to Alice's measurement result.

In an idealized situation, where the shared state is maximally entangled and no noise sources are present in the protocol steps, Bob perfectly retrieves the $|\psi\rangle$ state, as illustrated in figure 1.1.

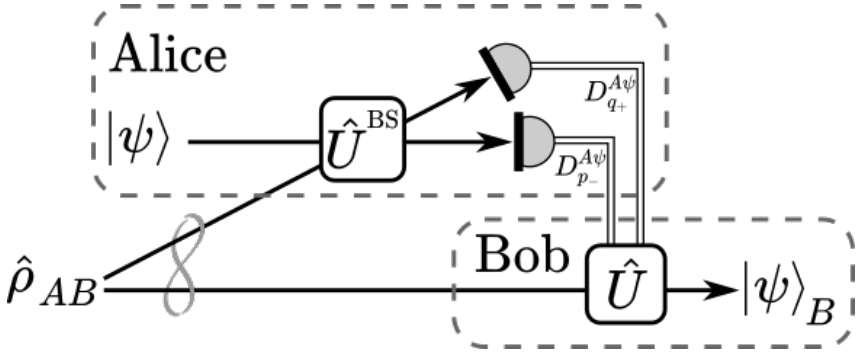


Figure 1.1: Quantum teleportation scheme. A maximally entangled state is distributed between Alice and Bob. Alice performs a joint measurement in the unknown state $|\psi\rangle$ and her share of the EPR state. She then informs Bob of her results, $D^{A\psi}_{p_-}$ and $D^{A\psi}_{q_+}$, through a classical communication channel. Bob makes a unitary operation conditioned to Alice's measurement in his state and retrieves the state $|\psi\rangle$ in his quantum channel. Straight lines: quantum channels. Double lines: classical communication channels. $\hat{U}^{\mathrm{BS}}$: beam splitter.

Following [48, 49], in a continuous variables idealized frame, we start the protocol considering a state $\hat{\rho}_{AB}$ that maximally violates a two-mode separability criterion, commonly known as the Einstein-Podolsky-Rosen (EPR) state. Indexes $A$ and $B$ where chosen here to indicate Alice and Bob. The EPR state can be seen as a two-mode vacuum state with arbitrarily large squeezing. Such state is fully characterized by null first moments and by the covariance matrix

$$\mathbb{V}_{AB} = \lim_{r\to\infty} \begin{bmatrix} \cosh(2r)\mathbb{1}_2 & \sinh(2r)\sigma_z \\ \sinh(2r)\sigma_z & \cosh(2r)\mathbb{1}_2 \end{bmatrix}, \tag{1.17}$$

where $r$ is the parameter that accounts for the amount of squeezing present in the system. In the limit of $r \to \infty$, we have null eigenvalues for the commuting quadratures $\hat{p}_- = (\hat{p}_A - \hat{p}_B)/\sqrt{2}$ and $\hat{q}_+ = (\hat{q}_A + \hat{q}_B)/\sqrt{2}$. In Heisenberg's picture, this condition can only be respected if

$$\hat{p}_A = \hat{p}_B, \tag{1.18}$$

$$\hat{q}_A = -\hat{q}_B. \tag{1.19}$$

Notice that this relation depends on the choice of limit of $r$ and other commuting quadratures could be equivalently used in different approaches.

Alice proceeds the protocol by performing a joint measurement in her part of the entangled subsystem together with the state she desires to teleport in the $\{\hat{p}_-, \hat{q}_+\}$ basis. In practice, this is equivalent to mixing the states in a lossless $50:50$ beam splitter ($\hat{U}^{\mathrm{BS}}$ in figure 1.1) followed by projections $|p\rangle\langle p|$ in mode "$-$" and $|q\rangle\langle q|$ in mode "$+$", as

illustrated in figure 1.1. After the beam splitter the quadratures transforms as

$$\hat{p}_{\pm}^{A\psi} = \frac{\hat{p}_A \pm \hat{p}_\psi}{\sqrt{2}} \tag{1.20}$$

$$\hat{q}_{\pm}^{A\psi} = \frac{\hat{q}_A \pm \hat{q}_\psi}{\sqrt{2}}. \tag{1.21}$$

The projection on $\hat{p}_-^{A\psi}$ and $\hat{q}_+^{A\psi}$ collapses Alice's state in

$$\hat{p}_A = \hat{p}_\psi + \sqrt{2} D_{p_-}^{A\psi} \tag{1.22}$$

$$\hat{q}_A = -\hat{q}_\psi + \sqrt{2} D_{q_+}^{A\psi}, \tag{1.23}$$

where $D_{p_-}^{A\psi}$ and $D_{q_+}^{A\psi}$ are the respective results of the projections. The results contain the information of how distant her state is from $|\psi\rangle$. As a consequence of the EPR correlations, they also carry the information of the distance between Bob's system $|\psi\rangle$. From relations (1.18) and (1.19), Bob's share of the EPR can be written as

$$\hat{p}_B = \hat{p}_\psi + \sqrt{2} D_{p_-}^{A\psi}, \tag{1.24}$$

$$\hat{q}_B = \hat{q}_\psi - \sqrt{2} D_{q_+}^{A\psi}, \tag{1.25}$$

which presents the same second moments of the state $|\psi\rangle$ apart from a displacement of the field. Once Alice communicates her measurement results, Bob can compensate his state with unitary evolutions (applying a displacement operation) in order to perfectly retrieve the state $|\psi\rangle_B$ in his system. It is important to emphasize that before receiving the $D_{p_-}^{A\psi}$ and $D_{q_+}^{A\psi}$ values Bob has a maximally mixed state in his channel. That is, without the classical communication, Bob has no knowledge about the state in his channel.

In practice, the described protocol is impossible due to the infinite squeezing approximation. In a realistic scenario one can only have access to a limited amount of squeezing. Nevertheless, for sufficiently high entanglement, nonlocal correlations are present in the quantum channel and the teleportation protocol can still be performed. A quantum teleportation is characterized by the *fidelity* ($F$) of the final state in Bob's hand. That is, how closely the teleported state is to the original one. Fidelity boundaries for successful quantum teleportation are established depending on the state to be sent. For a coherent state, for instance, this limit is known to be $F = 1/2$ and is related to the squeezing parameter $r$ by [32]

$$F_{\text{coh}} = \frac{1}{1 + e^{-2r}}. \tag{1.26}$$

For the infinite squeezing limit $r \to \infty$ and $F_{\text{coh}} \to 1$. The classical benchmark of $F_{\text{coh}} = 1/2$ is retrieved for $r = 0$. That is, for any amount of entanglement ($r > 0$) it is possible to perform a quantum teleportation of a coherent state. Naturally, losses and

measurement imperfections existent in real quantum optics experiments can hinder the effectiveness of the protocol.

Experimental advances in the realization of quantum teleportation are of great importance for quantum communication and computing. The transportation of quantum states inside quantum devices is essential to their functioning in the same way that classical information needs to be transferred along wires. Even in the presence of losses, quantum teleportation might represent a more efficient communication link between quantum systems than directly sending them through quantum channels.

### 1.2.1 Entanglement Swapping

The quantum teleportation protocol can be extended to a number of different applications, including further protocols of quantum technology. The transferring of quantum states by means of quantum teleportation can be extended to the distribution of entanglement between parties [50]. Consider that instead of sharing an entangled state, Bob and Alice have locally access to (or means of preparing) an entangled bipartite system each. Let us denote Alice's state by $\hat{\rho}_{AA'}$ and Bob's state $\hat{\rho}_{BB'}$. They send a partition of their systems ($A'$ and $B'$) to a third party, let us say Charlie, who performs a joint measurement in a maximally entangled basis in the subsystems. Now Alice and Bob share an entangled pair $\hat{\rho}_{AB}$ conditioned to Charlie's result. This procedure is illustrated in figure 1.2.

In the same spirit of last section, let us illustrate this process in the simplest way. Consider that Alice and Bob individually have access to maximally entangled bipartite states that respect the same conditions of equations (1.18) and (1.19) with the new indexes

$$\hat{p}_A = \hat{p}_{A'}, \quad \hat{q}_A = -\hat{q}_{A'}, \tag{1.27}$$

$$\hat{p}_B = \hat{p}_{B'}, \quad \hat{q}_B = -\hat{q}_{B'}. \tag{1.28}$$

Charlie proceeds the joint measuring in the same way as done before. He mixes the systems $A'$ and $B'$ in a $50:50$ beam splitter and perform projective measurements on the resultant two-mode quadratures

$$\hat{p}'_- = \frac{\hat{p}_{A'} - \hat{p}_{B'}}{\sqrt{2}}, \tag{1.29}$$

$$\hat{q}'_+ = \frac{\hat{q}_{A'} + \hat{q}_{B'}}{\sqrt{2}}, \tag{1.30}$$

yielding the respective results $D'_{p_-}$ and $D'_{q_+}$. Similar to the teleportation protocol, this values carry the information about the distance between the maximally mixed states in Alice and Bob channels and a maximally entangled state. From equations (1.27)–(1.30)

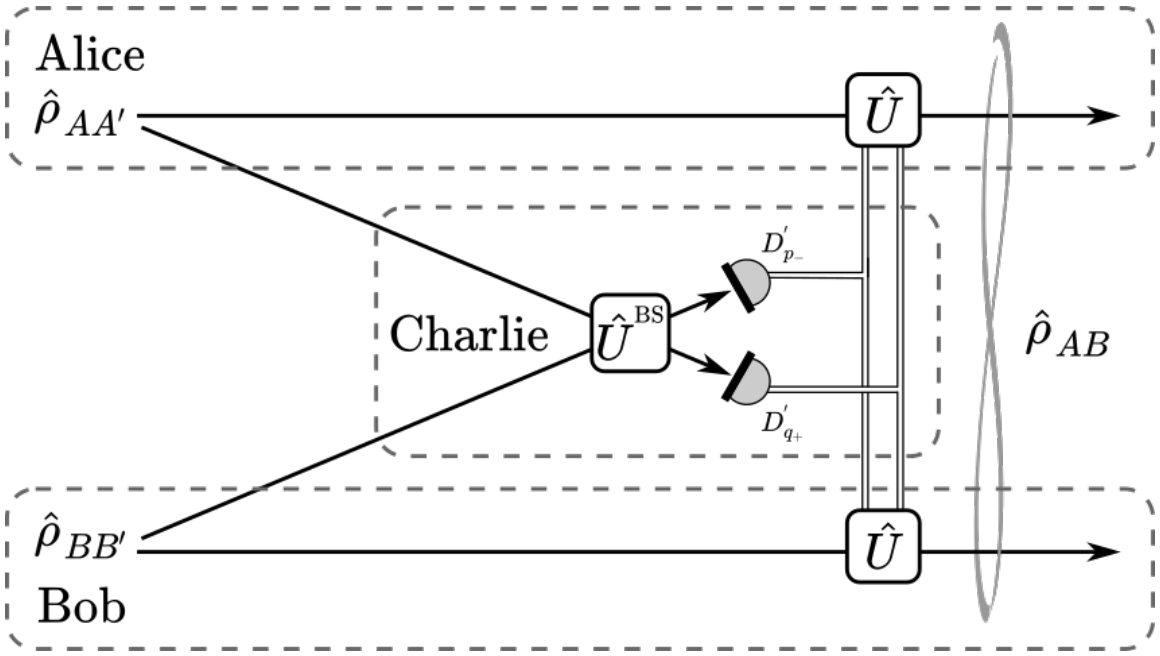


Figure 1.2: Entanglement swapping scheme. Alice and Bob send a partition of an entangled state in their possession to Charlie. Charlie then performs a measurement in this modes in a maximally entangled basis. Alice and Bob apply unitary evolutions to their remaining subsystem conditioned to Charlie's results and end up sharing a specified entangled state.

one can write Bob's and Alice's states as

$$\hat{p}_A = \hat{p}_B + \sqrt{2}D'_{p_-}, \tag{1.31}$$

$$\hat{q}_A = -\hat{q}_B - \sqrt{2}D'_{q_+}, \tag{1.32}$$

which, apart from the unknown displacements $D'_{p_-}$ and $D'_{q_+}$, are equivalent to the maximum entangled vacuum state of equations (1.18) and (1.19). In order take advantage of the new shared state in other quantum information applications, Alice or Bob need to be informed of Charlie's measurements results, that can be broadcasted by him through classical channels [51].

Entanglement swapping allows the distribution of nonlocal entanglement between distant particles without the need for them to directly interact. The presence of noise in real quantum channels is in principle a limiting factor in such distributions, which can be mitigated with the use of quantum repeaters [52]. They combine entanglement swapping with strategies of entanglement distillation [53], which allows one to trade a number of identical poorly entangled states for a smaller number of states with enhanced entanglement. This can be used to distribute entangled systems over lossy channels, constituting a main role in quantum networks [2].

## 1.3 Quantum Cryptography

Security is of extreme importance in the current global communication network. The merge of quantum and information sciences lead to the investigation of secure communication ruled by quantum mechanical laws and its limits. Typically, quantum cryptography protocols are based on two parties, Alice and Bob, that establish a secret key by exchanging quantum systems through an insecure channel. The quality of the protocol is determined by testing the strongest attacks allowed by general perturbations in the shared quantum systems by an eavesdropper, say Eve.

Several proposals of secure communication protocols rely on the distribution of *qubits* [54, 55]. The generation of such states is of probabilistic in nature, once it usually relies on spontaneous emission processes, and limits the data transmission rates. Despite further decreasing the transmission rate, the security of discrete variables quantum cryptography is not compromised in the presence of losses, as the information carrier is destroyed. On the other hand, quantum key distributions with continuous variables presents higher data flow, but their security is impaired by losses. In this section, we will briefly describe the first quantum key distribution proposal, followed by a similar continuous variables approach. This allows us to compare their differences in a fundamental quantum mechanical level.

The traditional BB84 protocol was developed by Bennett and Brassard in 1984 [56]. In their proposal, Alice sends qubits to Bob randomly distributed over four states of the maximally overlapped basis $\{|0\rangle, |1\rangle\}$ and $\{|+\rangle, |-\rangle\}$. Bob projectively measures the received qubits in the same two basis that Alice used, again choosing them at random. They then share their chosen basis publicly, gaining information of the correlation between the prepared states and the measured basis. Hence, Alice and Bob simultaneously know the state in which roughly 50% of the qubits were prepared, which is encoded in the shared secret key as a sequence of binary numbers of 0 for the correct measurement of states $|0\rangle$ or $|+\rangle$ and as 1 for the correct measurement of states $|1\rangle$ or $|-\rangle$. Note that the public announcement of the measurement *basis* does not give any information of the *results* that Bob obtained, neither inform which states Alice prepared. An example of this process is schematically represented in table 1.1.

Let us now consider that Eve tries to gain information about the secret key by attacking the quantum channel in which Alice sends the qubits to Bob. The obvious attempt is to intercept a qubit and keep the measurement to herself. In this case, Bob would not receive a qubit and simply informing this publicly would make Alice disregard this state

Table 1.1: BB84 secret key generation. The operators $\hat{P}_{01}$ and $\hat{P}_{\pm}$ are respectively related to projective measurements performed on the $\{|0\rangle, |1\rangle\}$ and $\{|+\rangle, |-\rangle\}$ basis.

| **Alice** | $\|1\rangle$ | $\|1\rangle$ | $\|+\rangle$ | $\|0\rangle$ | $\|-\rangle$ | ... | $\|+\rangle$ | $\|-\rangle$ | $\|0\rangle$ | $\|+\rangle$ | $\|1\rangle$ | $\|-\rangle$ |
|---|---|---|---|---|---|---|---|---|---|---|---|---|
| **Bob** | $\hat{P}_{01}$ | $\hat{P}_{\pm}$ | $\hat{P}_{\pm}$ | $\hat{P}_{\pm}$ | $\hat{P}_{01}$ | ... | $\hat{P}_{\pm}$ | $\hat{P}_{01}$ | $\hat{P}_{01}$ | $\hat{P}_{01}$ | $\hat{P}_{01}$ | $\hat{P}_{\pm}$ |
| **Same Basis** | Yes | No | Yes | No | No | ... | Yes | No | Yes | No | Yes | Yes |
| **Secret Key** | 1 | - | 0 | - | - | ... | 0 | - | 0 | - | 1 | 1 |

in the final key. This reduces the data transmission rate, but does not prevent any final secure key. Next, let us say that after Eve measures the intercepted system, she re-sends to Bob a newly prepared state. In half the cases, Eve will be lucky enough to send a state in the same basis as the prepared one. Even so, Alice and Bob will notice a drop from 50% to 25% in the correlated information once the public key is announced. This readily inform the presence of Eve.

Alternatively, Eve could drop her interception rate to only a few qubits, trying to mask her presence. However, this is detectable by publicly comparison of a fraction of the secret key. If there are any discrepancies between Alice's and Bob's key they will know that Eve tried to attack the cryptography scheme. Any time that Eve re-sends a qubit, even in an insignificant rate, there is only a 50% chance of her sending the exact state prepared by Alice, which will eventually cause a difference between the secret keys determined by Alice and Bob [54].

An equivalent protocol for discrete quantum key distribution can be performed with shared entangled states between Alice and Bob, achieving the same kind of protection [57]. Security is established by randomly choosing the measurement basis. Any attempt of attack in the quantum channel by measurements will inevitably disturb the system, which can be verified in *a posteriori* comparison of a fraction of the secret key.

In the presented discussion, we omitted the possibility of errors in the shared key caused by technical issues, which realistically have to be considered. One should also worry about possible attacks to every experimental breach, which can lead to very elaborate protocols. Furthermore, the random character of the state preparation and choose of measurement basis can be questioned. Reference [54] presents a thorough review on several aspects of discrete variables quantum cryptography.

A rather direct mapping of the cryptographic protocol into the continuous variables domain can be thought of as an encryption of messages in orthogonal quadratures of a coherent state. Alice modulates the phase and amplitude quadratures of a weak field in the continuous variables domain and Bob randomly detects one of them. Uncertainty

principle forbids an interceptor to read both quadratures at the same time, hindering the re-emission of the same state to a probability superior to 50%. This can be effectively discovered by comparing a part of Bob's result with Alice's encryption. However, Eve could apply a different strategy, collecting only a fraction of the intense beam and trying to obtain some information about the quadratures. Hence, optimal security is not guaranteed only by the uncertainty principle of conjugate quadratures in this regime. That is, there exists an optimal strategy that can be employed by Eve to acquire more information about the secret key with a lower chance of detection than the discrete counterpart. Losses, as photon absorption or scattering along the transmission line, and measurements performed by Eve in a discrete variables systems have equivalent effects in the communication channel as they both destroy the information carrier, which is not true for continuous variables states. It was then shown that two-mode squeezing is needed in two commuting quadratures to reach the security levels of the discrete variables protocol [58]. This highlights the importance of entanglement as a useful resource in secure quantum communications.

Let us then use the needed entangled state to illustrate the continuous variables quantum key distribution. An interesting mapping of binary information in the violation of the standard quantum limit of different quadratures is proposed in [59], which will be followed next. Consider the amplitude $\hat{p}_j$ and phase quadratures $\hat{q}_j$ of two bright beams, $j = A, B$. The intense field can be separated from the small fluctuations of each quadrature by writing them in the linearized forms $\hat{p}_j = \langle \hat{p}_j \rangle + \delta\hat{p}_j$ and $\hat{q}_j = \langle \hat{q}_j \rangle + \delta\hat{q}_j$. For two-mode correlations it is convenient to express the state fluctuations in the sum and subtraction basis, equations (1.14) and (1.15). Enhanced security is guaranteed when squeezing is mutually present in two of the commuting quadratures, say

$$\Delta^2\delta\hat{p}_- < 1, \quad \Delta^2\delta\hat{q}_+ < 1, \tag{1.33}$$

where normalization by the standard quantum limit is implicit. The conditions of equation (1.33) clearly ensures entanglement by violation of DGCZ criterion, equations (1.13).

As we schematically represented in figure 1.3, Alice generates two-mode entangled bright beams ($\hat{\rho}_{AB}$) and distributes one of them to Bob. They randomly measure their amplitude ($\hat{p}$) or phase ($\hat{q}$) quadrature. To verify correlations it is important that the measurements occur synchronously, hence the shared clock. Alice proceeds sending to Bob her registered photocurrent. He checks if correlations are present by comparing the received information with his measurement. He then shares with Alice if he obtained squeezing or not. In the absence of losses and eavesdropping attempts, squeezing is obtained when Bob and Alice measure the same quadrature. In this case, they encode 0 for amplitude

Table 1.2: Continuous variables quantum key distribution.

| **Time** | $t_1$ | $t_2$ | $t_3$ | $t_4$ | $t_5$ | $t_6$ | ... | $t_n$ | $t_{n+1}$ | $t_{n+2}$ | $t_{n+3}$ | $t_{n+4}$ |
|---|---|---|---|---|---|---|---|---|---|---|---|---|
| **Alice** | $\hat{p}$ | $\hat{p}$ | $\hat{q}$ | $\hat{p}$ | $\hat{q}$ | $\hat{q}$ | ... | $\hat{q}$ | $\hat{p}$ | $\hat{p}$ | $\hat{p}$ | $\hat{q}$ |
| **Bob** | $\hat{p}$ | $\hat{q}$ | $\hat{p}$ | $\hat{p}$ | $\hat{p}$ | $\hat{q}$ | ... | $\hat{p}$ | $\hat{q}$ | $\hat{q}$ | $\hat{p}$ | $\hat{q}$ |
| **Correlation** | Yes | No | No | Yes | No | Yes | ... | No | No | No | Yes | Yes |
| **Secret Key** | 0 | - | - | 0 | - | 1 | ... | - | - | - | 0 | 1 |

coincidence and 1 for phase. If the measurements do not coincide, no correlations will be stated by Bob and no key bit is registered. This procedure is exemplified in table 1.2.

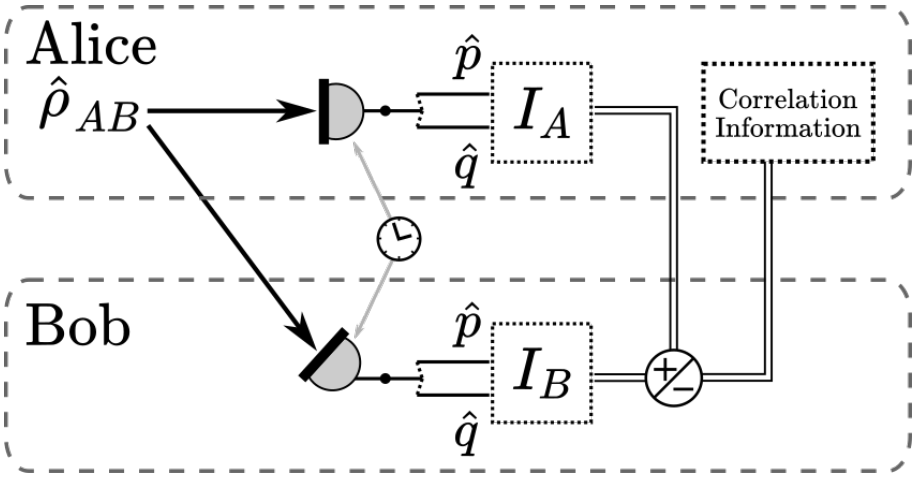


Figure 1.3: Quantum key distribution scheme. Alice distributes to Bob a subsystem of a prepared entangled state. They synchronously measure the $\hat{p}$ or $\hat{q}$ quadrature randomly. Alice then shares her measured photocurrent ($I_A$) with Bob via classical communication and he proceeds to analyze the correlations between $I_A$ and the photocurrent measured in his station $I_B$. Bob then communicates if the photocurrents are correlated bellow the standard quantum limit or not. If they luckily choose the same quadrature, a bit attributed to amplitude (0) or phase (1) is shared. Repeating this process at several times, a secret key is generated.

Attacks in the optical channel are revealed by the sensitivity of the correlations to losses and the impossibility of simultaneous measurements of both quadratures. The whistleblowers of eavesdropping are the occurrence of the no correlation event in more then 50% of the measurements and distortions of correlations caused by losses induced by Eve.

Apart from the need of the clock, this scheme seems identical to the one showed for discrete variables. However, the transmission rate is progressively altered in the presence of losses. This implies a limitation of the key distribution range, once losses tend to increase with distance. In this lossy regime, Eve can try to mask herself among the losses of the system, which can make more difficult to detect her presence. Nevertheless, large

transmission rates may compensate for the risks or be sacrificed to enhance the quality of the entangled pair with quantum repeaters, as discussed in section 1.2.1.

At last, it is important to emphasize that the presented schemes are far from being the only possibilities to take advantage of quantum channels to distribute secure keys. Practically, coherent states quantum key distribution schemes are vastly explored. The advantages taken from strong correlations between fields are also not limited to the ones pointed in the presented protocol. Reference [55] compiles a vast number of references on quantum cryptography with a good review on different discrete and continuous variables strategies, as well as several attack possibilities and practical implementations.

• •

In this chapter we presented some formal aspects of the treatment of Gaussian states, giving special attention to the determination of their purity and correlations. It is important to keep in mind that such analysis assumes the Gaussianity of the system, which is not guaranteed by analyzing an arbitrary covariance matrix.

We then proceeded to illustrate how continuous variables systems can be applied to quantum information protocols. Even though matter based quantum systems are arguably more suitable to quantum processing and quantum memories it is hard to think of a more suitable candidate to data transferring between them. Entanglement swapping can be used in the context of quantum networks [2], where multicolor light act as a quantum channel to exchange entanglement between different systems (quantum nodes) responsible for different tasks, figure 1.4. The high sensitivity to losses of the quantum correlations may preclude long distance data transferring without the need of quantum repeaters. Nevertheless, intense light can be very efficient as carrier of information between quantum nodes inside small integrated systems, where the short distances may result in negligible perturbations in the state for high transparent media. Hence, continuous variables quantum correlations may present as a key factor to future scalable quantum technologies.

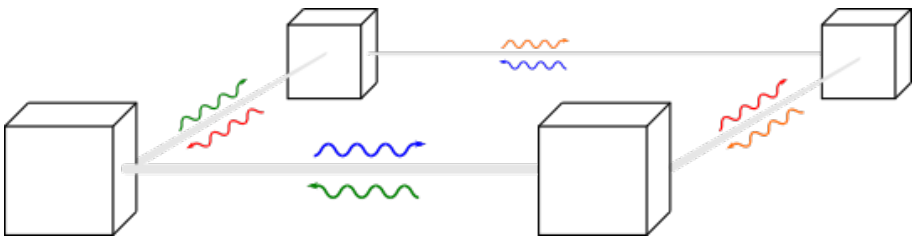

Figure 1.4: Representation of a quantum network, where different systems inside the boxes (nodes) are interconnected by multicolor quantum channels.

Sensible data is also assured to be protected by means of quantum cryptography, briefly introduced in the contexts of discrete and continuous variables. In this scenario, thousands of kilometers long secure lines were proven utilizing satellite to ground free space entangled quantum channels [60] and hundreds of kilometers secure lines by means of optical fibers communications assisted by silicon photonics devices [61].

Intense entangled light is an important ingredient for current and future quantum technologies. Due to its deterministic nature for applications to quantum information and high rate communication channels, reliable sources of nonclassical light are of vast interest of ongoing research. In the next chapter we will present the system under study in this work and how they can be used in the generation of CV quantum states.

# Chapter 2

# On-Chip Kerr Optical Parametric Oscillators

With the development of novel photonic technologies, where several optical components are printed in small footprints, there is a crescent interest for application of quantum information in small scales. Full optical experiments are currently feasible in such integrated devices. As discussed in chapter 1, a key ingredient for quantum applications is the entanglement and its distribution through light, as such phenomenon is at the core of communication protocols. Therefore, integrated sources of entangled states are of great interest.

In the discrete variables domain, integrated sources of entangled photons have been successfully demonstrated. The diverse platforms encompass optical components ranging from straight waveguides to optical resonators and materials including lithium niobate [62–64], silicon [65–67], nitrides [68–70] and semiconductor arsenides [71–73]. Combined with other on-chip devices, discrete quantum information protocols were successfully employed in photonic platforms [74–77]. For robust reviews including on-chip sources and applications one can recur to [12, 78, 79]

On the other hand, integrated sources of continuous variables entangled states remains a challenge. Although CV quantum entanglement on-chip was already verified in [80, 81], external sources of nonclassical light were necessary. Another approach consists in using non-degenerate optical parametric oscillators to directly produce entangled beams. Nanophotonics enables the miniaturization of such devices, which sustains strongly confined optical modes in a closed path waveguide structure. Microresonators with high quality factors, several orders of magnitude above mirror-based ones, are routinely designed with different shapes and materials.

Despite the variety of materials that can be employed in the construction of photonic systems, silicon-based materials are of special interest. They benefit from a currently

mature manufacturing industry to reach high quality, low loss waveguides in very compact structures. Furthermore, they are naturally compatible with CMOS technology, which is the basis of current microelectronic devices.

In this chapter we will explore integrated microcavities in the silicon photonics context. In section 2.1 we will treat the coupling and loss mechanisms associated with the propagation of light trough such structures. Next, we will explore the treatment of optical parametric oscillations, approaching the oscillation conditions of the system section 2.2.1, and the properties of the output light in section 2.2.2.

## 2.1 Silicon Nitride Micro-Ring Resonators

Silicon nitride ($Si_3N_4$) waveguides are presented as an optimal platform for integrated nonclassical light sources [82]. Its high refraction index ($n_0 = 1.9960$ at $\lambda = 1560$ nm) facilitates the confinement of light [83], which is subjected to very low propagation losses ($< 0.5$ dB cm$^{-}$1). A third-order nonlinear factor of $n_2 = 2.5 \times 10^{-19}$ m$^2$W$^{-1}$ [84] is excellent for experiments involving nonlinear optics. The material also has a huge transparency window, from visible to the upper limit of short-infrared ($\sim 400 - 2500$ nm), which enables broadband exploration. Besides, small Raman and Brillouin scattering rid us, to a certain degree, from undesired nonparametric effects, detrimental to squeezing [85].

As schematically shown in figure 2.1, our rectangular shaped waveguides are composed by a silicon nitride core buried in a silicon oxide substrate ($n_0 = 1.4439$ at $\lambda = 1560$ nm). The substrate provides a protection layer for the core waveguides and enables the placing of integrated microheaters above the microcavities, important for resonance tuning and stabilization of our system [1]. Furthermore, these materials have a good contrast between their refractive index on a huge frequency range, making them ideal to guide light by total internal reflection. Details of the waveguides fabrication can be found in [86].

Resonant cavities are built with closed paths of the rectangular cross section $Si_3N_4$ on $SiO_2$ waveguides. Such devices have the capability of trapping light for long periods of time. Due to the tight confinement of light in the compact structures of the waveguides, the intracavity intensities reach high levels enhancing light-matter interactions. This composes a propitious scenario to reach parametric oscillation.

Although several geometries can be employed to this purpose, let us consider an add-through micro-ring resonator, which consists of a ring-shaped cavity close to a single

[1] This topic will be covered in detail in section 3.2

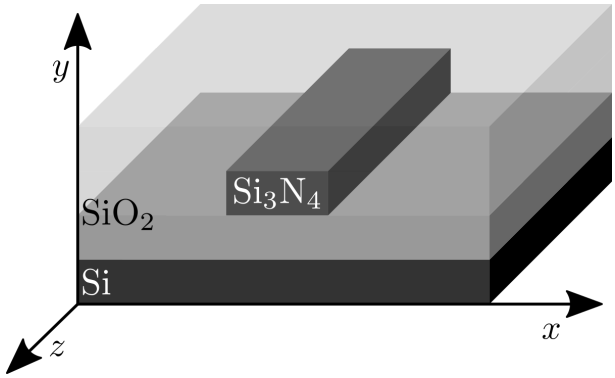


Figure 2.1: Three-dimensional scheme of a rectangular $Si_3N_4$ core buried $in SiO_2$. The silicon (Si) base is part of the fabrication process.

input-output coupling bus waveguide, as schematically shown in figure 2.2. A fraction of

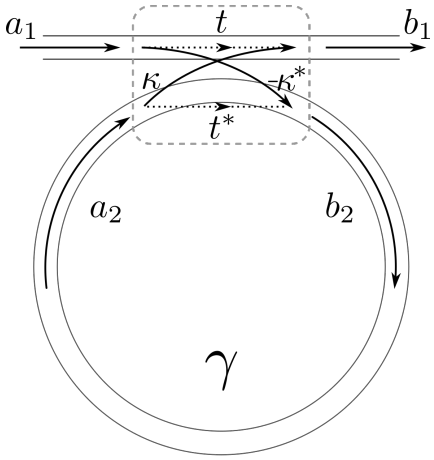


Figure 2.2: Input-output schematic of the add-through micro-ring resonator. The input field $a_1$ is coupled into the cavity with the parameter $-\kappa^*$. After circulation, the field is coupled back to the bus waveguide by the conjugate parameter $\kappa$. Parameters $t$ and its conjugate are respectively related to the uncoupled fields in the bus waveguide and the resonator. Intrinsic losses are indicated by $\gamma$. The output field, $b_1$, is a mixture of part of the field coupled into the resonator and then coupled back to the bus waveguide and the part that does not enter the microcavity.

the energy of the incident field $a_1$ is evanescently coupled into the micro-ring by a factor $-\kappa^*$ through frustrated total internal reflection [87]. The coupled field ($b_2$) is subjected to intrinsic losses ($\gamma$)[2] and dephasing ($\theta$) while trapped in the ring. A full circulation is described as

$$a_2 = \sqrt{1-\gamma}e^{i\theta}b_2, \tag{2.1}$$

with the acquired phase given by

$$\theta = \frac{\omega_p}{c_0}n_0 L, \tag{2.2}$$

[2]In general, this coefficient can also represent the canonical gain if we allow $\gamma < 0$ [88, 89].

where $n_0$ is the effective refraction index, $\omega_p$ is the wavelength of the cavity pump field, $c_0$ is the speed of light in vacuum and $L$ is the perimeter of the ring. Since the cavity entry and exit are the same, the output field ($b_1$) is also proportional to $\kappa$. Constants $t$ and $t^*$ are respectively related to the uncoupled part of the pump and the permanence of the coupled field in the ring.

Let us consider an ideal situation without taking into account the losses in the coupling region (dashed square) and considering only one direction for the propagating pump, disregarding back reflections in the bus waveguide walls. The dynamics of the fields will then be described by the coupling matrix [88, 89]

$$\begin{bmatrix} b_1 \\ b_2 \end{bmatrix} = \begin{bmatrix} t & \kappa \\ -\kappa^* & t^* \end{bmatrix} \begin{bmatrix} a_1 \\ a_2 \end{bmatrix}, \tag{2.3}$$

with the energy conservation constraint

$$|\kappa|^2 + |t|^2 = 1. \tag{2.4}$$

Developing equations (2.1)–(2.4), we obtain the normalized fields

$$\frac{b_1}{a_1} = \frac{-\sqrt{1-\gamma} + te^{i\theta}}{-t^*\sqrt{1-\gamma} + e^{-i\theta}}; \tag{2.5}$$

$$\frac{b_2}{a_1} = \frac{-\kappa^*}{1 - t^* e^{i\theta}\sqrt{1-\gamma}}; \tag{2.6}$$

$$\frac{a_2}{a_1} = \frac{-\kappa^*\sqrt{1-\gamma}}{-t^*\sqrt{1-\gamma} + e^{i\theta}}. \tag{2.7}$$

The transmission of the microcavity is then given by

$$T \equiv \left|\frac{b_1}{a_1}\right|^2 = \frac{(1-\gamma) + (1-|\kappa|^2) - 2\sqrt{(1-\gamma)(1-|\kappa|^2)}\cos\theta}{1 + (1-\gamma)(1-|\kappa|^2) - 2\sqrt{(1-\gamma)(1-|\kappa|^2)}\cos\theta}, \tag{2.8}$$

where the phase $\theta$ is the cavity-pump detuning. In resonance $\theta = m2\pi$, with $m \in \mathbb{Z}$, the transmission is reduced to

$$T_{\text{ress}} = \left[\frac{\sqrt{1-\gamma} - \sqrt{1-|\kappa|^2}}{1 - \sqrt{(1-\gamma)(1-|\kappa|^2)}}\right]^2, \tag{2.9}$$

from which we observe the dependence of $T$ with the coupling strength and intrinsic losses. Following the definitions in [90] we identify three different coupling regimes:

- **Critically Coupled** ($|\kappa|^2 = \gamma$)**:** when intrinsic losses are equal to the coupling strength we have perfect impedance match of these factors. This translates as a completely destructive interference at the output of the cavity.

- **Overcoupled** ($|\kappa|^2 > \gamma$)**:** As the coupling strength increases the photons will stay less time in the intracavity medium. Consequently, the probability of extracting the photons from the cavity back to the bus waveguide is increased.

- **Undercoupled** ($|\kappa|^2 < \gamma$)**:** As is harder to couple the photons into the cavity, the harder it is to extract them. Hence, they have a greater probability of being lost through other interactions.

The transmission as a function of the cavity detuning is shown in figure 2.3 for each of the discussed regimes. The dips are a result of the interference between the part of field exiting the cavity and the uncoupled part of the field in the bus waveguide. In practice, the coupling strength is controlled by the gap between the bus waveguide and the micro-ring. As we explore the gap as a figure of merit for the coupling strength we can also

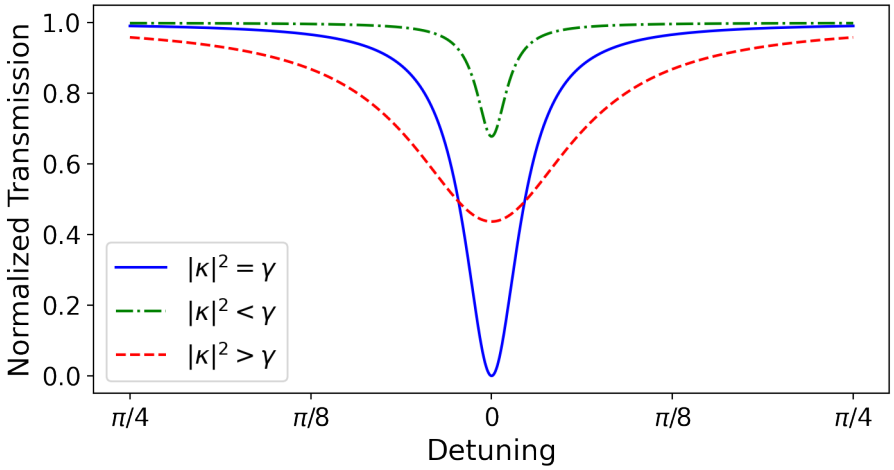


Figure 2.3: Microcavity output as a function of the detuning for a ring with losses fixed at $\gamma = 0.07$. For the overcoupled resonator (red dashed line) we have $|\kappa|^2 = 0.3$ and for the undercoupled (green dash-dotted line), $|\kappa|^2 = 0.007$.

characterize the losses with the help of transmission curves, which gives us information about the quality factor of the microcavities.

The quality factor is the ratio of the energy stored in the resonator to the energy dissipated per cycle by damping processes. In the add-through micro-ring resonator the total losses are accounted in the loaded quality factor ($Q_L$). It is related to the intrinsic quality factor ($Q_I$), that accounts only for the intrinsic losses of the system, and the coupling quality factor ($Q_C$), accounting only for the coupling losses, by [88, 89]

$$\frac{1}{Q_L} = \frac{1}{Q_I} + \frac{1}{Q_C}. \tag{2.10}$$

The loaded quality factor can be determined by [88, 89]

$$Q_L = \frac{\omega_m}{\Delta_{\mathrm{BW}}^{\omega_m}}, \tag{2.11}$$

where $\omega_m$ is the resonant mode frequency and $\Delta_{\mathrm{BW}}^{\omega_m}$ is the experimentally accessible cavity bandwidth for the mode $m$. This equation directly relates with the total losses of the cavity by

$$Q_L = \frac{\omega_m}{\Delta_{\mathrm{FSR}}^{\omega_m}} \frac{2\pi}{|\kappa|^2 + \gamma}, \tag{2.12}$$

with $\Delta_{\mathrm{FSR}}^{\omega_m}$ defining the cavity free spectral range for the resonant mode $m$. At critical coupling ($Q_{LC}$) we have $|\kappa|^2 = \gamma$, which yield direct access to the intrinsic losses of the system. We define the intrinsic quality factor ($Q_I$) disregarding the coupling factor, $|\kappa|^2 = 0$, resulting in the simple relation

$$Q_I = 2Q_{LC}. \tag{2.13}$$

Therefore, $Q_I$ is experimentally accessible through the measurement of $Q_{LC}$, giving us a practical way to determine the intrinsic losses $\gamma$.

## 2.2 Optical Parametric Oscillators

Nonlinear interactions of light and matter causes the spontaneous excitation of photons in different modes of the field. Such process depends on details of the system, such as frequency and intensity of light and the structure of the pumped media. Since light weekly interacts with transparent media without the presence of resonances with electronic transitions of the material, nonlinear effects can be enhanced introducing a feedback loop in the light-matter interaction. This three element forms an optical parametric oscillator (OPO). As an example, consider a $\chi^{(3)}$ nonlinear media inside an optical cavity. As we pump the system, photons will populate the sideband modes selected by the cavity boundary conditions. If the parametric gain exceeds the total losses of the medium (threshold) we will have the amplification of the generated fields. Such example is represented in figure 2.4.

In general, the OPO is described by the master equation [4, 20]

$$\frac{\mathrm{d}}{\mathrm{d}t}\hat{\rho} = -\frac{i}{\hbar}\left[\hat{H}_{\mathrm{free}} + \hat{H}_{\mathrm{int}} + \hat{H}_{\mathrm{ext}}, \hat{\rho}\right] + \sum_j \hat{\Lambda}_j(\hat{\rho}). \tag{2.14}$$

The first term in the right hand side describes the free field modes inside the cavity

$$\hat{H}_{\mathrm{free}} = \frac{\hbar}{\tau}\sum_j \Delta_j \hat{a}_j^\dagger \hat{a}_j, \tag{2.15}$$

where $\tau$ is the round-trip time of the light inside the cavity, $\Delta$ is the cavity detuning and $j$ covers all the intracavity modes involved. The annihilation $\hat{a}_j$ and creation $\hat{a}_j^\dagger$ operators

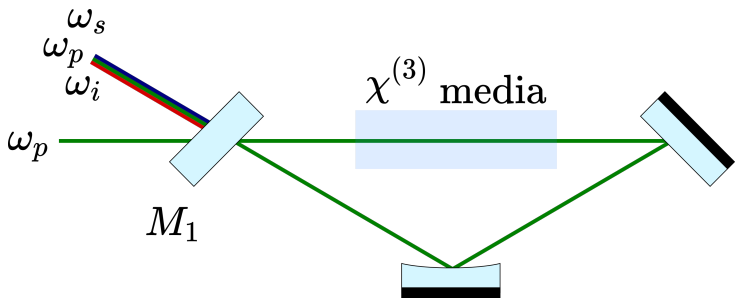


Figure 2.4: Representation of a $\chi^{(3)}$ OPO. An optical pump of frequency $\omega_p$ is coupled into the triangular optical cavity through the input mirror ($M_1$). The interaction of the pump field with the nonlinear media excite signal ($\omega_s$) and idler ($\omega_i$) modes through a degenerate four-wave mixing process. The intracavity power is amplified by the cavity loop for all fields in a triple resonant condition. The three intense beams then exit the cavity through the coupling mirror. The curved bottom mirror is represented as a parallel to usual triangular cavities build in the laboratory.

respect the conventional commutation rule $[\hat{a}_j, \hat{a}_k^\dagger] = \delta_{j,k}$. For the example of figure 2.4, the $j$ index indicates the pump, signal and idler modes. Next we have the interaction between the fields. This term will depend on the characteristics of the nonlinear medium and is responsible for energy exchanges between modes. The last term of the Hamiltonian is the pumping of the cavity by external fields. Assuming there is a single strong pump field $\epsilon$, it is given by

$$\hat{H}_{\text{ext}} = i\hbar\frac{\Gamma_p}{\tau}\epsilon\left[\hat{a}_p^\dagger - \hat{a}_p\right] \tag{2.16}$$

with $\Gamma_p$ corresponding to the total cavity losses for this mode. Additional input couplings can be taken as vacuum fluctuations. At last we have superoperators representing the losses of the system for each mode. They are modeled by the independent coupling of each intracavity field with an harmonic oscillator reservoir. When the interaction between the respective fields and reservoirs is given by a Jaynes-Cummings Hamiltonian

$$H_{\text{J-C}}^j = \hbar\sum_k\left[g_j^k\hat{a}_j\hat{b}_j^{k\dagger} + g_j^{k*}\hat{a}_j^\dagger\hat{b}_j^k\right], \tag{2.17}$$

where $j = \{p, s, i\}$ and $\hat{b}_j^k$ is related to the reservoir mode $k$ coupled to the cavity mode $\hat{a}_j$ through the constant $g_j^k$, the losses of each mode $j$ assumes the form

$$\hat{\Lambda}_j(\hat{\rho}) = \frac{\Gamma_j}{\tau}\left[2\hat{a}_j\hat{\rho}\hat{a}_j^\dagger - \hat{a}_j^\dagger\hat{a}_j\hat{\rho} - \hat{\rho}\hat{a}_j^\dagger\hat{a}_j\right]. \tag{2.18}$$

Depending on the complexity of the interaction term, solving equation (2.14) can be a very difficult task. Nevertheless, for $\chi^{(2)}$ [4, 20, 91] and $\chi^{(3)}$ [21, 92] nonlinear media, under proper considerations, one can translate this problem into a set of stochastic differential equations known as Heisenberg-Langevin equations. Such approach is useful when only

a small number of modes are excited. OPOs based on four-wave mixing may violate this condition since secondary modes, beyond signal and idler, are easily excited with an increase in the pump power [23, 93]. With an even further growth of the pump power, frequency combs can be generated [83, 94, 95]. In such cases other formalisms are more convenient, such as modified Lugiato-Lefever equations [96, 97] and numerical methods for solving the nonlinear Schrödinger equation [98]. Since we are interested in the dynamics of signal and idler fields, we will focus our attention in the first presented situation.

In the next section we will explore the conditions for sideband excitation on our chips. The quantum dynamics of pump, signal and idler will be given in section 2.2.2

### 2.2.1 Four-Wave Mixing

Amorphous materials, atomic clouds and a variety of crystal structures are symmetric when inverted with respect to an arbitrary axis. This lack of symmetry inversion precludes the existence of second-order nonlinear effects and only third-order ones are relevant [99]. In the case of silicon chips, $\chi^{(3)}$ effects are predominant[3] and will be developed in the context of parametric oscillation, where the four-wave mixing has a central role.

The Hamiltonian that describes the relevant effects is given by [92]

$$\begin{aligned}\hat{H}_{\text{int}} = &-\hbar\zeta^{(3)}\left[\frac{1}{2}\left(\hat{a}_p^\dagger\hat{a}_p^\dagger\hat{a}_p\hat{a}_p + \hat{a}_s^\dagger\hat{a}_s^\dagger\hat{a}_s\hat{a}_s + \hat{a}_i^\dagger\hat{a}_i^\dagger\hat{a}_i\hat{a}_i\right)\right. \\ &\left. + 2\left(\hat{a}_p^\dagger\hat{a}_s^\dagger\hat{a}_p\hat{a}_s + \hat{a}_p^\dagger\hat{a}_i^\dagger\hat{a}_p\hat{a}_i + \hat{a}_s^\dagger\hat{a}_i^\dagger\hat{a}_s\hat{a}_i\right) + \left(\hat{a}_s^\dagger\hat{a}_i^\dagger\hat{a}_p\hat{a}_p + \hat{a}_p^\dagger\hat{a}_p^\dagger\hat{a}_s\hat{a}_i\right)\right].\end{aligned} \tag{2.19}$$

The nonlinear index ($n_2$) and the modes volume ($\mathcal{V}$) are included in the coefficient

$$\zeta^{(3)} \approx \frac{\omega^2 n_2 c}{n_0^2 \mathcal{V}}. \tag{2.20}$$

All coefficients are merged together in equation (2.19) as we took a common central frequency for all modes ($\omega$), which is reasonable if all the modes are spectrally close. The nonlinear Kerr effect are considered to be linear with the intensity ($I$) as $n = n_0 + In_2$ and that the nonlinear indexes are equal for all involved fields. Furthermore, all the modes involved are assumed to be spatially overlapped, which is true in very good approximation for the fields involved in our problem, since their frequency difference is small.

The first term inside parenthesis in equation (2.19) is the self-phase modulation (SPM) term, which represents a self induced Kerr effect. The cross-phase modulation (XPM) is a phase shift induced between two fields. The phase modulation terms do not affect the intensity of the fields, since they commute with the number operators. On the other

[3] Although not relevant to the present work, the interface between silicon nitride and silicon oxide is not symmetric under inversion and second order effects can be explored in such photonic systems [100].

hand, the four-wave mixing (FWM) term in the last parenthesis is responsible for energy exchange. The creation of signal and idler photons are simultaneous to the annihilation of two pump photons, that do not need to be degenerated in the general case. This process is schematically represented in the energy diagram of figure 2.5. Other nonlinear effects,

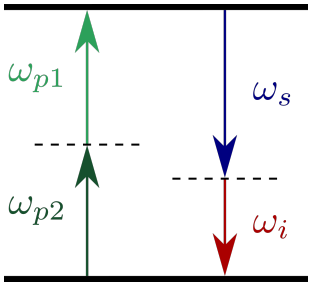


Figure 2.5: Energy diagram for the four-wave mixing process. Two pump photons $\omega_{p1}$ and $\omega_{p2}$ are annihilated and signal $\omega_s$ and idler $\omega_i$ photons are created (or vice-versa). Energy is conserved in the process, such that $\omega_{p1} + \omega_{p2} = \omega_s + \omega_i$. The degenerate case is equivalent to the condition $\omega_{p1} = \omega_{p2}$

such as third harmonic generation, can be neglected when the frequencies are spectrally distant from signal and idle.

Before we tackle the full OPO dynamics, let us first analyze the propagation equations of the interaction Hamiltonian by directly solving Heisenberg's equation, which results in

$$\frac{d\hat{a}_p}{dz} = i\zeta^{(3)}\left[\left(\hat{a}_p^\dagger\hat{a}_p + 2\hat{a}_s^\dagger\hat{a}_s + 2\hat{a}_i^\dagger\hat{a}_i\right)\hat{a}_p + \hat{a}_p^\dagger\hat{a}_s\hat{a}_i e^{i\Delta\beta z}\right], \tag{2.21}$$

$$\frac{d\hat{a}_s}{dz} = i\zeta^{(3)}\left[\left(2\hat{a}_p^\dagger\hat{a}_p + \hat{a}_s^\dagger\hat{a}_s + 2\hat{a}_i^\dagger\hat{a}_i\right)\hat{a}_s + \hat{a}_p\hat{a}_p\hat{a}_i^\dagger e^{-i\Delta\beta z}\right], \tag{2.22}$$

$$\frac{d\hat{a}_i}{dz} = i\zeta^{(3)}\left[\left(2\hat{a}_p^\dagger\hat{a}_p + 2\hat{a}_s^\dagger\hat{a}_s + \hat{a}_i^\dagger\hat{a}_i\right)\hat{a}_i + \hat{a}_p\hat{a}_p\hat{a}_s^\dagger e^{-i\Delta\beta z}\right]. \tag{2.23}$$

We introduced $\Delta\beta = 2\beta_p - \beta_s - \beta_i$ to include the phase mismatch induced by the cavity dispersion, a consequence of the material dispersion and the microresonator geometry. The longitudinal propagation constants are defined as $\beta_j = n_{0j}\omega_j/c$. Since the operators $\hat{a}_j$ are proportional to the mean fields $\alpha_j$, we retrieve the classical dynamics of the system by disregarding the quantum fluctuations in the substitution $\hat{a}_j \to \alpha_j$. Further considering an undepleted pump approximation, where $\alpha_p \gg \alpha_s, \alpha_i$, we can drop the second order terms in signal and idler fields. The pump equation is then given by

$$\frac{d\alpha_p}{dz} \approx i\zeta^{(3)}|\alpha_p|^2\alpha_p, \tag{2.24}$$

and the solution is

$$\alpha_p(z) = \alpha_p(0)e^{i\zeta^{(3)}P_p z}, \tag{2.25}$$

where $P_p = |\alpha_p(0)|^2$ is the *intracavity power*. It is important to notice that in the case of microreonators this value is usually large due to the high confinement of light. Therefore,

small input pump powers are expected. As we can observe, the SPM plays an important role in the field propagation, which will suffer an extra phase shift while propagating through the third order nonlinear media.

Under the same considerations, signal and idler fields will evolve according to

$$\frac{d\alpha_s}{dz} \approx i\zeta^{(3)}\left[2|\alpha_p|^2\alpha_s + \alpha_p^2(0)e^{i(2\zeta^{(3)}P_p-\Delta\beta)z}\alpha_i^*\right], \tag{2.26}$$

$$\frac{d\alpha_i}{dz} \approx i\zeta^{(3)}\left[2|\alpha_p|^2\alpha_i + \alpha_p^2(0)e^{i(2\zeta^{(3)}P_p-\Delta\beta)z}\alpha_s^*\right]. \tag{2.27}$$

This linear system can be analytically solved as [101]

$$\alpha_s(z) = \mu(z)\alpha_s(0) + \nu(z)\alpha_i^*(0), \tag{2.28}$$

$$\alpha_i(z) = \mu(z)\alpha_i(0) + \nu(z)\alpha_s^*(0), \tag{2.29}$$

where

$$\mu(z) = \left[\cosh(gz) + \frac{i(2\zeta^{(3)}P_p - \Delta\beta)}{2g}\sinh(gz)e^{i\left(\zeta^{(3)}P_p+\frac{\Delta\beta}{2}\right)z}y\right], \tag{2.30}$$

$$\nu(t) = \frac{i\zeta^{(3)}\alpha_p^2(0)}{g}\sinh(gz)e^{i(\zeta^{(3)}P_p+\frac{\Delta\beta}{2})z}. \tag{2.31}$$

Parametric gain by length unit is given by the $g$ parameter and its explicit expression has the form

$$g = \sqrt{\zeta^{(3)}P_p\Delta\beta - \frac{\Delta\beta^2}{4}}. \tag{2.32}$$

It is evident from this equation that we only have gain for $\Delta\beta > 0$. Considering that this criteria is respected, $\left(2\zeta^{(3)}P_p - \Delta\beta\right)$ will get closer to zero, which will at least partially compensate for the detunings induced by SPM and XPM. We expand the propagation constants around $\omega_p$ with the simplified notation for the first and second order derivatives $\beta_j^{(1)}$ and $\beta_j^{(2)}$, with $j = s, i$, such as

$$\beta_j = \beta_j + \beta_j^{(1)}(\omega_j - \omega_p) + \frac{1}{2}\beta_j^{(2)}(\omega_j - \omega_p)^2 + \cdots, \tag{2.33}$$

Taking advantage of the energy conservation relation $2\omega_p = \omega_s + \omega_i$, when high order terms are omitted we reach $\Delta\beta \approx -\beta_p^{(2)}(\omega_s - \omega_i)^2$. The second order derivative coefficient $\beta_p^{(2)}$ is known as group velocity dispersion (GVD) and its negativity gives a simple condition to guarantee parametric gain. Equivalently, we need anomalous dispersion ($\beta^{(2)} < 0$) between the pump field and material nonlinear interaction in order to have efficient FWM. Such parameter can be tailored by designing the geometry of the waveguides [102], which plays an important role in the dispersion effects.

Figure 2.6 shows the parametric gain as a function of the wavelength for a typical value of $\zeta^{(3)}$ for silicon nitride materials. The central pump frequency, the $\beta^{(2)}$ and intracavity

Table 2.1: Material resonances and Sellmeier constants.

| **Material** | $\lambda_1$ ($\mu$m) | $B_1$ ($\mu$m) | $\lambda_2$ ($\mu$m) | $B_2$ ($\mu$m) |
|---|---|---|---|---|
| $Si_3N_4$ | 0.1353406 | 3.0249 | 1239.842 | 40314 |
| $SiO_2$ | 1.09877 | 0.0924317 | – | – |

power ($P_p$) values are compatible with the experimentally available resonators. It is evident from figure 2.6 that the spectral distance between signal and idler increases with the intracavity power and decreases with $\beta^{(2)}$ absolute value.

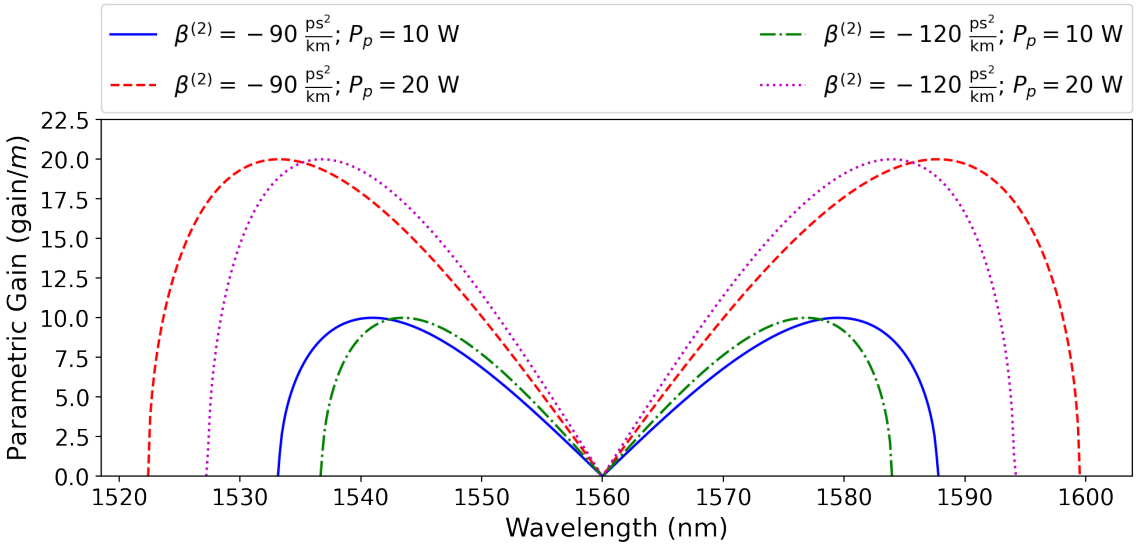


Figure 2.6: Parametric gain, equation (2.32), per length unity of the four-wave mixing process for several values of intracavity power ($P_p$) and group velocity dispersion ($\beta^{(2)}$) around the pump wavelength of $\omega_p = 1560$ nm. The peak of the gain, is shifted away from $\omega_p$ with the increment of $P_p$ or reduction of $\left|\beta^{(2)}\right|$. FWM bandwidth grows for the same conditions. We choose a nonlinear parameter compatible with silicon nitride ($\zeta^{(3)} = 1$) [103].

Materials dispersion are modeled according to Sellmeier equations

$$n^2 - 1 = \sum_j \frac{\lambda^2 B_j}{\lambda^2 - \lambda_j^2}, \tag{2.34}$$

where the $B_j$ values, shown in table 2.1, are empirically obtained in [83] for $Si_3N_4$ and in [104] for $SiO_2$. Silicon nitride and silicon oxide dispersion curves as a function of the wavelength are shown in figure 2.7 for a wide range of frequencies.

As an example, we calculated the group velocity dispersion for different silicon nitride on silicon oxide resonators. We used the MIT Electromagnetic Equation Propagation (Meep) open software [105], which solves Maxwell's equations through a finite-difference time-domain method for different waveguide geometries. Another important factor is the

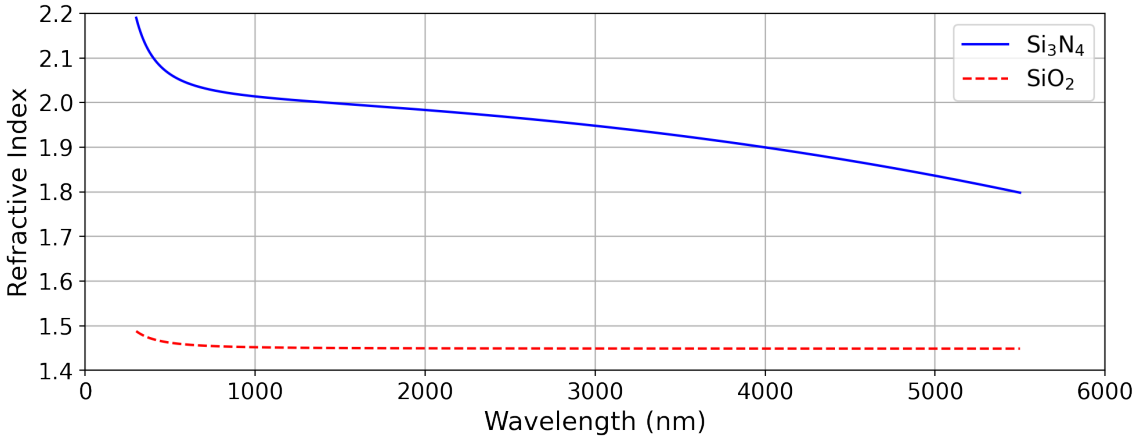


Figure 2.7: Behavior of the refraction index as a function of the wavelength for silicon nitride (blue continuous line) and silicon oxide (red dashed line).

microcavity geometry, where we restrict ourselves to ring-shaped resonators as they are simpler to define in the simulation routine. At last, we only explored the fundamental spatial modes of light. We runned the routine for two different cross section geometries available in our laboratory. In figure 2.8 (a) we show the results for the GVD of both quasi-transverse fundamental modes of a micro-ring with 100 $\mu$m radius with waveguides of 1300 nm width and 730 nm height. Although the dispersion is anomalous for the $TE_{00}$ mode, no oscillations are expected for the $TM_{00}$ mode when pumped with a 1560 nm field. In figure 2.8 (b) we see changes in the GVD purely induced by changes in the cross section dimensions.

Once parametric gain is guaranteed by the boundary conditions of the micro-resonator, we can explore the system as a third order optical parametric oscillator. In the next section we will treat the dynamics of the third order OPO and present some important results.

### 2.2.2 Third-Order Optical Parametric Oscillator

The four-wave mixing dynamics presented in last section allowed the derivation of the conditions for parametric oscillation. Now, we will take a further step and develop the full OPO dynamics given by the master equation (2.14). Following the treatment in [21, 92], a set of Heisenberg-Langevin equations are derived from equations (2.15) – (2.19), given

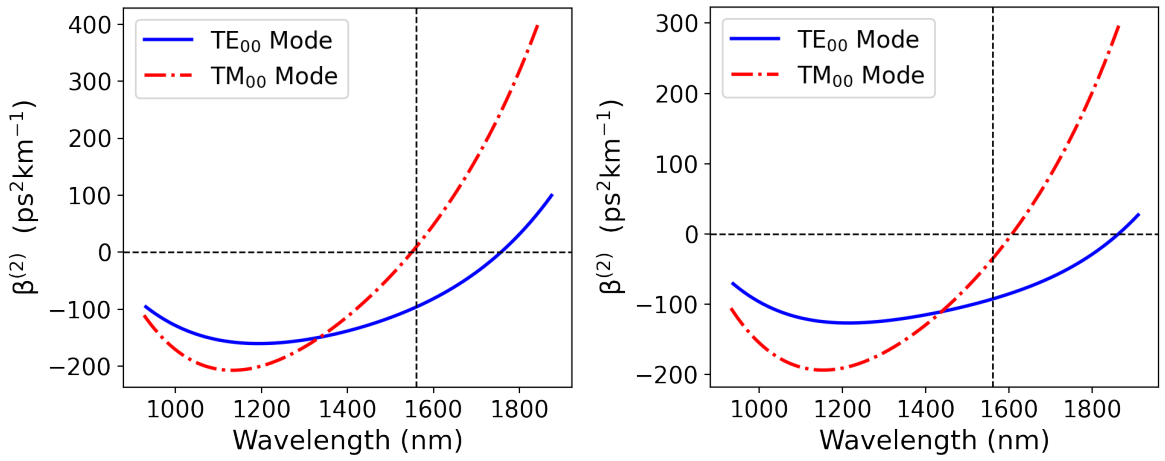


(a) (b)

Figure 2.8: Group velocity dispersion as a function of the wavelength for micro-rings with 100 $\mu$m radii and rectangular cross sections of (a) 1300 nm width by 730 nm height and (b) 1700 nm width by 730 nm height. Both figures show the results for quasi-transverse $TE_{00}$ (solid blue lines) and $TM_{00}$ (dash-dotted red lines) modes. The dashed black lines intersections are relative to the GVD at 1560 nm. Note that the $TM_{00}$ mode does not have anomalous dispersion for the 1300 × 730 waveguide, figure (a).

by

$$\begin{aligned}\frac{\mathrm{d}}{\mathrm{d}t}\hat{a}_p =& -(\Gamma_p + i\Delta_p)\hat{a}_p + i\zeta^{(3)}\left[\left(\hat{a}_p^\dagger\hat{a}_p + 2\hat{a}_s^\dagger\hat{a}_s + 2\hat{a}_i^\dagger\hat{a}_i\right)\hat{a}_p + 2\hat{a}_p^\dagger\hat{a}_s\hat{a}_i\right] \\ &+ \sqrt{2\kappa_p}\hat{a}_p^{\mathrm{in}} + \sqrt{2\gamma_p}\hat{a}_p^{\mathrm{loss}},\end{aligned} \tag{2.35}$$

$$\begin{aligned}\frac{\mathrm{d}}{\mathrm{d}t}\hat{a}_s =& -(\Gamma_s + i\Delta_s)\hat{a}_s + i\zeta^{(3)}\left[\left(2\hat{a}_p^\dagger\hat{a}_p + \hat{a}_s^\dagger\hat{a}_s + 2\hat{a}_i^\dagger\hat{a}_i\right)\hat{a}_s + \hat{a}_p\hat{a}_p\hat{a}_i^\dagger\right] \\ &+ \sqrt{2\kappa_s}\hat{a}_s^{\mathrm{in}} + \sqrt{2\gamma_s}\hat{a}_s^{\mathrm{loss}},\end{aligned} \tag{2.36}$$

$$\begin{aligned}\frac{\mathrm{d}}{\mathrm{d}t}\hat{a}_i =& -(\Gamma_i + i\Delta_i)\hat{a}_i + i\zeta^{(3)}\left[\left(2\hat{a}_p^\dagger\hat{a}_p + 2\hat{a}_s^\dagger\hat{a}_s + \hat{a}_i^\dagger\hat{a}_i\right)\hat{a}_i + \hat{a}_p\hat{a}_p\hat{a}_s^\dagger\right] \\ &+ \sqrt{2\kappa_i}\hat{a}_i^{\mathrm{in}} + \sqrt{2\gamma_i}\hat{a}_i^{\mathrm{loss}}.\end{aligned} \tag{2.37}$$

The above set of equations describes the dynamics for each mode, coupled through phase modulations and energy exchanges. The field detunings with respect to the cavity modes ($\tilde{\omega}_j$) are given by $\Delta_j = \tilde{\omega}_j - \omega_j$. Although energy conservation is respected, $2\omega_p = \omega_s + \omega_i$, the phase mismatched system entails $2\Delta_p \neq \Delta_s + \Delta_i$. As in section 2.1, the coefficients $\kappa_j$ are related to the coupling between the bus waveguide and the micro-ring and $\gamma_j$ accounts for other sources of loss such as scattering and absorption. The total losses are simply given by $\Gamma_j = \kappa_j + \gamma_j$. The respective operators $\hat{a}_i^{\mathrm{in}}$ and $\hat{a}_j^{\mathrm{loss}}$ correspond to the incoming and the loss modes. Except for the mean field for the incoming pump, all the other income

and loss operators have zero expectation values

$$\begin{cases} \left\langle \hat{a}_p^{\text{in}} \right\rangle = \sqrt{P_p^{\text{in}} \hbar \omega_p}, \\ \left\langle \hat{a}_j^{\text{in}} \right\rangle = 0, \qquad j = \{s, i\}, \\ \left\langle \hat{a}_j^{\text{loss}} \right\rangle = 0, \quad j = \{p, s, i\}. \end{cases} \tag{2.38}$$

As described in the beginning of the section 2.2, all reservoirs are independent for each mode, and the same is assumed for the coupling between waveguides. Therefore, all income and loss operators are uncorrelated

$$\begin{cases} \left\langle \hat{a}_j^{\dagger \text{in}}(t) \hat{a}_k^{\text{in}}(t') \right\rangle = \delta_{j,k} \delta(t - t'), \\ \left\langle \hat{a}_j^{\dagger \text{loss}}(t) \hat{a}_k^{\text{loss}}(t') \right\rangle = \delta_{j,k} \delta(t - t'), \quad j, k = \{p, s, i\}. \end{cases} \tag{2.39}$$

In order to solve this equations, the next step is to linearize our problem in a classical part added to its *small* quantum fluctuations

$$\hat{a}_j = \alpha_j + \delta \hat{a}_j, \quad j = \{p, s, i\}. \tag{2.40}$$

This procedure allows us to separate the problem in independent classical and quantum analysis. From a classical point of view, there is no advantage in this part of the process, since it is equivalent to taking the expectation values of the operators in equations (2.35) – (2.37). On the other hand, simplifications can be done in the quantum fluctuations. Since the fluctuations are small, we can drop second and third order terms.

For the mean fields, it is interesting to study the steady state solutions. Substituting 2.40 in (2.35) – (2.37), taking into account the relations given in (2.38) and dropping the null expectation values quantum fluctuations, we have, for the steady states

$$-(\Gamma_p + i\Delta_p)\alpha_p + i\zeta^{(3)} \left[ \left( \left|\alpha_p\right|^2 + 2|\alpha_s|^2 + 2|\alpha_i|^2 \right) \alpha_p + 2\alpha_p^* \alpha_s \alpha_i \right] + \sqrt{2\kappa_p} \alpha_p^{\text{in}} = 0, \tag{2.41}$$

$$-(\Gamma_s + i\Delta_s)\alpha_s + i\zeta^{(3)} \left[ \left( \left|2\alpha_p\right|^2 + |\alpha_s|^2 + 2|\alpha_i|^2 \right) \alpha_s + 2\alpha_p^2 \alpha_i^* \right] = 0, \tag{2.42}$$

$$-(\Gamma_i + i\Delta_i)\alpha_i + i\zeta^{(3)} \left[ \left( \left|2\alpha_p\right|^2 + 2|\alpha_s|^2 + |\alpha_i|^2 \right) \alpha_i + 2\alpha_p^2 \alpha_s^* \right] = 0. \tag{2.43}$$

A few properties can be retrieved from this set of equations with the aid of numerical methods. Phase modulations and thermo-optical effect shift the mode frequencies taking them out of resonance, leading to unstable solutions. Although not explicitly considered in this treatment, the temperature dependency can be easily included in the $\Delta_j$ parameters [92]. The resonance instabilities can be compensated by pumping the system with some detuning, either by tuning the pump frequency or by tuning the cavity resonant modes.

Another interesting aspect of the dynamics of the system is that the output of a microcavity cannot always be described as a Lorentzian shaped curve around its resonance.

A strong bistability effect, as explored in [106] in the context of micro-ring resonators, is expected due to the same resonance shifts responsible for the instabilities. This effect is also retrieved from equations (2.41) – (2.43) [107]. The bistable character of the chip operating above threshold will be shown in section 3.2.2.

At last, the optical power threshold can be derived by finding simultaneous stable solutions for pump, signal and idler fields in equations (2.41)–(2.43) using perturbation methods, as was done in references [92, 107], resulting in

$$P_{th} = 1.54\frac{\pi}{2}\frac{\kappa_p + \gamma_p}{2\kappa_p}\frac{n_0^2\mathcal{V}}{n_2\lambda Q_L^2}. \tag{2.44}$$

One can see that the threshold is directly related with the coupling ($\kappa_p$) and intrinsic losses ($\gamma_p$) of the system, which are also included in the loaded quality factor ($Q_L$), equation (2.12). The spacial volume ($\mathcal{V}$) is related with the geometry of the system. Refractive index and nonlinear index depends on the material. At last, the numerical factor of 1.54 is related to the phase modulations and is acquired from the numerical calculations.

For the quantum fluctuations we substitute the linear equation (2.40) into equations (2.35) – (2.37). We drop the terms superior to first order ones and separate the classical part of the dynamics, equivalent to equations (2.41) – (2.43). In the same spirit of the canonical variables vector of equation (1.1), we define the vector of quantum fluctuations as

$$\delta\hat{\mathbf{x}} = \left[\delta\hat{a}_p e^{-i\theta_p}, \delta\hat{a}_p^\dagger e^{i\theta_p}, \delta\hat{a}_s e^{-i\theta_s}, \delta\hat{a}_s^\dagger e^{i\theta_s}, \delta\hat{a}_i e^{-i\theta_i}, \delta\hat{a}_i^\dagger e^{i\theta_i}\right]^{\mathrm{T}}, \tag{2.45}$$

where $\theta_j$ is the phase of the mean field $\alpha_j = |\alpha_j|e^{i\theta_j}$. The evolution of the fluctuations are then given by [21]

$$\frac{\mathrm{d}}{\mathrm{d}\tau}\delta\hat{\mathbf{x}} = -\mathbb{M}\cdot\delta\hat{\mathbf{x}} + \frac{\mathbb{T}^{\mathrm{in}}}{\Gamma}\cdot\delta\hat{\mathbf{x}}^{\mathrm{in}} + \frac{\mathbb{T}^{\mathrm{loss}}}{\Gamma}\cdot\delta\hat{\mathbf{x}}^{\mathrm{loss}}, \tag{2.46}$$

with $\tau \equiv t\Gamma$ being the normalized time. In order to simplify the notation we took the normalized quantities $|\alpha|_p \to \sqrt{\zeta^{(3)}/\Gamma}|\alpha|_p$; $\Delta_p \to \Gamma\Delta_p$; $|\alpha|_s = |\alpha|_i \to \sqrt{\zeta^{(3)}/\Gamma}|\alpha|$; $\Delta_s = \Delta_i \to \Gamma\Delta$, where we considered equal amplitude and detunings for signal and idler.

Further approximations are made considering the coupling and intrinsic losses to be equal for all modes ($\Gamma = \Gamma_p = \Gamma_s = \Gamma_i$), which follows from the same reasoning of last section, where we considered all modes to be spatially overlapped. Hence, the coupling and losses are given by the matrices

$$\mathbb{T}^{\mathrm{in}} = \mathrm{Diag}\left\{\sqrt{2\kappa}e^{-\phi}, \sqrt{2\kappa}e^{\phi}, \sqrt{2\kappa}, \sqrt{2\kappa}, \sqrt{2\kappa}, \sqrt{2\kappa}\right\} \tag{2.47}$$

$$\mathbb{T}^{\mathrm{loss}} = \mathrm{Diag}\left\{\sqrt{2\gamma}e^{-\phi}, \sqrt{2\gamma}e^{\phi}, \sqrt{2\gamma}, \sqrt{2\gamma}, \sqrt{2\gamma}, \sqrt{2\gamma}\right\}, \tag{2.48}$$

where the phase $\phi_p$ is accumulated from the input field phase ($\theta_{\text{in}}$), that is $\phi_p = \theta_{\text{in}} - \theta_p$. Vectors $\delta\hat{\mathbf{x}}^{\text{in}}$ and $\delta\hat{\mathbf{x}}^{\text{loss}}$ have the same form as equation (2.45) respecting the same commuting relations as in (2.39). The elements of matrix $\mathbb{M}$ are functions of the mean field values and the detunings.

Equation (2.46) can give us correlations for all the three fields involved in the parametric oscillation. However, at this point of the project we are interested in the two-mode correlations between signal and idler. We then treat the pump field as a classical beam ($\delta\hat{a}_p \to 0$) and simplify to four equations the set described by (2.46). Furthermore, the observables that we are interested are the amplitude ($\hat{p}_j$) and phase ($\hat{q}_j$) operators, which respect the canonical commutation relation of equation (1.2). As a function of $\hat{a}_j$ and $\hat{a}_j^\dagger$, they are given by

$$\hat{p}_j = \frac{\hat{a}_j + \hat{a}_j^\dagger}{\sqrt{2}}, \tag{2.49}$$

$$\hat{q}_j = -i\frac{\hat{a}_j - \hat{a}_j^\dagger}{\sqrt{2}}, \quad j = \{s, i\}, \tag{2.50}$$

The dynamical equations (2.46) decouple in the sum and subtraction basis, equations (1.14) and (1.15), where the fluctuation vector

$$\delta\hat{\mathbf{x}}_\pm = \left[\delta\hat{p}_+, \delta\hat{q}_+, \delta\hat{p}_-, \delta\hat{q}_-\right]^{\text{T}} \tag{2.51}$$

will evolve following the dynamical equation

$$\frac{\text{d}}{\text{d}\tau}\delta\hat{\mathbf{x}}_\pm = -\mathbb{M}_\pm \cdot \delta\hat{\mathbf{x}}_\pm + \frac{\mathbb{T}_\pm^{\text{in}}}{\Gamma} \cdot \delta\hat{\mathbf{x}}_\pm^{\text{in}} + \frac{\mathbb{T}_\pm^{\text{loss}}}{\Gamma} \cdot \delta\hat{\mathbf{x}}_\pm^{\text{loss}}. \tag{2.52}$$

The coupling and loss matrices are given by $(\mathbb{T}_\pm^{\text{in}}, \mathbb{T}_\pm^{\text{loss}})$ and vectors $(\hat{\mathbf{x}}_\pm^{\text{in}}, \hat{\mathbf{x}}_\pm^{\text{loss}})$ follow directly from the basis changes of equations (2.49) and (2.50). Matrix $\mathbb{M}_\pm$ is explicitly given by [107]

$$\mathbb{M}_\pm = \begin{bmatrix} -6|\alpha|^2 & -2 & 0 & 0 \\ 0 & 6|\alpha|^2 + 4|\alpha|_p^2 - 2\Delta & 0 & 0 \\ 0 & 0 & 0 & -2 \\ 0 & 0 & 0 & -4|\alpha| - 4|\alpha|_p + 2\Delta \end{bmatrix}. \tag{2.53}$$

From the $\mathbb{M}_\pm$ matrix we can see that the subspaces are decoupled. One should note that the $\pm$ subscript is solely labeling a basis and not two different equation sets.

The parametric nature of FWM, conserving energy and momentum, leads to the production of highly correlated signal and idler modes. In order to characterize such correlations, we analyze the spectral noise density [108]

$$S_j(\Omega)\delta(\Omega + \Omega') = \langle \hat{x}(\Omega)\hat{x}(\Omega') \rangle \,, \tag{2.54}$$

where $\hat{x}(\Omega)$ is an arbitrary quadrature and $\Omega$ is the sideband frequency in which the measurement is carried out. From the dynamics described above, entanglement between signal and idler is predicted [21]. Such result is an extension of the two-mode amplitude squeezing ($S_{p_-}(\Omega)$) in the difference subspace, and is in accordance with previous analytical models [107]. In terms of experimentally accessible parameters, the noise compression is given by [97, 109, 110]

$$S_{p_-}(\Omega) = 1 - \frac{\eta_d\,(1 - Q_L/Q_I)}{1 + \Omega^2\tau_c^2}, \tag{2.55}$$

where $\eta_d$ is the detection efficiency and $\tau_c$ is the intracavity photon lifetime. The loaded ($Q_L$) and intrinsic ($Q_I$) quality factors were discussed in section 2.1 and are respectively given by equations (2.12) and (2.13).

Phase modulations are responsible for distortions on the noise ellipse [21, 101], which is the Fresnel diagram representation of the uncertainty associated with quadrature observables. Stronger correlations are expected in rotated quadratures:

$$\begin{bmatrix} \delta\hat{q}_\pm^\theta \\ \delta\hat{p}_\pm^\theta \end{bmatrix} = \begin{bmatrix} \cos\theta_\pm & \sin\theta_\pm \\ -\sin\theta_\pm & \cos\theta_\pm \end{bmatrix} \begin{bmatrix} \delta\hat{q}_\pm \\ \delta\hat{p}_\pm, \end{bmatrix} \tag{2.56}$$

where the angles $\theta_\pm$ diagonalize the spectral density matrix. A representation of this effect is given in figure 2.9.

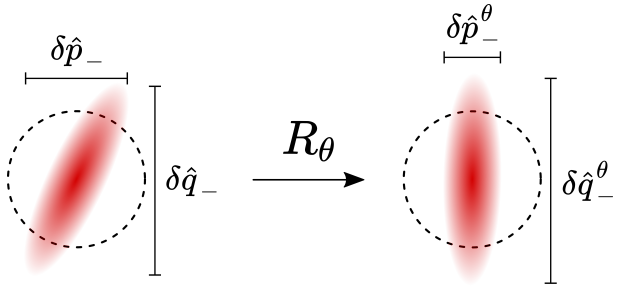


Figure 2.9: Noise ellipse (faded red) compared to the standard quantum limit (dashed circle). The best achieved squeezing in amplitude difference is not aligned with the quadrature. Instead, optimal squeezing is seen in the rotated frame. $R_\theta$ is the rotation operation by an angle $\theta$, equivalent to the squared matrix in equation (2.56).

• •

In this chapter we presented the silicon nitride on silicon oxide micro-ring resonators. We explored the coupling of light in and out the cavity along with its losses mechanisms, experimentally accessible through the quality factor. Although only a brief description of the micro-ring resonator is needed for our purpose, a plethora of on-chip passive applications can be performed. For instance, such devices are a reliable source of entangled pho-

tons [70, 111, 112]. They also can accommodate several linear optics components that can be used in the implementation of on-chip quantum information protocols [75, 77, 113, 114].

As seen in section 2.2, integrated optical parametric oscillators can be explored for the generation of bright sideband frequencies. The large third order non-linear coefficient of silicon nitride, together with the high confinement of light in the microcavity enables parametric oscillation with sub-milliwatt threshold [24]. The dependence of the parametric gain with the geometry of the waveguides enables the tailoring of the excited frequencies [83, 94, 95]. Further exploration in dispersion engineering can be done by studding other orders of $\beta$ in the expansion (2.33) and by coupling other spatial modes into the resonators [111, 115].

In particular, we are interested on the deterministic generation of nonclassical light. In this context, on-chip optical squeezing was successfully measured for bright beams [110, 116] as well as broadband squeezed vacuum [117]. Quantum aspects of microcombs [94, 95] were recently explored in the deterministic regime and two-mode squeezing was observed in a range of 40 modes [118]. Single-mode squeezed states were generated with dual pump technique, where photons of two different colors excite a near degenerate mode with wavelength equivalent to the mean of the pumps wavelength [119, 120]. Broadband quadrature squeezing via SPM was reported in [121].

As we can see from the different results exposed above, photonic devices present themselves as a versatile platform for future quantum technologies. However, there are still open questions regarding several properties of integrated optical systems, such as the influence of the generation of adjacent sidebands in the signal and idler correlations, the presence of nonclassical correlations between asymmetrical sidebands and the limits in the observation of expected nonclassical properties, such as entanglement, imposed by experimental conditions. We will explore aspects of this last questioning through careful experimentation. In the next chapter we will present the methods and techniques employed to study the modes excited in on-chip OPOs operating above oscillation threshold.

# Chapter 3

# Experimental Setup

Our experimental system is specifically designed to produce and characterize fields in on-chip optical parametric oscillators. A concise schematic of the setup is presented in figure 3.1, in which a 1560 nm diode laser is amplified (EDFA - erbium-doped fiber amplifier) and passes through a filter cavity. At this point, the high noise state at the erbium output is reduced to a low noise level. Comparisons between these situations will be given in section 4.1. The filtered pump is then coupled to the bus waveguide of the micro-ring cavity with a tapered fiber. The inverse tapered shape of the bus waveguide extremity allows highly efficient coupling [122], 75% for our system. The output of the integrated OPO is collected by a lens into free space and partially monitored on an optical spectrum analyzer. We separate the generated sidebands with a diffraction grating and send them to analysis cavities for resonator assisted detection [25, 26, 123].

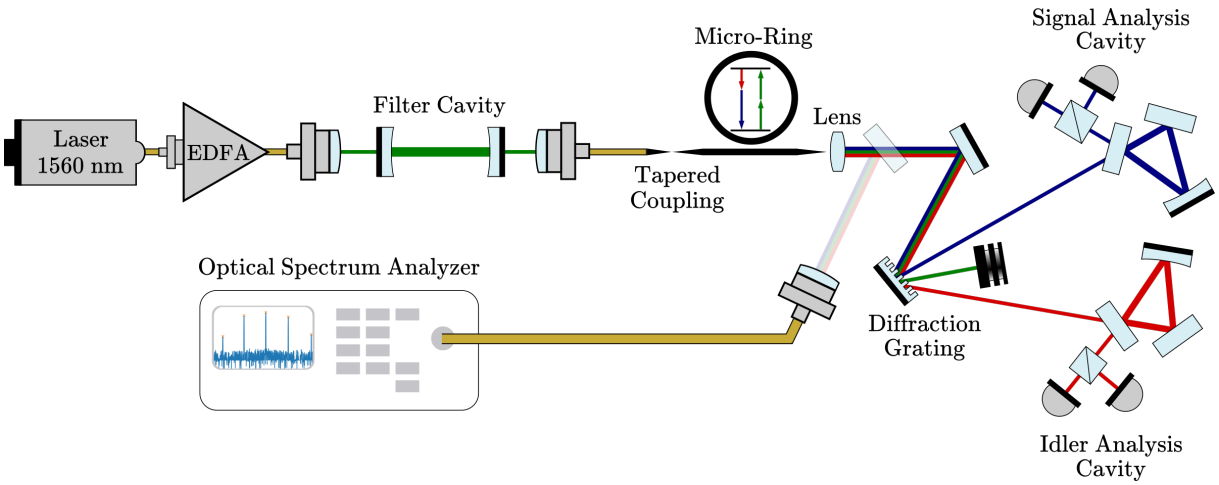


Figure 3.1: Schematic of the experimental setup. A 1560.6 nm laser source is filtered after amplification in order to generate a near coherent optical pump. The pump is coupled into the bus waveguide with a tapered fiber. Above threshold, intense signal and idler modes are excited. We collimate the cavity output into free space and monitor a small part of the fields with an optical spectrum analyzer. The fields are separated with a diffraction grating and sent to individual analysis cavities for resonator assisted detection.

In the present section we will explore all the relevant details of the system. As seen from figure 3.1, there are three main parts in our experimental setup: the pump preparation, the integrated OPO and the detection system. Details of the optical pump will be given in section 3.1. In section 3.2 we will present the characterization of our microcavities and details of signal and idler generation and stabilization. At last, in section 3.3, the resonator assisted detection scheme will be presented.

## 3.1 Optical Pump Preparation

Our optical source is a commercial RIO ORION$^{TM}$ diode laser with emission wavelength of 1560.6 nm, which is located in the short infrared spectrum and is compatible with telecommunication frequencies. The laser delivers approximately 20 mW of power and has low amplitude noise. However, due to an excessive phase noise of more than 20 dBm above shot noise for the relevant powers, we need to introduce a filter cavity in the system in order to improve the coherence of the state, trying to bring it closer to the noise level of an effective coherent state. The introduction of several optical components in the optical path, needed for both alignments and protection of the laser, drastically reduces the accessible optical power to pump our microcavity. This is compensated with the introduction of the EDFA, model Keopsys CEFA-C-PB-HP-SM-33-NL1-OM1-B130-FA-FA, with controllable output power from 200 mW to 2.00 W. The amplifier further increases the fluctuations of the field, also mitigated by the filter cavity.

The filter cavity was built by Pablo Jaime Palacios Avila during his master's program [124] in a bow-tie geometry with two high reflective curved mirrors and two partially transparent ($T \sim 0.5\%$) input and output mirrors. The total optical path of the cavity is approximately 4.9 m, which gives us an inferred free spectral range of $\Delta_{\mathrm{FSR}} = 61.2$ MHz. Following this scale, we measured a bandwidth of $\delta\omega = 237.1$ kHz and obtained a finesse of $\mathcal{F} = 258.1$.

We lock the cavity in resonance using the Hänsch-Couillaud method [125], in which we take advantage of the birefringence of the input mirror to monitor undesired instabilities through the interference between the transmitted and reflected polarizations. We generate an error signal ($\epsilon(t)$), see figure 3.2, with the electronic subtraction of signals coming from a balanced detection scheme. This system alone presents strong fluctuations corresponding to up to 20% of intensity variations, probably due to frequency instabilities of the light source. We employed a combination of current modulations in the laser and the introduction of an acousto-optic modulator (AOM) after the filter cavity, which will

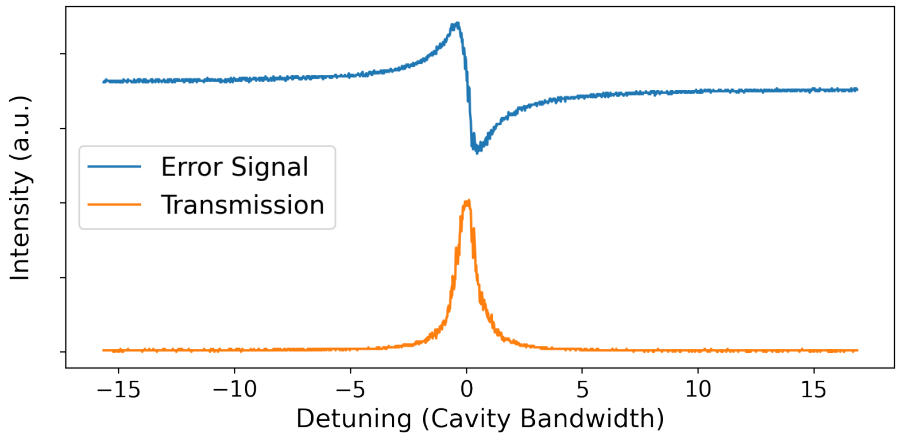


Figure 3.2: Error signal generated by the Hänsch-Couillaud method used to lock the cavity in resonance. The transmission of the cavity indicates the sweeping around the resonant peak. The magnitudes of the error signal and the cavity monitor are not related and an offset was included to facilitate the visualization.

be described next. The full optical pump preparation setup is schematized in figure 3.3.

First attempts consisted in thorough tuning of the PI system (proportional and integration electronic signals used to lock the cavity) fed to the cavity PZT combined with the broadening of the cavity bandwidth. We introduced a quarter waveplate solely to enhance the intracavity losses leading to the new respective bandwidth and finesse values of $\Delta_{\mathrm{BW}} = 278.5$ kHz and $\mathcal{F} = 220.0$. This strategies were partially fruitful as the fluctuations were dropped to half their initial values. However, the pump intensity was still too noisy for the following parts of the system, as they would lead to instabilities on the OPO oscillation condition. This strategy was limited in effectiveness due to the 24 kHz cutoff frequency of the PZT. The remaining fluctuations reached up to hundreds of kHz, impossible to be compensated by the piezoelectric device.

The fast fluctuations were mitigated with a modulation in the laser. We used the Hänsch-Couillaud error signal of the locked system together with an electronic gain and a phase control to feedback the current modulation input of the RIO laser and compensate for the oscillations. This effectively reduced the majority of the oscillations, with only eventual instability spikes remaining. Since they were still disturbing the stabilization of the OPO a further technique was employed. We monitor a fraction of the output field of the filter cavity by setting an acousto-optic modulator (AOM) fed with this signal, again with gain and phase control, in a feedforward scheme. Finally, we ended up with a near coherent pump with small intensity fluctuations corresponding to up to 1% of the total power. A very convenient feature of the chosen setup is the possibility of tuning the gain and phase parameters in real time. Figure 3.4 shows the effect of each subsequent

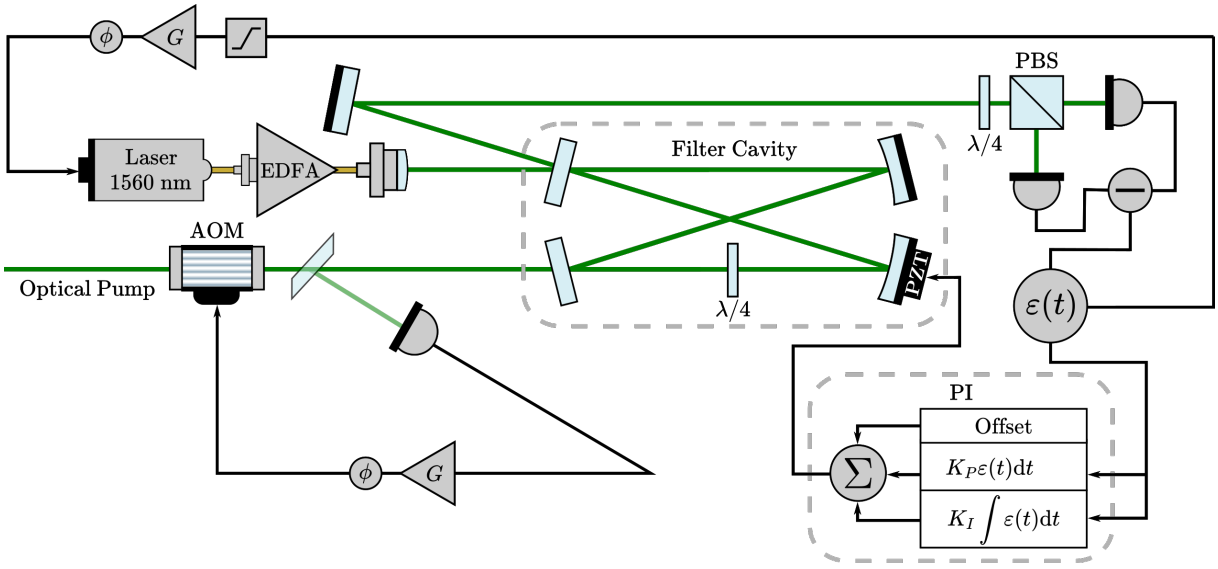


Figure 3.3: Near coherent optical pump generation scheme. A 1560 nm diode laser source is amplified by an EDFA and sent to a bow-tie configuration filter cavity. A quarter wave-plate was introduced inside the cavity in order to increasse the optical losses. The cavity is locked to the laser frequency with the Hänsch-Couillaud method using a PI system with the constants $K_P$ and $K_I$ respective to the proportional and the integrator actuators. Current modulations are fed back to the laser in order to mitigate undesired fluctuations. Further cleaning in the cavity output is done with an acousto-optic modulator (AOM). The gain $G$ and phase control $\phi$ necessary for the optimization of the feedback and feed-forward systems are represented along the electrical paths.

stabilization step in the output intensity.

From this procedure we were able to produce a near coherent field, drastically reducing the quadrature noise. Details of the pump noise in different operation conditions of the system will be given in section 4.1, where we use the resonator assisted detection scheme to fully characterize its fluctuations.

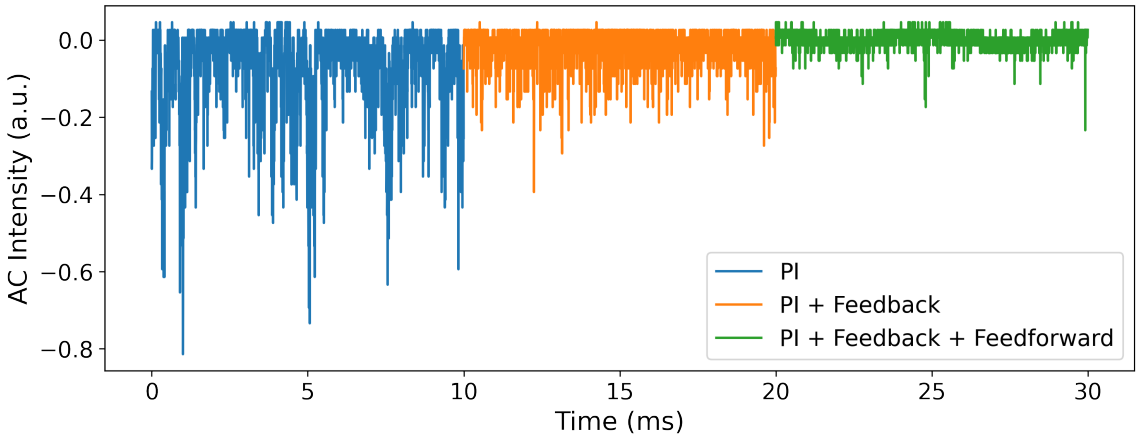


Figure 3.4: Evolution of the output pump fluctuations with the actuation of the different stabilization systems. At first, the PZT alone, feeded by the PI system, is unable to mitigate the strong fluctuations. Then, a good improvement is seen from the addition of modulations into the laser current. With the aid of an acousto-optic modulator we end up with a cleaner signal. Note that the action of the AOM induces fluctuation above the mean field. The curves were obtained from the AC coupling of a photocurrent in an oscilloscope.

## 3.2 Integrated Micro-Ring Cavity

At the core of our experiment are the micro-ring resonators, as they are the source of nonclassical light that we are interested in. As described in section 2.1 they are constituted of a bus waveguide close to a circular loop. The coupling of the optical field into the bus waveguide is done with the aid of a tapered fiber. The extremities of the bus waveguide have a similar conical shape (see figure 3.5) which enables high efficient coupling between them [126]. We fixate the tapered fiber in a manual micrometric control with three axis (Newport MAX355D) with which we align the pump field into the bus waveguide. As the tip of the fiber remains suspended at the end of alignment system, it is susceptible to jiggling due to air mass displacements. We disposed acrylic barriers around the system to reduce such effects. Further degrees of freedom in the alignment are present in the chip positioning. It remains freely supported above a copper base with angular and displacement controls, which allows us to compensate eventual displacements of the chip.

The tuning of the microcavity into resonance is done via thermo-optical effect controled by a platinum micro-heater above the micro-ring, as schematized in figure 3.5. The variation in the refractive index due to this thermal control [127] changes the length of the optical path inside the microresonator, which is equivalent to the tuning of optical cavities by mechanical means. The localized thermal effect has a fast response allowing sub-millisecond operation [128, 129]. Platinum is chosen as the heater material due to its tolerance to high temperatures. In our systems, resistances of the order of hundreds of ohms are observed. This allows us to reach detunings of around 200 GHz applying voltages below the damage threshold of the heater. Electrical probes are used to supply the electrical current. When positioned they help holding the chip still, preventing it from accidental slips during the experiment operation.

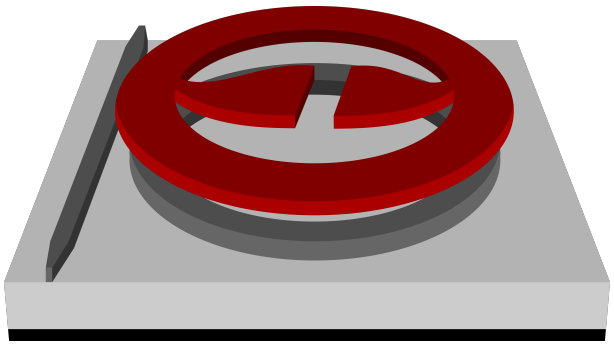

Figure 3.5: Micro-ring resonator scheme highlighting the integrated micro-heater (red) above the cavity. The conical shapes of the bus waveguide are also represented in the figure.

Additional temperature stabilization is done with a peltier under the copper basis. The temperature control is actively locked near room temperature with a PI system with a 10 mK precision range. This minimizes thermal drifts and aids in the resonance stabilization.

Due to the pump frequency used in our system and the small size of our OPO, we use an infrared camera, model FLIR A6260sc, coupled to a microscope to aid in the system alignment and monitoring. This allows us to visualize scattered light in the microcavity. The output light of the chip is collimated into free space by a low loss ($< 1$ dBm) aspheric lens (Thorlabs C430TME-C) with a large numerical aperture (0.15). The lens is also fixed in manual micrometric control with three axis, identical to the one used for the tapered fiber. Aligning this lens is crucial, because the subsequent parts of the system, including the analysis cavities, are sensitive to any changes in the optical path or collimation.

In figure 3.6 (a) we present a photograph of the coupling apparatus, in which we can identify the several components described above. Pictures of a microcavity without any coupled light and in a resonant condition were taken with the aid of the infrared camera and are shown in the respective images 3.6 (b) and (c). Note that the shape of our micro-resonators are not circular rings, but a structure with two radii that go adiabatically towards each other. In practice, this shape have effects in the system coupling, losses and dispersion.

The output field of this system was used in different experimental tasks. First, we characterized the microcavities by measuring their quality factors, which will be explored in the next subsection. Then, in section 3.2.2, we will describe the locking system used to stabilize the generation of signal and idler fields.

### 3.2.1 Microcavities Characterization

The quantum correlations expected from the micro-ring cavities are closely related to the intrinsic and loaded quality factors of the system, as seen in equation (2.55). The higher the ratio between those two factors, the higher the magnitude of amplitude squeezing will be. In order to avoid undesired optical losses, detrimental to quantum correlations, it is also desirable to reduce the interaction time between the generated signal and idler fields and the resonator. Hence, highly overcoupled systems, see section 2.1, are ideal to our purposes.

Currently, we have access to several chips built for the study of correlations, but we will focus on the one used for the final results exposed in this work. The chips are printed with several equal resonators with different gaps between them and the bus waveguides, as illustrated in figure 3.7. In this way, we can explore different coupling regimes in order

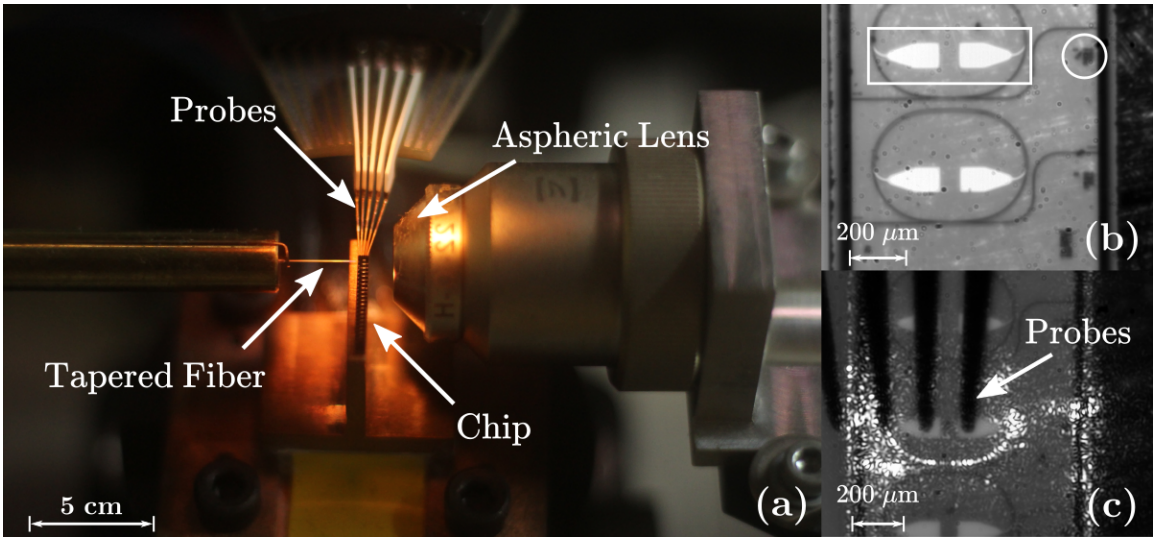


Figure 3.6: **(a)** Photograph of the chip setup, where we highlighted the tapered fiber, the heater probes and the aspheric lens. Looking closely to the chip one can see the printed waveguides as the heaters scatter the top light. **(b)** Microscopic photograph of two microcavities. In the picture we notice the real shape of the micro-rings that is not exactly circular and the bus waveguides passing close to them. As the gaps sizes are of only hundreds of nanometers we cannot distinguish the separation between the waveguides in the coupling region. The square shape highlights the probes contacts and the microcavity details are printed inside the circle. **(c)** Micro-ring tuned into resonant condition. With the aid of the infrared camera we can clearly see the scattered light off the resonator. Scatterings at the input and output of the bus waveguide help us to couple the pump into the chip.

to characterize and select the microcavity that better suits our purposes.

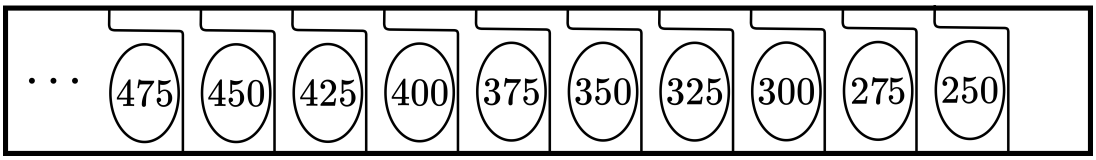


Figure 3.7: Schematic that partially represents the chip we will work with. The 10 identical microresonators have different gaps between them and their respective bus waveguide. The inset numbers accounts for the respective gap in nanometer units, which are printed in the real microcavities for identification. The full chip has a total of 20 microcavities with gaps ranging from 250 nm to 725 nm.

Due to the small dimensions of the optical path in the microcavities, FSRs of dozens, or even hundreds of GHz are routinely obtained. In our case, we worked with 80 GHz cavities, with two different radii that adiabatically goes towards each other with a hyperbolic tangent function. This corresponds to a microcavity with approximate 1.88 mm of length. In principle, a full cavity FSR could be scanned with the heater tuning. However, the nonlinear behavior of the thermal effect for large detunings [128] forbids us to use the FSR as a frequency scale to measure the bandwidth of the resonators, which is the standard

method used for the macroscopic optical cavities in our system. Hence, we need a different measurement method to obtain a reference scale.

Fortunately, the pump laser frequency can be tuned by internal thermoelectric cooling, which is accessible by using the manufacturer available software. We can vary the emission wavelength by 65 pm at a cost of optical power and an increase in the quadrature noise. Using a Bristol 671 wavelength monitor we observed the behavior of the tuning, shown in figure 3.8.

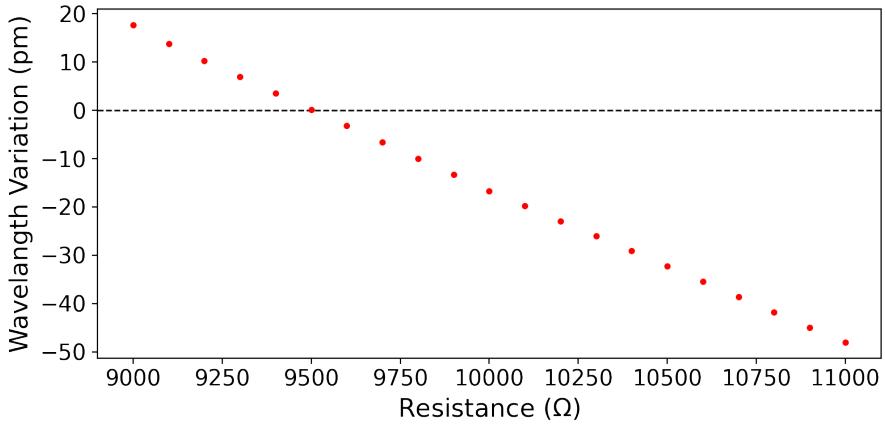


Figure 3.8: RIO laser wavelength calibration as a function of the accessible internal resistance parameter. The dashed line indicates the optimal operation frequency of 1560.6 nm set as default by the manufacturer.

Using the wavelength variation, we can monitor displacements of the resonance peak and use it as a frequency scale. This gives us access to a direct measurement of the micro-ring bandwidth and hence the quality factor by equation (2.11). In order to avoid distortions of the resonant peak due to thermal effects, we pumped the microcavities with low power. In this regime, we see an approximate Lorentzian shape as we sweep the heater around a resonant condition. We determine the bandwith by computationally fitting the Lorentzian curve to the data.

Additionally, we measured the extinction ratio of every cavity, given by

$$T_{\text{ext}} = 1 - \frac{T_{\text{min}}}{T_{\text{max}}}, \tag{3.1}$$

where $T_{\text{min}}$ is the transmission dip exactly when in resonance and $T_{\text{max}}$ the direct bus waveguide transmission without any coupling to the resonator. The coupling regime changes with the gaps, as the coupling strength varies. The variation of the extinction ratio with the gaps is due to interferometric effects between the output light of the micro-cavity and field in the bus waveguide, as discussed in section 2.1. We identify the critical

coupling region as the extinction ratio gets closer to unity. From the respective quality factor we can then infer the intrinsic quality factor of the systems through equation (2.13).

Figures 3.9 (a) and (b) show the respective quality factors (a) and extinction ratios (b) for the quasi-transverse $TE_{00}$ and $TM_{00}$ modes of the ring. We estimate intrinsic

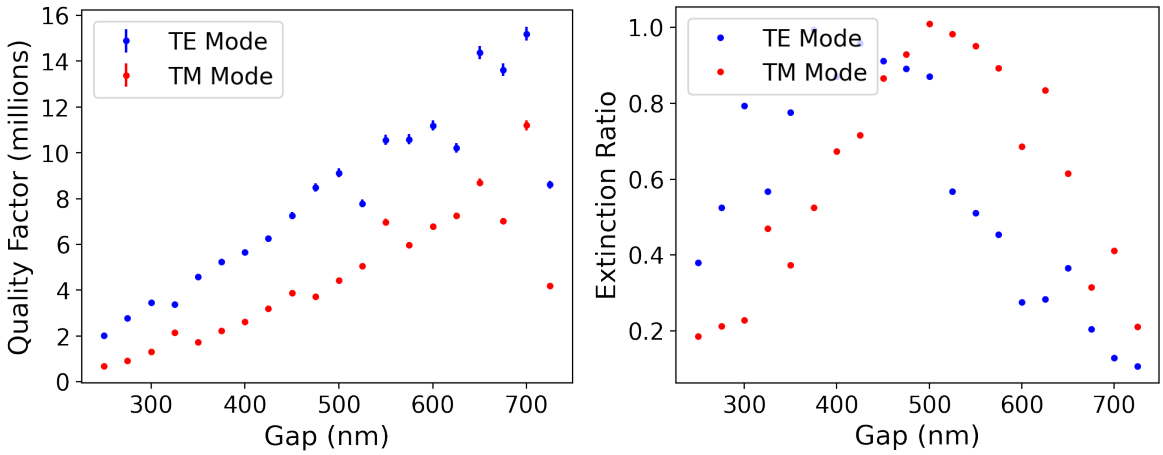


(a) (b)

Figure 3.9: Quality factor (a) and extinction ratio (b) for all the microcavities present in the chip for both quasi-transverse fundamental modes.

quality factors of $Q_I^{\mathrm{TE}} \sim 16$ million and $Q_I^{\mathrm{TM}} \sim 12$ million. In order to preserve the correlations of the generated fields, we chose to work with the cavity with higher coupling, corresponding to the one with the smaller gap of 250 nm. We worked with the TE mode as it has a lower oscillation threshold, avoiding the need of extra amplification. Furthermore, it presents a high loaded ($Q_L^{\mathrm{TE}} \sim 2$ million) to intrinsic quality factor ratio, which contributes to the two-mode amplitude correlations as shown in equation (2.55). The characterization of microcavity chosen from now quality factors, losses and expected squeezing are summarized in table 3.1. It is worth to note that the finesse of the optical cavity is of same order of magnitude of typical mirror-based OPOs [14, 19, 130].

### 3.2.2 Stable Optical Parametric Oscillations

One of the major difficulties encountered during the project was the stability in the generation of signal and idler fields. Working above the threshold, the system is stable enough to passively maintain the resonant condition for several minutes. Since we are working with very high quality factor microresonators additional sideband modes are easily exited in this pumping regime. Moreover, small variations on the pump intensity entails changes in the oscillation frequencies, where there is a tendency of signal and idler to hop between different modes. Although the hops are small, the alignment and mode

Table 3.1: Parameters of the microcavity used in the generation of signal and idler.

| Parameter | Magnitude |
|---|---|
| Gap | 250 nm |
| Free Spectral Range | 80 GHz |
| Loaded Quality Factor | $2 \times 10^9$ |
| Intrinsic Quality Factor | $16 \times 10^9$ |
| Intrinsic Losses | 0.006 |
| Coupling Losses | 0.041 |
| Finesse | 132 |
| Expected Squeezing | −9.00 dB |

matching of optical cavities are harshly harmed with the consequent change of the optical paths. This experimental instabilities are mitigated by using an active locking system by modulating the micro-heaters. Stable oscillations with the frequencies shown in figure 3.10 were then achieved. This also contributed to the assemble of the analysis cavities, as the system remained stable even when subjected to mechanical disturbances during the positioning and alignment of several optical components.

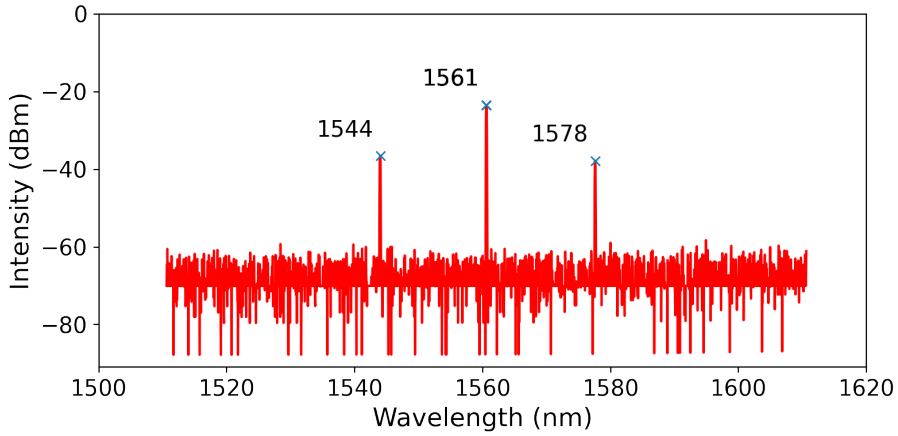


Figure 3.10: Optical spectrum of the stabilized oscillations achieved with the active locking system. The data were acquired with a Yokogawa AQ6370D spectrum analyzer.

When driving a Kerr system with high optical power, thermal effects and phase modulations will distort the symmetric Lorentzian shape of the resonant peak, as discussed in section 2.2.2. This effect can be seen in figure 3.11 (a). The bistable character of the peak [106] hinders the generation of an error signal at maximum resonance. However, when operating above threshold and by separating the generated fields from the pump, we can observe the drop of intensity on the optical pump with the detuning of the resonator. Monitoring the pump field after the separation of the fields by the optical grating we observe a nearly symmetric shape of the depletion of the field, see figure 3.11 (b), where

the stability point can be explored to lock the cavity in resonance.

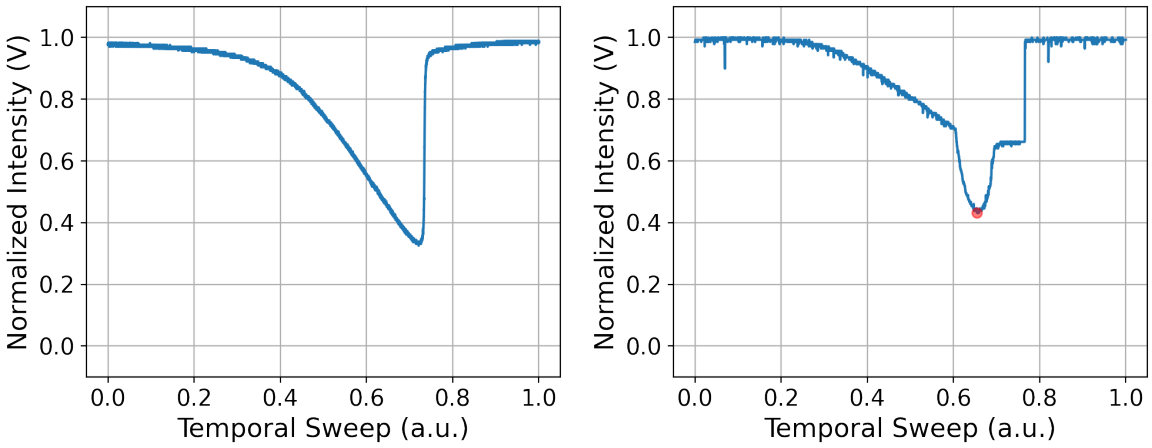


(a) (b)

Figure 3.11: Bistability effect in the OPO transmission above oscillation threshold. In figure (a) all the output fields are overlapped, while in figure (b) the pump is being monitored after separation of the fields. The depletion in the signal is equivalent to the energy distributed to the other modes and the red dot indicates the stabilization point.

We used a Stanford Research System SR830 DSP lock-in amplifier to modulate the micro-heater current with a frequency of 15 kHz and stabilize the system through a dither and lock scheme. Optimum parameters of the proportional and integrator signals are subject to daily changes in the experimental conditions. For instance, the angular alignment between the chip and the taper fiber alters the shape of the dip and the small step at the side of it. To further avoid thermal drifts, the chip stays in a copper basis with controlled temperature. This is done with a peltier and a PI system. We keep the chip close to room temperature with a precision in the range of 10 mK. The stabilization system is shown in figure 3.12.

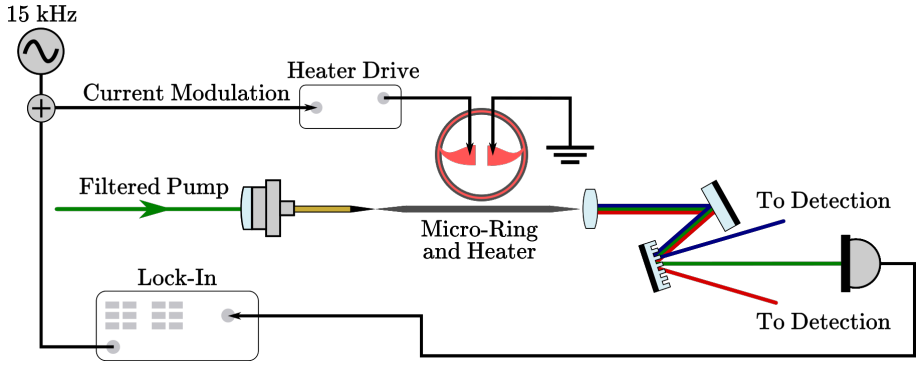


Figure 3.12: OPO stability system. We modulate the micro-heater at 15 kHz. The separated pump photocurrent is sent to a lock-in system, added to the 15 kHz modulation, to keep the resonant condition stable.

As a result, we managed to stabilize the oscillations for several minutes, even for pump powers very close to oscillation threshold ($P_{th} =\sim 13$ mW). Resonant condition is maintained even with a certain degree of mechanical perturbations in the environment or in the optical table. This was crucial for the assembling of the resonator assisted detection schemes, as thorough alignment of the optical systems is needed.

## 3.3 Quadrature Measurements

The experimentally accessible observable that we retrieve from photodetection is a time-dependent current, namely photocurrent, proportional to the intensity of the field. It is related to the positive and negative frequency parts of the electric field as $\hat{I} = \hat{E}^{-}(t)\hat{E}^{+}(t)$ [131]. The electric field is related to the creation and annihilation operators by

$$\hat{E}^{+}(t) \propto \hat{a}(t) = \int e^{-i\omega t}\hat{a}_{\omega}\mathrm{d}\omega; \quad \hat{E}^{-}(t) \propto \hat{a}^{\dagger}(t) = \int e^{i\omega t}\hat{a}^{\dagger}_{\omega}\mathrm{d}\omega. \tag{3.2}$$

Apart from a dimensionality constant, we define the intensity operator as a function of the linearized operators of equation (2.40) as

$$\hat{I}(t) \equiv \hat{a}^{\dagger}(t)\hat{a}(t) = |\alpha(t)|^2 + |\alpha(t)|\left[e^{-i\varphi}\delta\hat{a}(t) + e^{i\varphi}\delta\hat{a}^{\dagger}(t)\right], \tag{3.3}$$

where we dropped the second order terms of the fluctuations. The phase $\varphi$ is related to the mean field as $\alpha = |\alpha|e^{i\varphi}$. As we can see, the intensity operator has a mean value added to fluctuations that are related to the quadrature operators of equations (2.49) and (2.50). As the photodetector is only sensitive to amplitude fluctuations, we recognize the amplitude quadrature as $\hat{p}(t) = \left[e^{-i\varphi}\delta\hat{a}(t) + e^{i\varphi}\delta\hat{a}^{\dagger}(t)\right]$, which is in the same phase space direction of the carrier. Without loss of generality we can take this phase as $\phi = 0$ for the amplitude quadrature. Moreover, note that the quadrature fluctuations are amplified by the carrier mean field. In practice, this amplification is what allows us to experimentally access the quadrature noise that would be otherwise buried under the electronic noise of the detection systems.

The quantum quadratures that describe the continuous variables of an optical state are then related to the fluctuations inherent to optical fields. As fluctuations act as modulations of a mean field, they can be seen as energy distributions to other modes of the field, analogously to the modulation of classical fields [3]. Physically, they are translated as a *small* probability of creating photons in sideband modes. For bright fields, the mean field intensity is proportional to a high photon flux, typically of the order of $10^{16}$, while the sideband photon flux is of the order of units [4]. For modes spectrally

distant from the carrier the fluctuations approach their minimum value, which is known as the shot noise limit of the field.

The observation of quantum fluctuations in the optical carrier is hindered by technical difficulties. On the other hand, signatures of nonclassical correlations can be seen in frequencies in a sideband region. In our case, limited by the bandwidth of our OPO. Further limitations are imposed by the detection system, where we can only relay in measurements in frequencies within its bandwidth. For resonator assisted detection, this value is proportional to the analysis cavity bandwidth . Figure 3.13 illustrate the intensity spectrum of an optical field, its sidebands and the described detection region, limited by the analysis cavity ($\Delta_{\mathrm{BW}}^{\mathrm{AC}}$) and the OPO ($\Delta_{\mathrm{BW}}^{\mathrm{OPO}}$) bandwidths.

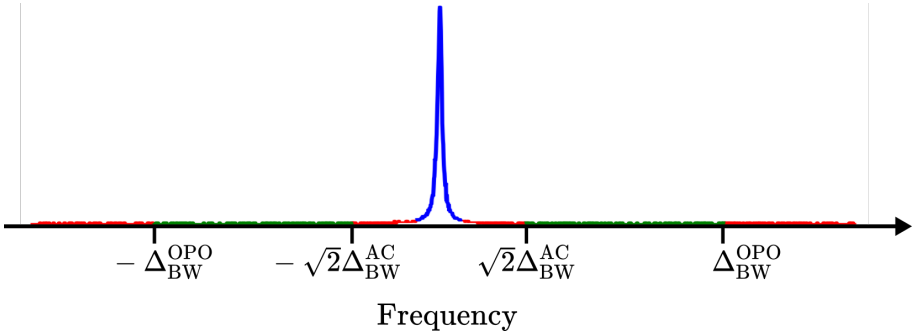


Figure 3.13: Intensity spectrum of an optical field. The sidebands are highlighted in red and green and photon overpopulation area in blue. The detection region, in green, has indications of the limits imposed by the OPO and the analysis cavity.

In the frequency domain, the intensity fluctuations are described by the Fourier transform

$$\delta\hat{I}_{\Omega} = \int \delta\hat{I}(t)e^{i\Omega t}\mathrm{d}t = e^{-i\varphi}\int e^{i\Omega t}\delta\hat{a}(t)\mathrm{d}t + e^{i\varphi}\int e^{i\Omega t}\delta\hat{a}^{\dagger}(t)\mathrm{d}t, \tag{3.4}$$

where the integration limits are determined by the detection bandwidth. As the temporal creation and annihilation operators are related to quantum fluctuations, they encompass all the spectrum with exception of the carrier frequency $\omega_0$. Explicitly they are given by (see equations (3.2) and (3.3)) [25, 26]

$$\delta\hat{a}(t) = \int_0^{'\infty} e^{-i(\omega-\omega_0)t}\delta\hat{a}_{\omega}\mathrm{d}\omega; \quad \delta\hat{a}^{\dagger}(t) = \int_{-\infty}^{'0} e^{-i(\omega-\omega_0)t}\delta\hat{a}_{\omega}^{\dagger}\mathrm{d}\omega, \tag{3.5}$$

where the prime notation in the integral limit excludes $\omega_0$. Inserting these equations in (3.4), we determine the non-Hermitian operator

$$\hat{I}_{\Omega} = e^{-i\varphi}\hat{a}_{\Omega} + e^{i\varphi}\hat{a}_{-\Omega}^{\dagger}, \tag{3.6}$$

where the $\pm\Omega$ indexes indicate the sideband frequency around $\omega_0$ and $\hat{a}_{\Omega}^{\dagger} = \hat{a}_{-\Omega}$. We dropped the indication of the fluctuations by $\delta$ for the sake of a cleaner notation. This equation stresses the two-mode character of the photodetection spectral analysis.

The sidebands are accessed in the laboratory through the measurement of (Hermitian) observable operators. We introduce the two observable operators

$$\hat{I}_{\cos} = \cos\varphi\hat{p}_{\mathfrak{s}} + \sin\varphi\hat{q}_{\mathfrak{s}}, \tag{3.7}$$

$$\hat{I}_{\sin} = \cos\varphi\hat{q}_{\mathfrak{a}} - \sin\varphi\hat{p}_{\mathfrak{a}}, \tag{3.8}$$

where the $\varphi$ phase is now the relative phase between an arbitrary quadrature and the amplitude one. In principle, this phase is null due to the insensibility of the photodetector to phase fluctuations. We will address the method of resonator assisted detection in section 3.3.2, where we will show how to vary $\varphi$ and measure the fluctuations of arbitrary quadratures.

We introduce the quadrature operators in the symmetric ($\mathfrak{s}$) and antisymmetric ($\mathfrak{a}$) basis as

$$\hat{p}_{\mathfrak{s},\mathfrak{a}} = \frac{\hat{p}_{\Omega} \pm \hat{p}_{-\Omega}}{\sqrt{2}}, \tag{3.9}$$

$$\hat{q}_{\mathfrak{s},\mathfrak{a}} = \frac{\hat{q}_{\Omega} \pm \hat{q}_{-\Omega}}{\sqrt{2}}. \tag{3.10}$$

We can now write the intensity operator in terms of the commuting observables $\hat{I}_{\cos}$ and $\hat{I}_{\sin}$ as

$$\hat{I}_{\Omega} = \hat{I}_{\cos} + i\hat{I}_{\sin}. \tag{3.11}$$

Hence, the simultaneous measurement of $\hat{I}_{\cos}$ and $\hat{I}_{\sin}$ allows us to reconstruct the intensity operator. This is possible through a double demodulation scheme, in which we divide the measured temporal photocurrent and mix each of the signals with in quadrature electronic references, as schematized in figure 3.14.

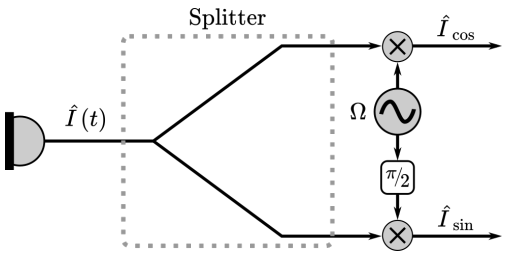


Figure 3.14: Mixture of the photocurrent with two electronic references of frequency $\Omega$ in quadradure.

The Wiener-Kintchine theorem states that the spectral density, equation (2.54), of a stationary variable is the Fourier transform of its temporal correlation [108]. Assuming a stationary photocurrent, its spectral density is given by $S(\Omega) = \left\langle \hat{I}_{\Omega}\hat{I}_{-\Omega} \right\rangle$ which is related with equations (3.7) and (3.8) by

$$S(\Omega) = \frac{1}{2}\left\langle \hat{I}^2_{\cos} \right\rangle + \frac{1}{2}\left\langle \hat{I}^2_{\sin} \right\rangle. \tag{3.12}$$

Since the mean field of the measured sidebands is zero, the expected values are equivalent to the *variance* of the demodulated photocurrents. Hence, we have an experimental approach to retrieve the information about the noise quadratures. From equations (3.7) and (3.8), in the absence of any methods to access arbitrary quadratures, we note that the spectral density gives us information about $\hat{p}_s$ and $\hat{q}_a$. Since we do not have any means to observe phase fluctuations in this scenario, we reach the conclusion that these quadratures carry the same information. Furthermore, we cannot attribute any physical meaning to the measured fluctuations unless we compare them to a reference noise.

From equation (2.54), we can also check the stationarity of a given photocurrent by

$$\left\langle \hat{I}_\Omega \hat{I}_\Omega \right\rangle = 0 \rightarrow \begin{cases} \left\langle \hat{I}^2_{\cos} \right\rangle - \left\langle \hat{I}^2_{\sin} \right\rangle = 0, \\ \left\langle \hat{I}_{\cos} \hat{I}_{\sin} \right\rangle = 0. \end{cases} \tag{3.13}$$

This is an important indicator of the reliability of the detection system which will be explored in our results.

We need to further develop the analysis to include more than one optical field. In this case, besides the validity of equations (3.12) and (3.13) for the individual signal (s) and idler (i) beams we reach the cross correlations of the spectral photocurrents by [25, 26]

$$\mathrm{Re}\left\{ \left\langle \hat{I}^{(s)}_\Omega \hat{I}^{(i)}_{-\Omega} \right\rangle \right\} = \frac{1}{2} \left\langle \hat{I}^{(s)}_{\cos} \hat{I}^{(i)}_{\cos} \right\rangle + \frac{1}{2} \left\langle \hat{I}^{(s)}_{\sin} \hat{I}^{(i)}_{\sin} \right\rangle, \tag{3.14}$$

$$\mathrm{Im}\left\{ \left\langle \hat{I}^{(s)}_\Omega \hat{I}^{(i)}_{-\Omega} \right\rangle \right\} = \frac{1}{2} \left\langle \hat{I}^{(s)}_{\sin} \hat{I}^{(i)}_{\cos} \right\rangle - \frac{1}{2} \left\langle \hat{I}^{(s)}_{\cos} \hat{I}^{(i)}_{\sin} \right\rangle. \tag{3.15}$$

Stationarity then implies

$$\left\langle \hat{I}^{(s)}_\Omega \hat{I}^{(i)}_\Omega \right\rangle = 0 \rightarrow \begin{cases} \left\langle \hat{I}^{(s)}_{\cos} \hat{I}^{(i)}_{\cos} \right\rangle &= \left\langle \hat{I}^{(s)}_{\sin} \hat{I}^{(i)}_{\sin} \right\rangle, \\ \left\langle \hat{I}^{(s)}_{\sin} \hat{I}^{(i)}_{\cos} \right\rangle &= - \left\langle \hat{I}^{(s)}_{\cos} \hat{I}^{(i)}_{\sin} \right\rangle. \end{cases} \tag{3.16}$$

The four-mode covariance matrix can then be organized as follows. Consider the symmetric ($\hat{\mathbf{x}}_\mathfrak{s}$) and antisymmetric ($\hat{\mathbf{x}}_\mathfrak{a}$) vectors containing the canonical operators in the symmetric and antisymmetric basis, equations (3.9) and (3.10), as

$$\hat{\mathbf{x}}_j = \left[ \hat{p}^{(s)}_j, \hat{q}^{(s)}_j, \hat{p}^{(i)}_j, \hat{q}^{(i)}_j \right]^{\mathrm{T}}, \quad j = \{\mathfrak{s}, \mathfrak{a}\}. \tag{3.17}$$

The covariance matrix will then assume the form [25, 26]

$$\mathbb{V} = \begin{bmatrix} \mathbb{V}_\mathfrak{s} & \mathbb{C}_{(\mathfrak{s},\mathfrak{a})} \\ \mathbb{C}^{\mathrm{T}}_{(\mathfrak{s},\mathfrak{a})} & \mathbb{V}_\mathfrak{a} \end{bmatrix}, \tag{3.18}$$

where the first block matrix in the main diagonal is related purely to the symmetric correlations and the second one to the antisymmetric correlations. The antidiagonal matrices

are related to cross correlations between the symmetric and antisymmetric operators. The symmetric matrix is explicitly given by

$$\mathbb{V}_{\mathfrak{s}} = \frac{1}{2}\left\langle \mathbf{x}_{\mathfrak{s}} \cdot \mathbf{x}_{\mathfrak{s}}^{\mathrm{T}} + \left(\mathbf{x}_{\mathfrak{s}} \cdot \mathbf{x}_{\mathfrak{s}}^{\mathrm{T}}\right)^{\mathrm{T}} \right\rangle = \begin{bmatrix} \Delta^2 \hat{p}_{\mathfrak{s}}^{(s)} & \left\langle \hat{p}_{\mathfrak{s}}^{(s)} \hat{q}_{\mathfrak{s}}^{(s)} \right\rangle & \left\langle \hat{p}_{\mathfrak{s}}^{(s)} \hat{p}_{\mathfrak{s}}^{(i)} \right\rangle & \left\langle \hat{p}_{\mathfrak{s}}^{(s)} \hat{q}_{\mathfrak{s}}^{(i)} \right\rangle \\ \left\langle \hat{q}_{\mathfrak{s}}^{(s)} \hat{p}_{\mathfrak{s}}^{(s)} \right\rangle & \Delta^2 \hat{q}_{\mathfrak{s}}^{(s)} & \left\langle \hat{q}_{\mathfrak{s}}^{(s)} \hat{p}_{\mathfrak{s}}^{(i)} \right\rangle & \left\langle \hat{q}_{\mathfrak{s}}^{(s)} \hat{q}_{\mathfrak{s}}^{(i)} \right\rangle \\ \left\langle \hat{p}_{\mathfrak{s}}^{(i)} \hat{p}_{\mathfrak{s}}^{(s)} \right\rangle & \left\langle \hat{p}_{\mathfrak{s}}^{(i)} \hat{q}_{\mathfrak{s}}^{(s)} \right\rangle & \Delta^2 \hat{p}_{\mathfrak{s}}^{(i)} & \left\langle \hat{p}_{\mathfrak{s}}^{(i)} \hat{q}_{\mathfrak{s}}^{(i)} \right\rangle \\ \left\langle \hat{q}_{\mathfrak{s}}^{(i)} \hat{p}_{\mathfrak{s}}^{(s)} \right\rangle & \left\langle \hat{q}_{\mathfrak{s}}^{(i)} \hat{q}_{\mathfrak{s}}^{(s)} \right\rangle & \left\langle \hat{q}_{\mathfrak{s}}^{(i)} \hat{p}_{\mathfrak{s}}^{(i)} \right\rangle & \Delta^2 \hat{q}_{\mathfrak{s}}^{(i)} \end{bmatrix} \tag{3.19}$$
$$= \begin{bmatrix} \alpha^{(s)} & \gamma^{(s)} & \mu & \xi \\ \gamma^{(s)} & \beta^{(s)} & \zeta & \nu \\ \mu & \zeta & \alpha^{(i)} & \gamma^{(i)} \\ \xi & \nu & \gamma^{(i)} & \beta^{(i)} \end{bmatrix},$$

where the Greek letters notation was introduced to simplify the expressions and to group the covariances that carry the same information. Similarly, the antisymmetric matrix is written as

$$\mathbb{V}_{\mathfrak{a}} = \frac{1}{2}\left\langle \mathbf{x}_{\mathfrak{a}} \cdot \mathbf{x}_{\mathfrak{a}}^{\mathrm{T}} + \left(\mathbf{x}_{\mathfrak{a}} \cdot \mathbf{x}_{\mathfrak{a}}^{\mathrm{T}}\right)^{\mathrm{T}} \right\rangle = \begin{bmatrix} \Delta^2 \hat{p}_{\mathfrak{a}}^{(s)} & \left\langle \hat{p}_{\mathfrak{a}}^{(s)} \hat{q}_{\mathfrak{a}}^{(s)} \right\rangle & \left\langle \hat{p}_{\mathfrak{a}}^{(s)} \hat{p}_{\mathfrak{a}}^{(i)} \right\rangle & \left\langle \hat{p}_{\mathfrak{a}}^{(s)} \hat{q}_{\mathfrak{a}}^{(i)} \right\rangle \\ \left\langle \hat{q}_{\mathfrak{a}}^{(s)} \hat{p}_{\mathfrak{a}}^{(s)} \right\rangle & \Delta^2 \hat{q}_{\mathfrak{a}}^{(s)} & \left\langle \hat{q}_{\mathfrak{a}}^{(s)} \hat{p}_{\mathfrak{a}}^{(i)} \right\rangle & \left\langle \hat{q}_{\mathfrak{a}}^{(s)} \hat{q}_{\mathfrak{a}}^{(i)} \right\rangle \\ \left\langle \hat{p}_{\mathfrak{a}}^{(i)} \hat{p}_{\mathfrak{a}}^{(s)} \right\rangle & \left\langle \hat{p}_{\mathfrak{a}}^{(i)} \hat{q}_{\mathfrak{a}}^{(s)} \right\rangle & \Delta^2 \hat{p}_{\mathfrak{a}}^{(i)} & \left\langle \hat{p}_{\mathfrak{a}}^{(i)} \hat{q}_{\mathfrak{a}}^{(i)} \right\rangle \\ \left\langle \hat{q}_{\mathfrak{a}}^{(i)} \hat{p}_{\mathfrak{a}}^{(s)} \right\rangle & \left\langle \hat{q}_{\mathfrak{a}}^{(i)} \hat{q}_{\mathfrak{a}}^{(s)} \right\rangle & \left\langle \hat{q}_{\mathfrak{a}}^{(i)} \hat{p}_{\mathfrak{a}}^{(i)} \right\rangle & \Delta^2 \hat{q}_{\mathfrak{a}}^{(i)} \end{bmatrix} \tag{3.20}$$
$$= \begin{bmatrix} \beta^{(s)} & -\gamma^{(s)} & \nu & -\zeta \\ -\gamma^{(s)} & \alpha^{(s)} & -\xi & \mu \\ \nu & -\xi & \beta^{(i)} & -\gamma^{(i)} \\ -\zeta & \mu & -\gamma^{(i)} & \alpha^{(i)} \end{bmatrix}.$$

At last, the cross correlations matrix is given by

$$\mathbb{C}_{(\mathfrak{s},\mathfrak{a})} = \left\langle \mathbf{x}_{\mathfrak{s}} \cdot \mathbf{x}_{\mathfrak{a}}^{\mathrm{T}} \right\rangle = \begin{bmatrix} \left\langle \hat{p}_{\mathfrak{s}}^{(s)} \hat{p}_{\mathfrak{a}}^{(s)} \right\rangle & \left\langle \hat{p}_{\mathfrak{s}}^{(s)} \hat{q}_{\mathfrak{a}}^{(s)} \right\rangle & \left\langle \hat{p}_{\mathfrak{s}}^{(s)} \hat{p}_{\mathfrak{a}}^{(i)} \right\rangle & \left\langle \hat{p}_{\mathfrak{s}}^{(s)} \hat{q}_{\mathfrak{a}}^{(i)} \right\rangle \\ \left\langle \hat{q}_{\mathfrak{s}}^{(s)} \hat{p}_{\mathfrak{a}}^{(s)} \right\rangle & \left\langle \hat{q}_{\mathfrak{s}}^{(s)} \hat{q}_{\mathfrak{a}}^{(s)} \right\rangle & \left\langle \hat{q}_{\mathfrak{s}}^{(s)} \hat{p}_{\mathfrak{a}}^{(i)} \right\rangle & \left\langle \hat{q}_{\mathfrak{s}}^{(s)} \hat{q}_{\mathfrak{a}}^{(i)} \right\rangle \\ \left\langle \hat{p}_{\mathfrak{s}}^{(i)} \hat{p}_{\mathfrak{a}}^{(s)} \right\rangle & \left\langle \hat{p}_{\mathfrak{s}}^{(i)} \hat{q}_{\mathfrak{a}}^{(s)} \right\rangle & \left\langle \hat{p}_{\mathfrak{s}}^{(i)} \hat{p}_{\mathfrak{a}}^{(i)} \right\rangle & \left\langle \hat{p}_{\mathfrak{s}}^{(i)} \hat{q}_{\mathfrak{a}}^{(i)} \right\rangle \\ \left\langle \hat{q}_{\mathfrak{s}}^{(i)} \hat{p}_{\mathfrak{a}}^{(s)} \right\rangle & \left\langle \hat{q}_{\mathfrak{s}}^{(i)} \hat{q}_{\mathfrak{a}}^{(s)} \right\rangle & \left\langle \hat{q}_{\mathfrak{s}}^{(i)} \hat{p}_{\mathfrak{a}}^{(i)} \right\rangle & \left\langle \hat{q}_{\mathfrak{s}}^{(i)} \hat{q}_{\mathfrak{a}}^{(i)} \right\rangle \end{bmatrix} \tag{3.21}$$
$$= \begin{bmatrix} \delta^{(s)} & 0 & \kappa & -\eta \\ 0 & \delta^{(s)} & -\tau & -\lambda \\ -\lambda & \eta & \delta^{(i)} & 0 \\ -\tau & \kappa & 0 & \delta^{(i)} \end{bmatrix}.$$

The equivalence between the several terms in the covariance matrix holds when the stationarity condition of equations (3.13) and (3.16) is satisfied.

We described the accessible information of the intensity operator and how they are related with the quadratures of the optical field. In the next sections we will give details of

our technical apparatus and which kind of information is obtained by them. We will start with the description of photodetectors and the balanced detection technique in section 3.3.1. Next, in section 3.3.2, we will describe the resonator assisted detection, how it is related to the covariance matrix coefficients of equations (3.19)–(3.21) and how the full measurement setup operates.

### 3.3.1 Photodetection and Balanced Detection

As discussed in the last section, a photocurrent is generated as the response of a detector to an optical field. In our system, the photocurrent is converted into a voltage signal by a transimpedance amplifier [3] with a correspondence of 1 mA $\rightarrow$ 1 V. As the measured signal is proportional to the intensity operator, it can be separated into two parts: a DC signal related to the mean field and a high frequency (HF) voltage containing the fluctuations. Each one of the signals is independently accessible in our system. Therefore, the DC and HF photocurrents have independent gains $g_{\mathrm{DC}}$ and $g_{\mathrm{HF}}$ that are considered to contain the electronic characteristics of the photodetector and to include all the proportionality constants needed to link the intensity operator of equation (3.3) and the measured voltage. That is

$$V(t) = V_{\mathrm{DC}}(t) + V_{\mathrm{HF}}(t) = g_{\mathrm{DC}}|\alpha(t)|^2 + g_{\mathrm{HF}}|\alpha(t)|\hat{x}(t), \tag{3.22}$$

where $\hat{x}(t)$ the accessible field quadrature.

In order to correctly retrieve the quadrature information, several technicalities related to the photodetection need to be addressed. At first, the conversion of light into current is not unitary, it is subjected to probabilistic processes. This effect is quantified by the fraction of incoming photons and the electron number in the correspondent signal. In terms of experimentally accessible variables the so called quantum efficiency ($\eta$) is given by

$$\eta = \frac{ihc}{Pe\lambda}, \tag{3.23}$$

where $i$ and $P$ are the respective measured current and optical power, $\lambda$ is the field wavelength and $h$, $c$ and $e$ are respectively the Planck constant, the speed of light and the electron charge. We then determined the quantum efficiency of the four PIN diode detectors model ETX300T from EPITAX used in our experiment with the fits shown in figure 3.15.

The four detectors used in our system are mounted in individual balanced detection schemes for signal and idler fields. This technique allows the mutual measurement of the fluctuations of the field and its correspondent shot noise value. The detectors where paired

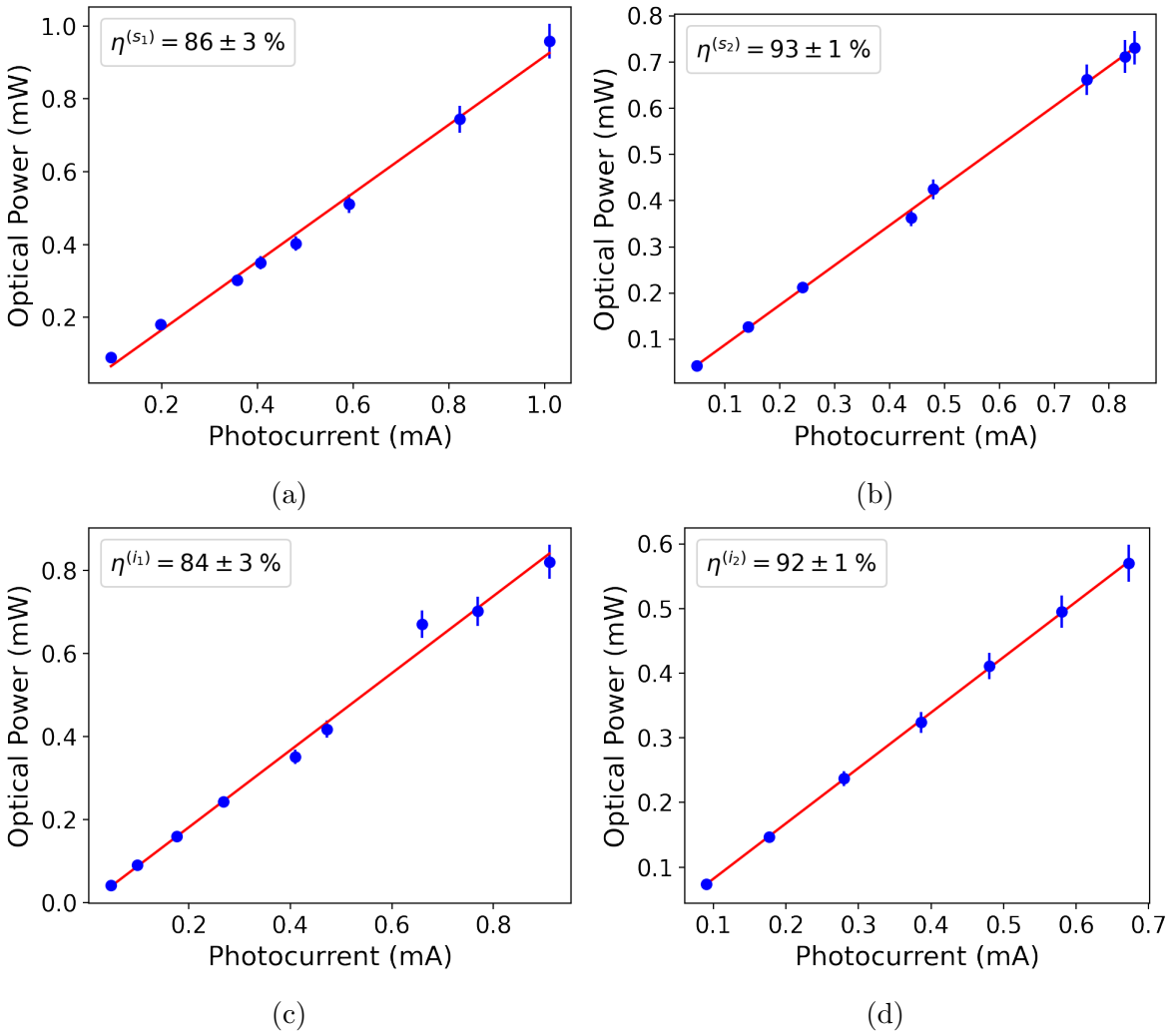


Figure 3.15: Determination of the quantum efficiency for the detectors used in our system. The detection scheme correspond to two balanced detections, where the quantum efficiencies are shown in figures (a) and (b) for the signal detectors and in figures (c) and (d) for the idler detectors. Error bars are in accordance to the power meter's (Thorlabs S122C) manufacturer information.

by similarity in the DC and HF response. We compared the DC signals and the variance of the HF photocurrents for different combinations between the detectors (together with necessary electronic amplifiers) and chose the ones closest to unitary equivalence. That is, we chose pairs of detectors with the gains as matched as possible. Figure 3.16 show examples of the DC and HF response of the selected pairs. The data acquisition was done with a National Instruments analog-digital converter model BNC-2110 and the presented results were computationally treated. One should note that the results may vary as the detection parameters, as the analysis frequency, are changed. Hence, the analysis of the relative gains is repeated for any different measurements carried out with this system.

The balanced detection scheme consists in the 50 : 50 splitting of a light field followed

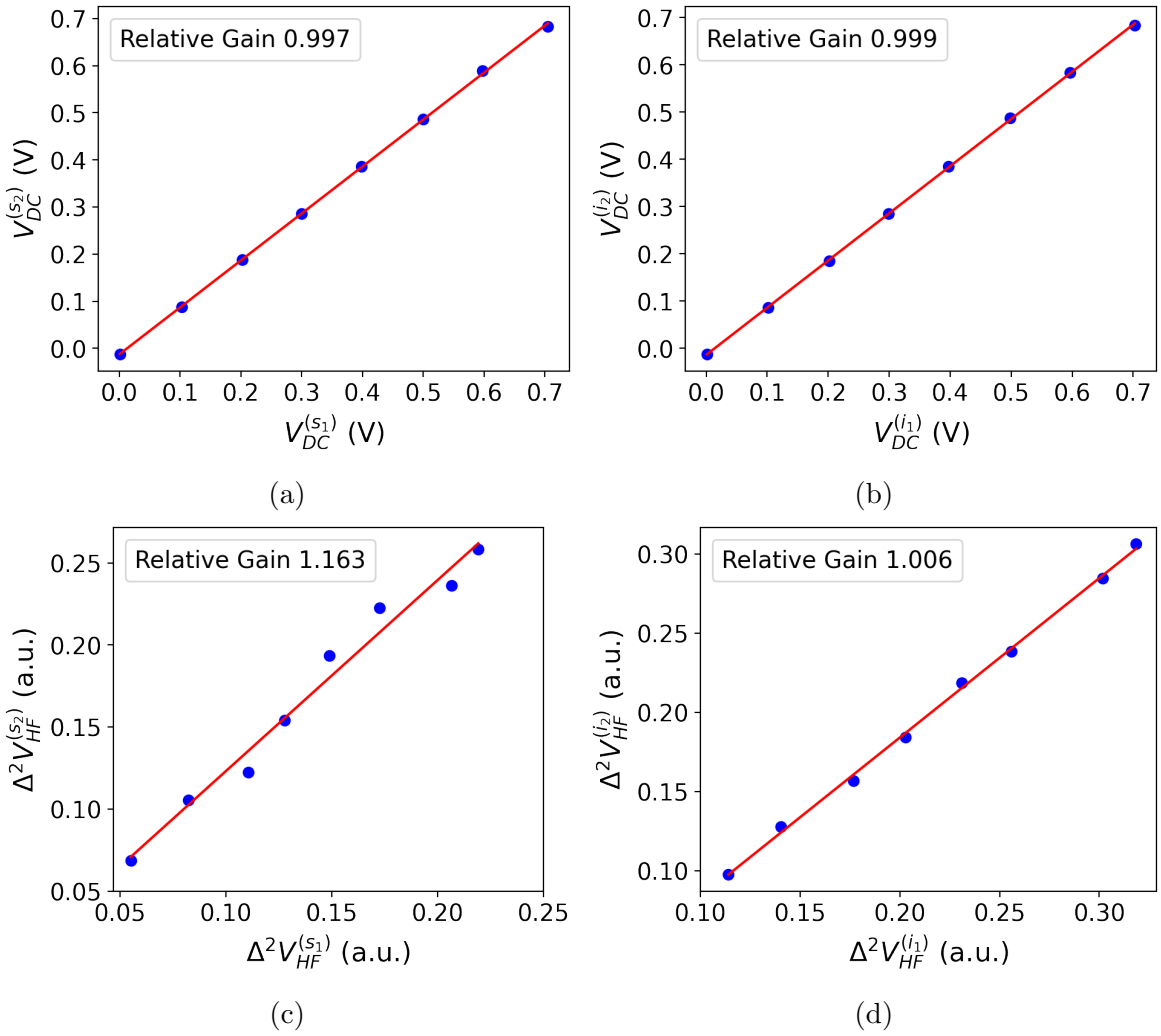


Figure 3.16: Comparison of the DC signal (a,b) and of the variance of HF signal (c,d) of the selected photodectors pairs for signal (a,c) and idler (b,d) fields. The measurements were carried with a $\Omega = 20$ MHz analysis frequency and the electronic noise was compensated in the data analysis.

by detections in each of the field arms. By the subtraction of the HF photocurrent we cancel eventual excess of noise present in the photocurrent. Hence, the variance of the subtracted signals will be equivalent to the noise of a coherent state with the same intensity as the detected field. This is equivalent to the shot noise [3], needed to determine a scale for the measured noise. The sum of the photocurrents is equivalent to the reconstruction of a single photocurrent of an optical field impinging on a photodetector. As real photodetectors present background electronic noise ($e$) [132] and the gains are not perfectly matched between the detectors, we address these error sources in our data analysis.

The electronic noise can be easily compensated for by subtracting it from the respective signals. Figure 3.17 shows the background fluctuations of our detectors. Overall electronic

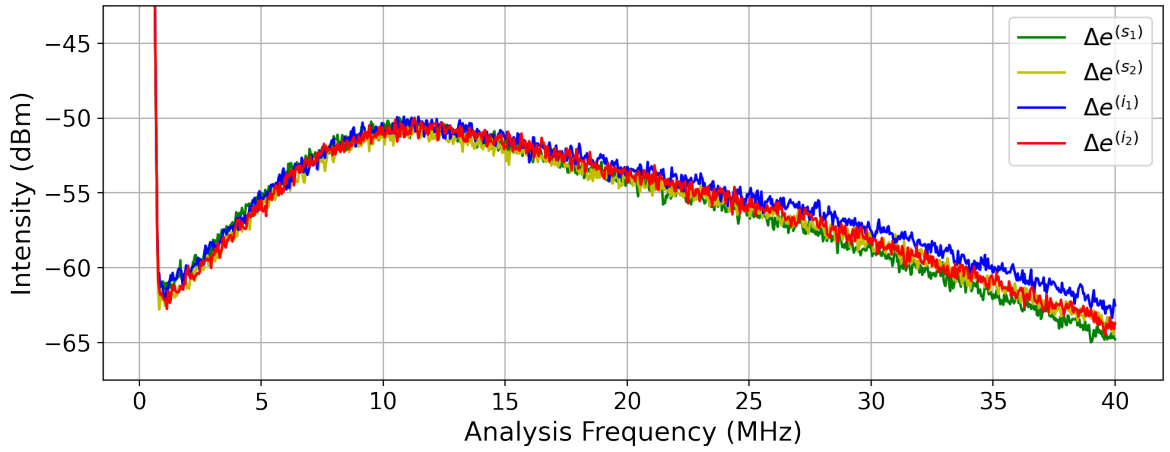


Figure 3.17: Electronic noise from the combined pairs of detectors and amplifiers. The low electronic noise in the region below 10 MHz is due to an electronic filter added to mitigate contaminations from the carrier field. The detection systems remain fairly equivalent between 10 and 25 MHz, region where we will carry our measurements. The data were acquired from an electronic spectrum analyzer model KEYSIGHT N9010B.

gains are matched with the the information from the linear adjusts in figure 3.16, where we multiply one of the signals and its electronic noise, say 1, by a relative gain given by

$$g_{\text{rel}} = \frac{\sqrt{g_{\text{HF}}^{(2)}/g_{\text{HF}}^{(1)}}}{g_{\text{DC}}^{(2)}/g_{\text{DC}}^{(1)}}, \tag{3.24}$$

where the DC part also compensates for unbalances in the beam splitter. After gain compensation, the expression for the corrected normalized noise attained by a balanced detection with detectors labeled by 1 and 2 is given by

$$\Delta^2\hat{x} = \frac{\Delta^2\left(V_{\text{HF}}^{(1)} + V_{\text{HF}}^{(2)}\right) - \Delta^2 e^{(1)} - \Delta^2 e^{(2)}}{\Delta^2\left(V_{\text{HF}}^{(1)} - V_{\text{HF}}^{(2)}\right) - \Delta^2 e^{(1)} - \Delta^2 e^{(2)}}, \tag{3.25}$$

with $\Delta^2\hat{x}$ representing the quadrature fluctuations. It is straightforward to carry out the presented analysis in order to include the correlations of different fields. The noise present in the sum and subtraction subspaces is given by

$$\begin{aligned}\Delta^2\hat{x}_{\pm} = \frac{1}{2}\left(\frac{\Delta^2 V_{\text{HF}}^{(s+)} - \Delta^2 e^{(s)}}{\Delta^2 V_{\text{HF}}^{(s-)} - \Delta^2 e^{(s)}} + \frac{\Delta^2 V_{\text{HF}}^{(i+)} - \Delta^2 e^{(i)}}{\Delta^2 V_{\text{HF}}^{(i-)} - \Delta^2 e^{(i)}}\right) \\ \pm \frac{\left\langle V_{\text{HF}}^{(s+)} V_{\text{HF}}^{(i+)}\right\rangle}{\sqrt{\left(\Delta^2 V_{\text{HF}}^{(s-)} - \Delta^2 e^{(s)}\right)\left(\Delta^2 V_{\text{HF}}^{(i-)} - \Delta^2 e^{(i)}\right)}},\end{aligned} \tag{3.26}$$

where

$$V_{\text{HF}}^{(s_\pm, i_\pm)} = V_{\text{HF}}^{(s_1, i_1)} \pm V_{\text{HF}}^{(s_2, i_2)}, \tag{3.27}$$

and

$$e^{(s,i)} = e^{(s_1,i_1)} + e^{(s_2,i_2)}. \tag{3.28}$$

For stationary processes, equation (3.13), one should note that the HF signal is equivalent to choosing any of the signals of the double demodulation scheme, since they carry the same information about the quadrature noise. Any unbalances between electronic gains are analogously compensated by the procedure described in equation (3.24)

The measured quadratures are yet subject to losses coming from the diverse experimental devices. The quantum efficiency is a significant source of such effect. In general, the presence of losses ($\mu$) are modeled as a beam splitter operation before a measurement with 100% of quantum efficiency. The beam splitter will mixture the field fluctuations with vacuum as

$$\Delta^2 \hat{x}_{\text{meas}} = \mu \left( \Delta^2 \hat{x}_{\text{real}} - 1 \right) + 1, \tag{3.29}$$

where $\hat{x}_{\text{meas}}$ is the measured result of an arbitrary quadrature and $\hat{x}_{\text{real}}$ is the value of the quadrature corrected by the losses of the system. Note that the vacuum mixture is the phenomenon that is responsible for taking a nonclassical state into a coherent one in a lossy medium.

We described the method to measure an optical quadrature with the appropriate corrections without worrying about which quadrature is being measured. As already emphasized, quadratures beyond amplitude are not accessible without interferometric processes, which will be treated in the next section.

### 3.3.2 Resonator Assisted Detection

Resonators are versatile devices in quantum optics experiments. Good reviews of their properties can be found in references [3, 133]. In this work, they play a central role in all of the experimental steps, acting as a filter in the pump preparation and as a feedback system in the generation of signal and idler in the integrated optical parametric oscillator. In our detection scheme they allow us to access several quadratures of the optical fields, which is crucial in the reconstruction of the covariance matrices. We combine the cavity output with a balanced detection scheme to obtain the shot noise value simultaneously to the measurement process, as illustrated in figure 3.18. Furthermore, each photocurrent undergoes the doubled demodulation described in figure 3.14 before acquisition. In order to keep the image clean, we chose to only show the acquisition of the HF part of the signals. The DC part as well as cavity transmission monitors are send to extra channels of the analog to digital converters. Hence, a total of 14 signals are registered in each of our

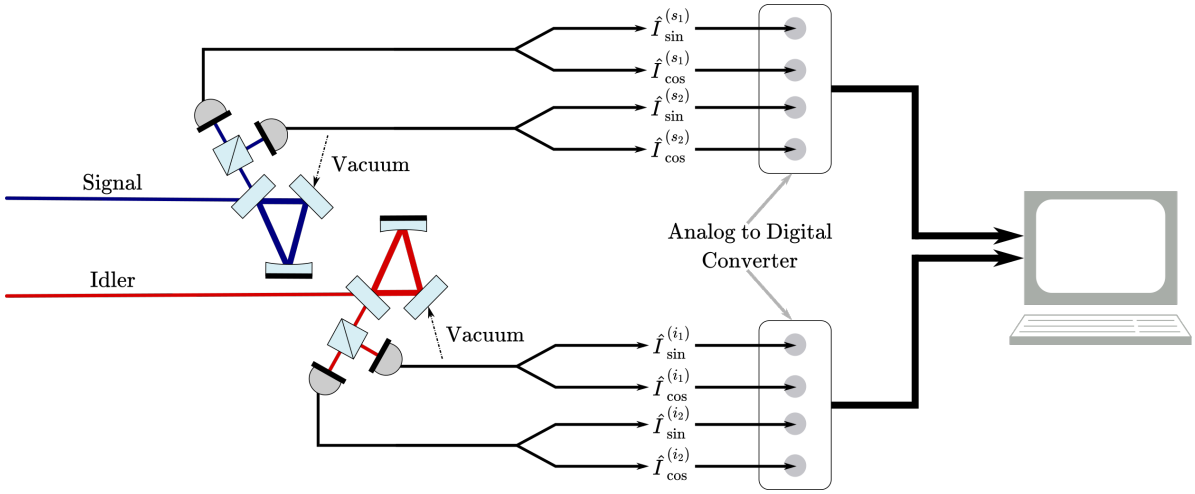


Figure 3.18: Detection setup scheme. After passing through the resonators, signal and idler undergoes a balanced detection. The double demodulated photocurrents, see figure 3.14, are individually acquired by analog to digital converters and computationally analyzed.

measurements. In the following analysis the $\hat{I}^{(s,i)}_{\sin}$ and $\hat{I}^{(s,i)}_{\cos}$ photocurrents are respectively given by

$$\hat{I}^{(s,i)}_{\sin} = \hat{I}^{(s_1,i_1)}_{\sin} + \hat{I}^{(s_2,i_2)}_{\sin}, \tag{3.30}$$

$$\hat{I}^{(s,i)}_{\cos} = \hat{I}^{(s_1,i_1)}_{\cos} + \hat{I}^{(s_2,i_2)}_{\cos}. \tag{3.31}$$

The interference of coupled light into an optical cavity and the reflected part of the field by the input mirror act as self-homodyning procedure between the carrier and the sidebands. The optical resonator transforms the spectral creation and annihilation operators as [123]

$$\hat{a}_\Omega \to r(\Delta)\hat{a}_\Omega + \sqrt{1 - r^2(\Delta)}\hat{v}_\Omega, \tag{3.32}$$

where the vacuum term ($\hat{v}_\Omega$) is introduced by the transmission coefficient. Carrying this transformation through equations (3.6)–(3.12) we obtain the effects of this interferometric process. The spectral density as a function of the detuning of the optical cavity ($\Delta$) and the demodulation frequency ($\Omega$) is then given by [123]

$$S(\Delta,\Omega) = c_\alpha\alpha + c_\beta\beta + c_\gamma\gamma + c_\delta\delta + \Delta^2\hat{v}, \tag{3.33}$$

where vacuum term couples into the cavity by the transmission mirror and is taken as $\Delta^2\hat{v} = 1 - c_\alpha - c_\beta$. The functions

$$c_\alpha = \left|g_+\right|^2, \quad c_\beta = \left|g_-\right|^2, \quad c_\gamma = 2\mathrm{Re}\{g^*_+ g_-\}, \quad c_\delta = 2\mathrm{Im}\{g^*_+ g_-\} \tag{3.34}$$

are dependent on the cavity detuning ($\Delta$) and the analysis frequency ($\Omega$). These functions depend on the parameters of the individual cavities, which are completely modeled by the

Table 3.2: Experimentally determined parameters of the analysis cavities.

| **Parameter** | Signal Cavity | Idler Cavity |
|---|---|---|
| Free Spectral Range | 1.03 GHz | 1.03 GHz |
| Bandwidth | 3.56 MHz | 4.74 MHz |
| Finesse | 290 | 218 |
| Dip | 25.8% | 13.4% |
| Mean Visibility | 97.5% | 95.7% |

mirrors reflectance ($R(\Delta,\Omega)$) as

$$g_+(\Delta,\Omega) = \frac{(R(\Delta,\Omega) + R(\Delta,-\Omega))}{2}, \tag{3.35}$$

$$g_-(\Delta,\Omega) = \frac{i\,(R(\Delta,\Omega) - R^*(\Delta,-\Omega))}{2}, \tag{3.36}$$

where the reflectance of the cavities as a function of their detunings are given by

$$R(\Delta,\Omega) = \frac{r^*(\Delta)}{|r(\Delta)|} r\left(\Delta + \frac{\Omega}{\Delta_{\mathrm{BW}}^{\mathrm{AC}}}\right). \tag{3.37}$$

The reflection coefficients, and as a consequence the $g_\pm$ functions, are experimentally determined by the measurement of the depletion magnitude of the reflected field, named dip ($d = |r(0)|^2$), and the analysis cavity bandwidth ($\Delta_{\mathrm{BW}}^{\mathrm{AC}}$). For high finesse cavities, the reflection coefficient is given by

$$r(\Delta) = -\frac{\sqrt{d} - 2i\Delta}{1 - 2i\Delta}. \tag{3.38}$$

The relevant parameters of our analysis cavities are compiled in table 3.2. We included the average visibility, which is the ratio of the energy in the main resonant peak to the total energy coupled into the resonator. It is worth to notice that these values change with the alignment of the system, which can slightly vary along the total time needed to conclude a series of mesurements. Hence, the characterization of the cavities are made before and after we run the experiment in order to estimate the total losses more accurately.

Given the cavities parameters we can analyze the behavior of the multiplicative functions of the coefficients in equation (3.33). The parameters are better accessible, or even completely hidden, from the data as these functions vary in magnitude along the cavity detuning. Figures 3.19 (a) and (b) show all the functions according to the experimental parameters of the respective signal and idler cavities.

An example is given in figure 3.20, where it is shown the spectral density, equation (3.33), of a hypothetical state with amplitude and phase normalized noises respectively given by $\Delta^2\hat{p} = 1$ and $\Delta^2\hat{q} = 2$. The taken cavity parameters are equivalent to the

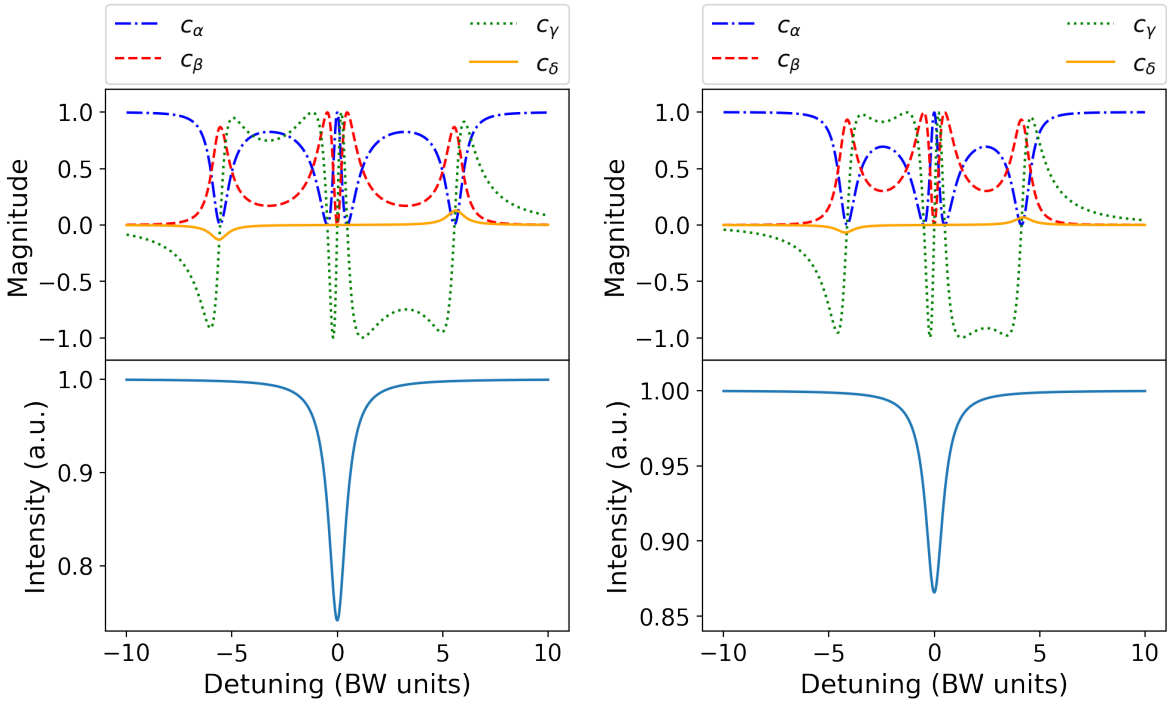


Figure 3.19: Dependency of signal (a) and idler (b) power spectrum $c_j, j = \{\alpha, \beta, \gamma, \delta\}$ on the respective analysis cavity detuning. The parameters used to determine the curves are listed in table 3.2.

signal cavity. Note that as we sweep the cavity, the exchange of the quadrature along the amplitude axis can be interpreted as rotations of the noise ellipse, see figure caption. Hence, this technique is often referred as ellipse rotation [123].

Next, we need to look at the correlations between the signal and idler photocurrents. Similarly to the analysis above, we obtain the correlations of the reflected fields by carrying the transformation (3.32) to equations (3.14) and (3.15). The real and imaginary parts of $\left\langle \hat{I}_{\Omega}^{(s)} \hat{I}_{-\Omega}^{(i)} \right\rangle$ are explicitly given by

$$\mathrm{Re}\left\{\left\langle \hat{I}_{\Omega}^{(s)}(\Delta)\hat{I}_{-\Omega}^{(i)}(\Delta)\right\rangle\right\} = c_\mu\mu + c_\nu\nu + c_\kappa\kappa + c_\lambda\lambda + c_\xi\xi + c_\zeta\zeta + c_\eta\eta + c_\tau\tau, \tag{3.39}$$

$$\mathrm{Im}\left\{\left\langle \hat{I}_{\Omega}^{(s)}(\Delta)\hat{I}_{-\Omega}^{(i)}(\Delta)\right\rangle\right\} = -c_\eta\mu - c_\tau\nu + c_\xi\kappa + c_\zeta\lambda - c_\kappa\xi - c_\lambda\zeta + +c_\mu\eta + c_\nu\tau, \tag{3.40}$$

with

$$g_+^{*(s)}g_+^{(i)} = c_\mu + ic_\eta, \quad g_-^{*(s)}g_+^{(i)} = c_\zeta + ic_\lambda, \quad g_-^{*(s)}g_-^{(i)} = c_\nu + ic_\tau, \quad g_+^{*(s)}g_-^{(i)} = c_\xi + ic_\kappa. \tag{3.41}$$

The functions are plotted in figure 3.21 (solid blue lines). As we can see, by inspecting the real and imaginary parts of equations (3.39) and (3.40), we can determine the $\mu, \nu, \kappa, \lambda, \xi, \zeta, \eta$ and $\tau$ coefficients, related to the covariance matrix by the equations (3.18)–(3.21).

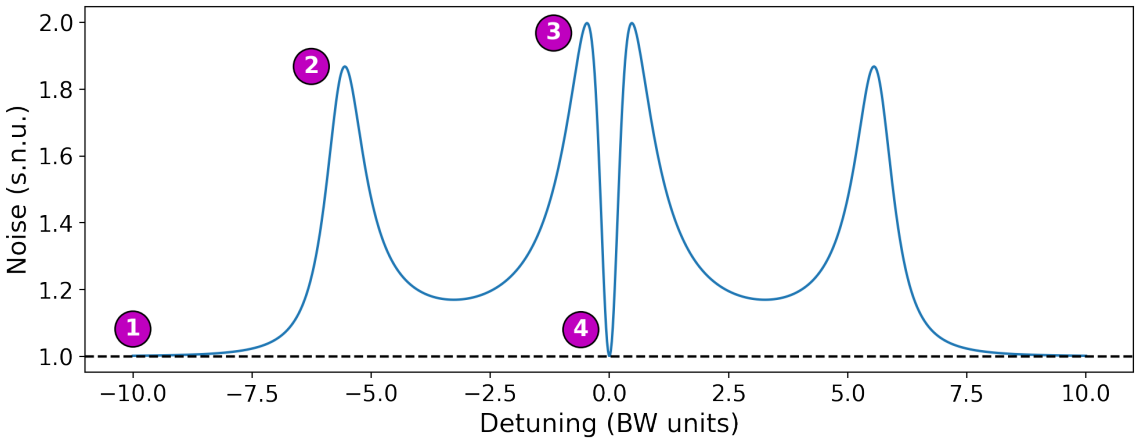


Figure 3.20: Spectral density of a thermal field with excess of phase noise. This power spectrum is equivalent to the case where $\alpha = 1$, $\beta = 2$, $\gamma = \delta = 0$. The marked points in the graphic stand to the following: 1) far from resonance the cavity does not interfere in the noise ellipse and only amplitude fluctuations are measured. 2) At resonance with the demodulated sideband (in this example 20 MHz) we have a full phase shift between amplitude and phase noise while leaving the carrier field undisturbed. The small depletion in comparison to the peak 3 is due to vacuum fluctuations disturbances. 3) This second $\pi/2$ phase-shift is due to the effect of the cavity on the carrier, where now the vacuum only attenuates its the mean field and does not disturb significantly the measured quadrature. 4) At resonance with the carrier, the noise ellipse suffers a $\pi$ phase-shift and the amplitude noise is again accessible. The dashed line is the shot noise level and s.n.u. stands for shot noise units. We used the parameters of the signal cavity to model the resonator of this example.

This analysis assumed the synchronous sweeping of the optical cavities. In order to obtain some redundancy (useful to reduce experimental errors) we can look at the correlations between different quadratures by holding one cavity far out of resonance (or exactly in resonance with the carrier) and sweep the other one. By doing this procedure to the two possible combinations, $\left\langle \hat{I}_{\Omega}^{(s)}(\Delta)\hat{I}_{-\Omega}^{(i)}(0)\right\rangle$ and $\left\langle \hat{I}_{\Omega}^{(s)}(0)\hat{I}_{-\Omega}^{(i)}(\Delta)\right\rangle$, we obtain the other curves present in figure 3.21. Note that some of the coefficients are hidden due to a null multiplicative function, which simplifies the functions (3.39) and (3.40).

In practice, we perform the three experiments described above in sequence. This gives us access to the spectral densities, equation (3.33), and the correlations of equations (3.39) and (3.40) with the functions plotted in figures 3.19 and 3.21. We then retrieve the covariance matrix coefficients from this data set, as will be described in the next chapter.

• •

Along this chapter we explored all the steps of the experimental setup used to achieve the results from this work. We first described the steps needed to generate a stabilized

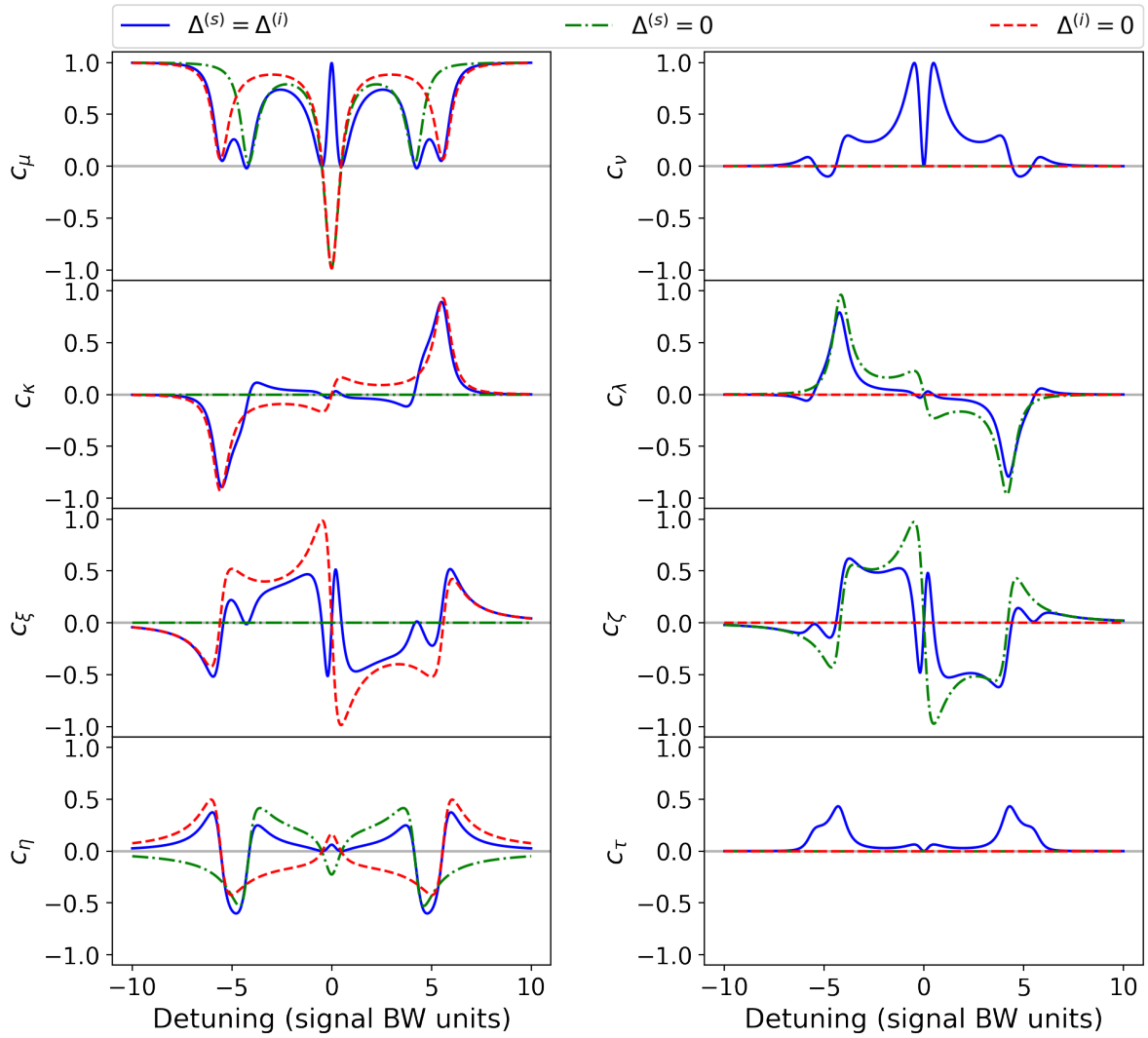


Figure 3.21: Behavior of the detuning dependent functions of equations (3.39) and (3.40) in three different experimental conditions: synchronous ellipse rotations of signal and idler (solid blue); signal ellipse rotation while the idler is kept fixed at amplitude fluctuations (dash-dotted green); idler ellipse rotation while the signal is kept fixed at amplitude fluctuations (dashed red).

near coherent optical pump, essential in the generation of optical nonclassical states.

Based on the characterization of the available microcavities, we chose the system that better suits our needs. This is a critical step since the frequency of the generated signal and idler can vary depending on the cavity and the coupled optical mode. Hence, different mode matchings and optical alignments are needed in order to carry out the resonator assisted measurements for different microcavities. Furthermore, the stabilization of the OPO oscillations is necessary to assemble the detection system and to perform the measurements.

We described all the necessary ingredients to determine all the covariance matrix coefficients with a resonator assisted detection technique. The full measurement system

consists of individual resonators for the signal and idler fields followed by a balanced detection scheme. Each photocurrent is double-demodulated before the registering of the signals. This allows us to determine the spectral densities, equation (3.33), of each field, their correlations, equations (3.39) and (3.40), and their shot noise reference. In the next chapter we will present the analysis performed over the acquired data and the resulting information retrieved from it.

The losses of the system can be properly compensated for following equation 3.29. In addition to the quantum efficiency of the detection system and the optical cavities imperfect visibilities, the described setup has significant losses in the optical path of signal and idler. We infer an 11% loss in the chip output due to reflections on the waveguide interface with air. The optical grating imposes a further 13% depletion of the fields. The other optical devices in the detection scheme path sum up to additional 9% of losses in each beam. Detection efficiency is discussed in section 3.3.1.

This setup can be expanded to include other modes in the analysis, such as the pump or secondary (or even further) oscillations coming from the OPO. Our low threshold system enables the generation of several excited modes, and even optical combs [83, 94, 95], within the current available optical powers. The investigation of such additional modes is one of the objectives for future expansions of the assembled experiment.

# Chapter 4

# Data Analysis and Results

In the previous chapters we developed all the necessary tools to generate signal and idler fields by pumping an integrated OPO with a nearly coherent field above threshold. Furthermore, we described all the detection system that allows us to determine all the covariance matrix coefficients, equations (3.18)–(3.21). Given the acquired signals described in section 3.3, we will show the methods used to analyze the data sets and the results retrieved from them. Sanity check tests performed by comparing the results obtained with our acquisition system and equivalent measurements carried out with a commercial electronic spectrum analyzer will be explored.

This chapter is organized as follows. First we will present the characterizations of the optical pump field that were realized along the evolution of the experimental setup. Then, in section 4.2, we will show the results obtained for squeezing measurements between signal and idler fields as well as the four-mode state reconstruction. From the obtained covariance matrices we will check the physicality and the purity of the generated states followed by the verification of entanglement by the PPT criterion. We then investigate the behavior of the generated states with the increasing of the optical pump power. We take advantage of the developed analysis algorithm to reconstruct all the different covariance matrices. The characteristics of the reconstructed quantum states are compared in section 4.3. Finally, we explore the consequences of phase modulation dynamics in our states.

## 4.1 Optical Pump Characterization

The optical pump is characterized by measuring the noise quadratures by the ellipse rotation technique described in section 3.3.2. Currently, we share the idler cavity with the pump, where we select the desired field with a flip mounted mirror. Since we have an appreciable difference between their wavelenghts, the cavity parameters are different. Furthermore, since we are not worried with degradation of correlations due to undesired

Table 4.1: Experimentally determined parameters of the pump analysis cavity.

| **Parameter** | Pump Cavity |
|---|---|
| Free Spectral Range | 1.03 GHz |
| Bandwidth | 3.67 MHz |
| Finesse | 281 |
| Dip | 17.1% |
| Mean Visibility | 72.5% |

losses we accepted to work with a significantly lower visibility for the pump. The relevant pump cavity parameters are compiled in table 4.1.

Before determining the spectral density of the pump field we performed the calibration of the detectors' gain, properly compensated according to equation (3.24), and carried out a shot noise calibration. Instead of directly determining the shot noise for each individual measurement, we determined a calibration curve for the shot noise with a series of measurements with varying intensities, shown in figure 4.1. We then determine the shot noise level by monitoring the DC signal of our measurement. This procedure reduces experimental errors and helps us to determine the saturation level of the detectors, as one can see for the higher intensity measurements. Note that the electronic noise of the detection system is shown in the graphic for $V = 0$.

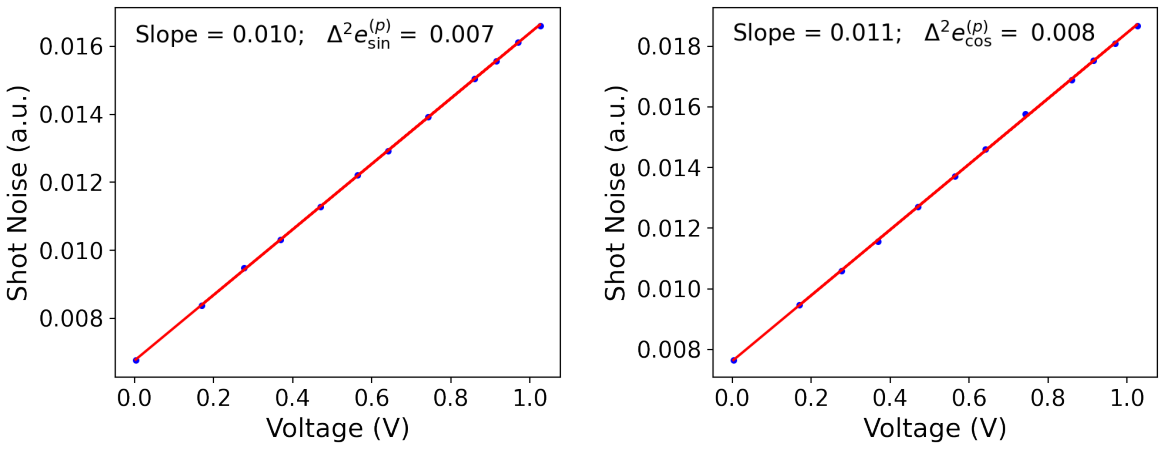


(a) (b)

Figure 4.1: Pump field shot noise calibration. (a) Shot noise for the sine demodulation. (b) Shot noise for the cosine demodulation. The electronic noise is present as a data point in both graphics.

The power spectrum of the optical source, the amplified RIO laser output, is given in figure 4.2 (a), where the fitted curve is given by equation (3.33). Following equation (3.25), we corrected the electronic noise from the result, which is normalized by the shot

noise. Due to the high noise levels we had to work with a big attenuation in order to avoid the saturation of the detectors when measuring the phase fluctuations. By comparing the obtained phase noise with the saturation levels determined by the shot noise calibration we guarantee the validity of the measurement. We then correct the spectra according to equation (3.29) to match the threshold intensity ($P_{th} \sim 13$ mW).

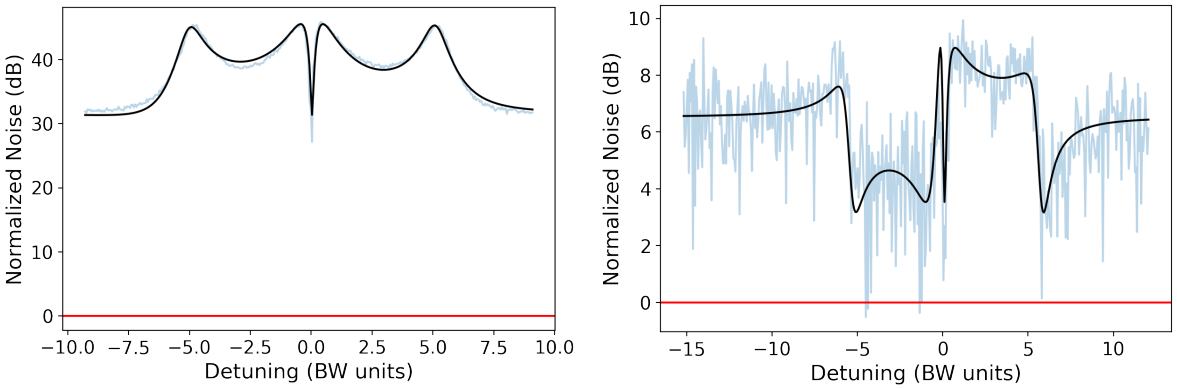


(a) (b)

Figure 4.2: Amplified laser source noise (a) and filtered light noise (b) as a function of the analysis cavity detuning. The faded blue noise are regarding experimental data corrected by the optical losses and the black solid lines the noise ellipse fitting of equation 3.33. Red lines in 0 dB are the shot noise reference. The filter cavity drastically reduces the overall noise. Furthermore, it introduced $\hat{p}$–$\hat{q}$ correlations on the state. Note that the scales are not matched to favor a better visualization of the filtered noise.

An equivalent measurement for the filtered field was carried after coupling the pump to the bus waveguide. The micro-cavity was tuned to remain out of resonance. This allowed us to investigate the noise levels that will be coupled into the integrated OPO. The effects of the filter cavity become clear in figure 4.2 (b), where we repeated the measurement process. Although the pump beam is not coherent, the noise levels were drastically reduced while the filter cavity output remained stable (see figure 3.4). The acousto-optic modulator also contributes to the remaining excess of noise. A parallel between the source of this noise and a classical modulation picture is in the distribution of energy from the modulated field to its sidebands. A good theoretical model for the effect of the AOM on the optical field noise can be found in [134].

The information achieved from figure 4.2 (b) gives us a good perspective on the power of our pump preparation system. The characterization of the pump field under different conditions gives us a realistic quantification of the noise levels that we are propagating to the signal and idler field through the optical pump. In the next section we will explore the levels of correlation that we can measure by operating the integrated OPO above threshold.

## 4.2 Signal and Idler State Reconstruction

As described in the last chapter, our experimental system allows us to reconstruct the full covariance matrix of signal and idler fields. Before we jump into the final measurements, we will present some important aspects of the system and tests carried out to guarantee proper functioning of the setup. We first show intensity measurements obtained without the interference of the analysis cavities, where we compare the results from our demodulation system with a commercial spectrum analyzer. The squeezing degradation with induced optical losses will enunciate the expected behavior of the nonclassical states. In section 4.2.2 we reconstruct the quadrature noise in the sum and subtraction subspaces by carrying the measurements while the cavities synchronously sweep around the carrier resonance. The reconstruction of the state covariance matrix is shown in section 4.2.3, followed by the exploration of the purity of the state and the application of entanglement criteria, section 4.2.4.

### 4.2.1 Amplitude Difference Squeezing and Squeezing Degradation

The first goal of our experiment was to measure optical squeezing in the amplitude difference sub-space, reproducing previous results obtained for silicon nitride micro-cavities [110, 116]. For these measurements we compared two different methods. For the first one we used an electronic spectrum analyzer (ESA) to explore amplitude correlations between signal and idler. Although more limited than our full system, this step was important to cross check our results and evaluate the reliability of the equipments at our disposal. We then compared this results with equivalent measurements done with the double demodulation scheme. The proper functioning of the system is guaranteed if similar results are achieved for both methods. Furthermore, the comparison of results allows us to evaluate problems in the data analysis.

The electronic spectrum analyzer enables us to verify the spectral band of the observed correlations, as it can be operated with spectral sweeping. Figure 4.3 shows our raw results directly comparing the amplitude difference noise of signal and idler with the shot noise. Note that, since we have a single input to the ESA, we have to determine the shot noise in different temporal measurements. We used electronic power splitters to perform sum and subtraction operations on the photocurrents, giving us access to the amplitude difference noise and the shot noise. Our measurement covers the region where the detectors remain well balanced, as discussed in section 3.3.1. The squeezing remains approximately at the

same magnitude along the observed spectrum. The crucial parameters to measure such correlations are the pump power, which will be explored in section 4.3, and the optical losses. In principle we could try to measure squeezing up to 200 MHz, limited by the OPO bandwidth, however we have electronic limitations which restrict our measurement window to approximately 35 MHz.

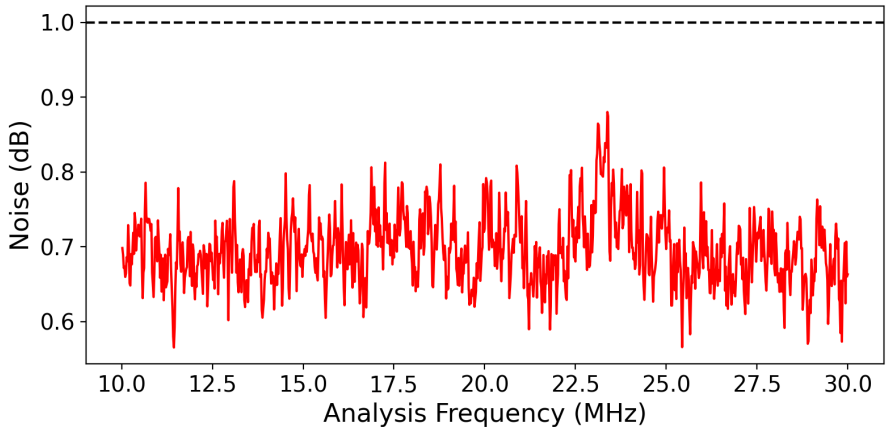


Figure 4.3: Optical squeezing at a pump power near oscillation threshold for analysis frequencies ranging from 10 MHz to 30 MHz. The dashed line indicates the shot noise level.

Next, we checked the behavior of the obtained squeezing with optical losses by adding neutral density filters in the optical path right after the chip output. The choice of attenuating the fields while spatially overlapped guarantees that signal and idler are being subjected to the same losses. On the other hand, this jeopardizes the locking system introducing instabilities to the experiment.

The degradation of squeezing with losses, shown in figure 4.4, is expected to be in accordance to equation 3.29. In order to see a clear decreasing in the squeezed level we took several measurements at each attenuation level. This is an important result to certificate that the measured nonclassical effects are not a product of possible electronics malfunctioning or analysis errors.

As a sanity test of the acquisition system, we performed equivalent measurements with the procedure described in section 3.3.1. We used the doubled demodulation scheme to measure the amplitude difference with both electronic oscillators. The shot noises were calibrated for each demodulation of each field, and are given in figure 4.5. Three measurements were performed for each one of the attenuations to mitigate the effects of the system instabilities. The presented results are a mean of such measurements and the different demodulations. The squeezing degradation is shown in figure 4.6 (a). Since we have access to the individual photocurrents in this configuration, we are able to observe

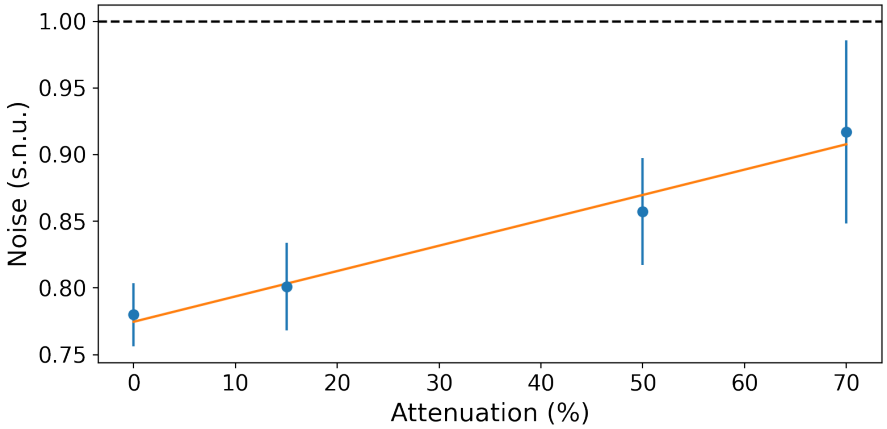


Figure 4.4: Optical squeezing as a function of the attenuation of signal and idler fields. As expected, the squeezing degrades as the optical losses increase. The fit gives a slope of $(1.90 \pm 0.02) \cdot 10^{-2}$ and an intercept of $(7.75 \pm 0.09) \cdot 10^{-1}$, leading to a noise of $0.96 \pm 0.02$ for complete attenuation. As expected, this result is compatible to the shot noise. The data was obtained with an electronic spectrum analyzer fixed at the analysis frequency of 20 MHz. Error bars are calculated by the standard deviation of the data set. We used a resolution bandwidth of 200 kHz and a video bandwidth of 20 Hz.

the degradation of the anti-squeezing on the orthogonal quadrature as well, shown in figure 4.6 (b). Another interesting manner to observe the losses effects is by varying the attenuation of the optical beam while the measurement is being carried out. The result of such procedure can be seen in figure 4.7, where we have a clear increasing of the mean value of the amplitude difference noise together with the increasing of the dispersion of the data points. The measurements were carried with the analysis frequency of 20 MHz.

The tests presented in this section assure the nonclassical nature of the effects measured. All the shown results are respective to the raw data, without any loss correction for the squeezing amount. The best squeezing directly measured was of $2.30 \pm 0.03$ dB. Taking into account the optical losses and the quantum efficiency of our photodetectors, equation (3.29), we infer a total of $4.0 \pm 0.7$ dB of squeezing at the chip output.

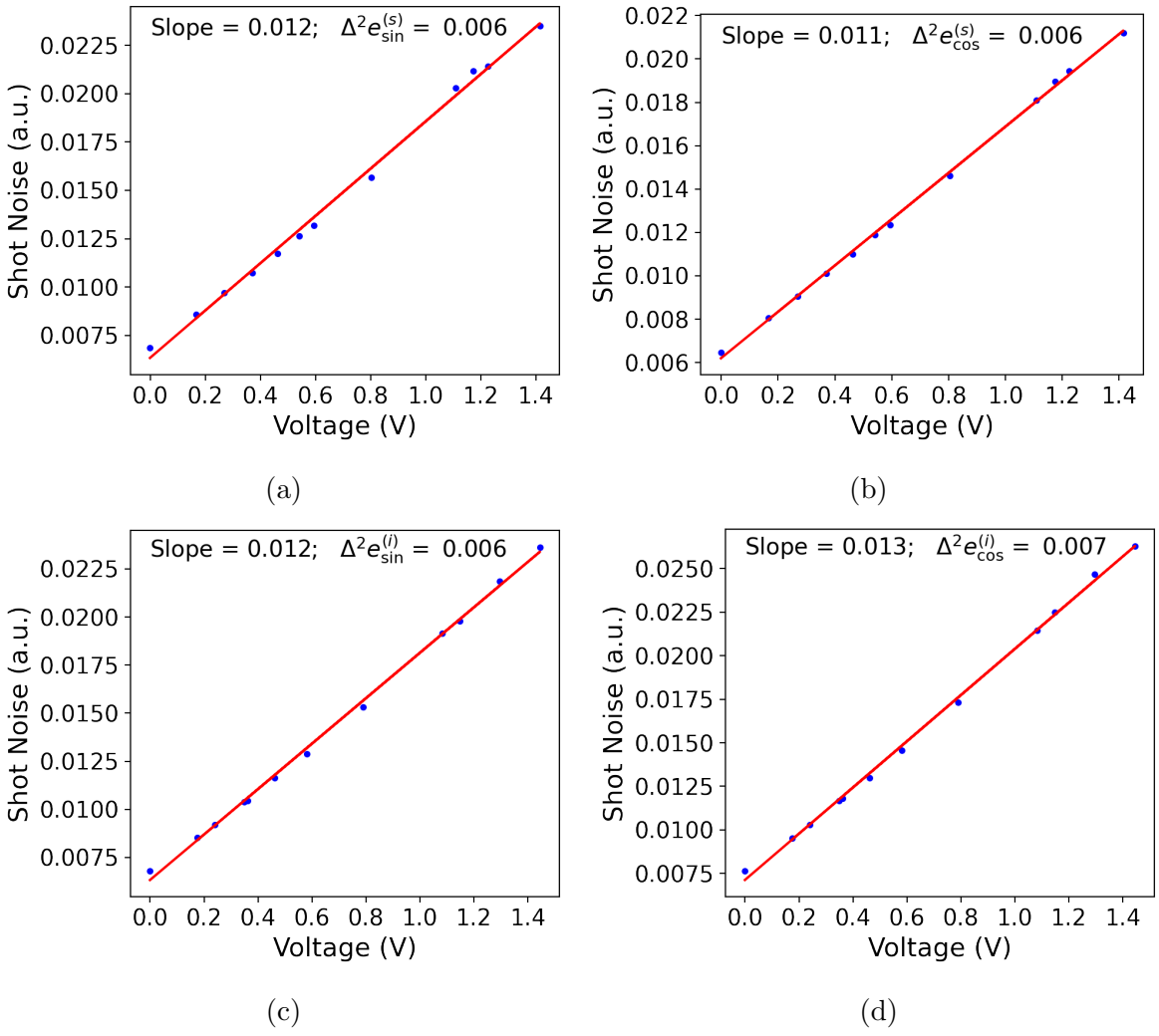


Figure 4.5: Shot noise calibration for the sine (a) and cosine (b) demodulation of the signal field and for the sine (c) and cosine (d) demodulation of the idler field.

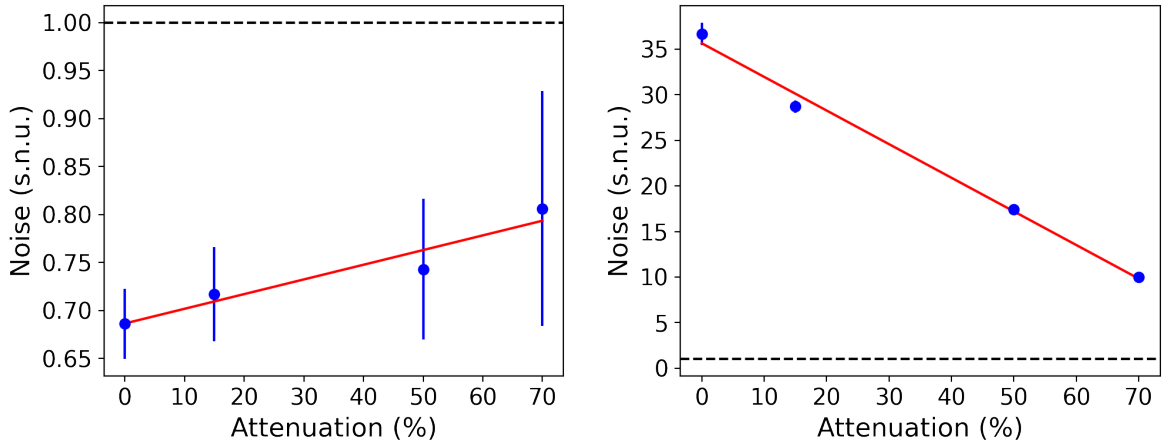


(a) (b)

Figure 4.6: Optical squeezing (a) and anti-squeezing (b) degradation as a function of the attenuation. For complete attenuation, the respective tendency curves tend toward $(8.4 \pm 0.3) \cdot 10^{-1}$ and $-1 \pm 2$. Error bars are calculated by the standard deviation of the data set.

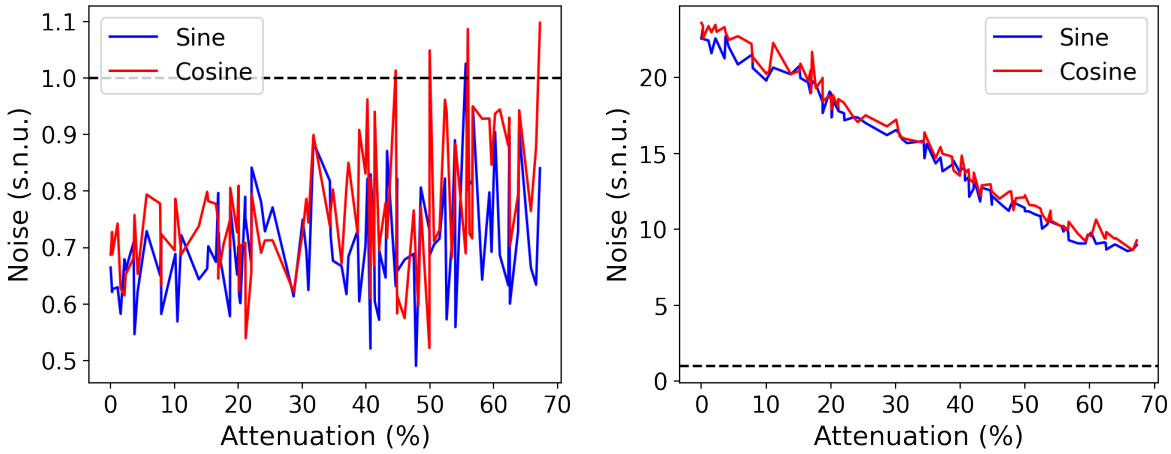


(a) (b)

Figure 4.7: Optical squeezing (a) and anti-squeezing (b) degradation as a function of the real time attenuation, performed in a 700 ms time window. The measurements carried out during the experiment present dispersion levels equivalent to the ones at the low attenuation part of the graphics.

### 4.2.2 Sum and Subtraction Subspaces

As seen in the previous section the difference of signal and idler amplitude quadratures present strong correlations, beating the shot noise level. We extend this measurements to other quadratures of the fields by taking measurements while sweeping the optical cavities, as discussed in section 3.3.2. Signal and idler quadrature noise as a function of the idler cavity detuning are shown in figure 4.8. The choice of one of the cavities as reference for the sweeping is necessary in order to compare the different signals. The curves were fitted according to the Non-Linear Least-Square Minimization and Curve-Fitting (lmfit) package for Python [135]. Our algorithm performs a least-square method to determine the optimum curve adjust and the standard deviations from the model and the data. The advantage of using the lmfit package for this task is that it allows us to fix values and impose bounds between the fitting parameters. Moreover, it is fairly simple to apply the algorithm in parallel, including bounded parameters, to different data sets. Note that the central depletion in the experimental data when the cavities are at resonance is not considered in the fits. This behavior is due to interference between the part of the carrier that was coupled into the cavity, suffering a $\pi$ phase-shift, and the part that was reflected. Partial treatment of this effect can be found in [136].

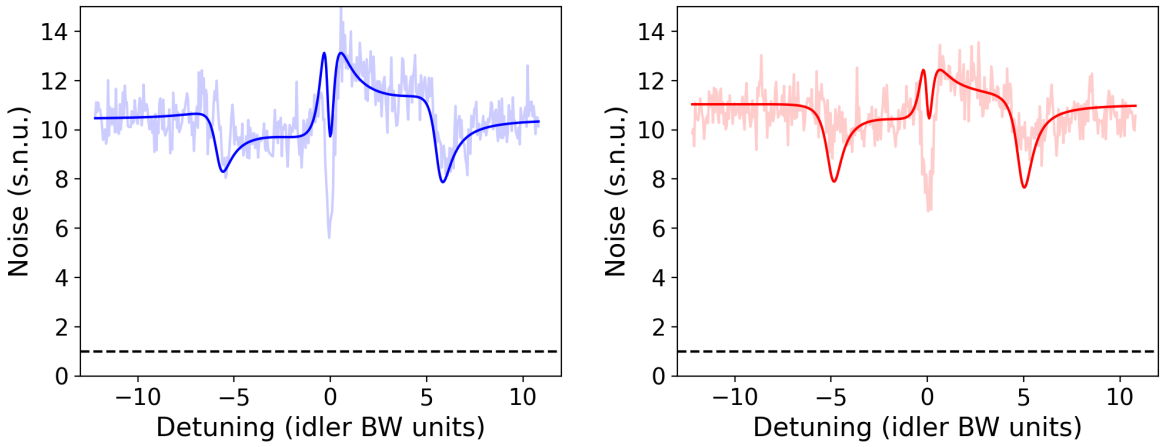


(a) (b)

Figure 4.8: Spectral density, equation (3.12), of the signal (a) and idler (b) fields. Both states are highly noisy in both amplitude and phase quadratures. The straight line is the fitting of equation (3.33) to the respective faded data set. The dip in the data at resonance is due to a interferometric effect between the reflected and the coupled part of the carrier into the cavity.

We then computed the sum and subtraction subspaces of the measured data, given by equation (3.26) and shown in the respective figures 4.9 (a) and (b). The squeezing in amplitude difference is observed in the regions far from resonance in figure 4.9 (b). Note

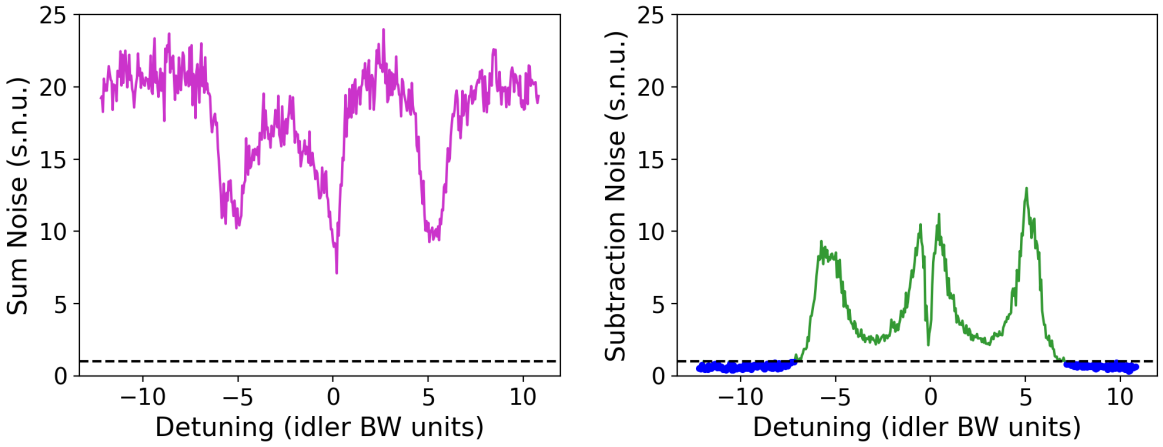


(a) (b)

Figure 4.9: Quadrature noise of the sum (a) and subtraction (b) subspaces as a function of the idler cavity detuning. Optical anti-squeezing and squeezing (blue dots) can be observed on the corners of the respective figures (a) and (b). The high levels of phase noise are seen in the peaks of the subtraction subspace and the dips in the sum subspace. In ideal conditions, the dips in figure (a) are expected to reach below shot noise levels. Horizontal dashed lines indicates the shot noise level.

that at exact resonance, despite a significant drop in the amplitude difference noise, we do not have a signature of optical squeezing. This point must be taken with skepticism since it is related to a vary fast quadrature noise exchange as the cavity passes through this point. Moreover, any asynchrony between the cavities results in a strong mixture between different quadratures. Hence, by checking the extremities of the data set, we affirm that the highly thermal fields shown in figure 4.8 are strongly correlated in amplitude. Furthermore, by looking at the same region in figure 4.9 (a) anti-squeezing is observed, as expected. While sweeping the cavity, phase noise is accessible and no clear phase correlations in the sum subspace are seen. Note that the noise levels in the sum and subtraction subspaces are of the same order. Near resonance, the expected increase in the amplitude sum noise, of the same order of the extremities of the graphic, is not observed. This is due to the fast rotation of the noise ellipses combined with the dip in the spectral densities (see figure 4.8). Moreover, the noise level is far above shot noise, which hinders any expectation of violating entanglement criteria as in equation (1.13).

The presented correlations and the excess of noise will be explored in further sections, where we will use the information of the density spectrums and the correlations obtained from our measurements to reconstruct the covariance matrix of the generated optical state. The high levels of phase noise indicates that any entanglement is hindered from our state as will be thoroughly explored in section 4.2.4.

Table 4.2: Experimentally determined parameters of the analysis cavities.

| Parameter | Related Correlations | Mean Value | Standard Deviation |
|---|---|---|---|
| $\alpha^{(s)}$ | $\Delta^2\hat{p}_{\mathfrak{s}}^{(s)} = \Delta^2\hat{q}_{\mathfrak{a}}^{(s)}$ | 10.44 | 0.03 |
| $\beta^{(s)}$ | $\Delta^2\hat{q}_{\mathfrak{s}}^{(s)} = \Delta^2\hat{p}_{\mathfrak{a}}^{(s)}$ | 12.51 | 0.09 |
| $\gamma^{(s)}$ | $\left\langle \hat{p}_{\mathfrak{s}}^{(s)}\hat{q}_{\mathfrak{s}}^{(s)} \right\rangle = -\left\langle \hat{p}_{\mathfrak{a}}^{(s)}\hat{q}_{\mathfrak{a}}^{(s)} \right\rangle$ | $-1.36$ | 0.05 |
| $\delta^{(s)}$ | $\left\langle \hat{p}_{\mathfrak{s}}^{(s)}\hat{p}_{\mathfrak{a}}^{(s)} \right\rangle = \left\langle \hat{q}_{\mathfrak{s}}^{(s)}\hat{q}_{\mathfrak{a}}^{(s)} \right\rangle$ | $-0.1$ | 0.3 |
| $\alpha^{(i)}$ | $\Delta^2\hat{p}_{\mathfrak{s}}^{(i)} = \Delta^2\hat{q}_{\mathfrak{a}}^{(i)}$ | 11.04 | 0.04 |
| $\beta^{(i)}$ | $\Delta^2\hat{q}_{\mathfrak{s}}^{(i)} = \Delta^2\hat{p}_{\mathfrak{a}}^{(i)}$ | 12.0 | 0.1 |
| $\gamma^{(i)}$ | $\left\langle \hat{p}_{\mathfrak{s}}^{(i)}\hat{q}_{\mathfrak{s}}^{(i)} \right\rangle = -\left\langle \hat{p}_{\mathfrak{a}}^{(i)}\hat{q}_{\mathfrak{a}}^{(i)} \right\rangle$ | $-0.87$ | 0.06 |
| $\delta^{(i)}$ | $\left\langle \hat{p}_{\mathfrak{s}}^{(i)}\hat{p}_{\mathfrak{a}}^{(i)} \right\rangle = \left\langle \hat{q}_{\mathfrak{s}}^{(i)}\hat{q}_{\mathfrak{a}}^{(i)} \right\rangle$ | $-0.7$ | 0.3 |

### 4.2.3 Covariance Matrix Reconstruction

In order to retrieve all the properties of the quantum state determined by the four sidebands involved in our measurements we need to further investigate the correlations between signal and idler. From the spectral densities of signal and idler fields eight parameters are readily determined from the fitted curves given by equation (3.33). We used the lmfit Python package to determine the optimal parameters and their errors. For the same data set used in last section, these parameters are listed in table 4.2. As described in section 3.3.2, three measurements are taken in sequence to reconstruct the covariance matrix. A synchronous measurement of both cavities sweeping around the resonance is followed by asynchronous measurements in which one of the cavities stays far out of resonance and vice versa. Hence, we have two degenerate measurements for each power spectrum. In order to reduce uncertainties we simultaneous fit the data sets with bounded parameters, that is, all the coefficients must remain the same along the measurement.

Note that the high error of the $\delta^{(j)}, j = \{s, i\}$ parameters are expected from the theoretical approach to the cavity assisted detection exposed in section 3.3.2. As can be seen from figures 3.19, such parameter has small multiplicative factors coming from the properties of the assembled optical cavities. Hence, we have a poor estimation of such factor and the high standard deviations can, at some cases, introduce undesired effects in our reconstructed covariance matrices. As a consequence, nonphysical states can be reconstructed if this parameter is considered. Figure 4.10 shows the difference in the fitting curves for a model taking this factor into account and a model imposing $\delta^{(j)} = 0$. As we can see, the adjusts considering this parameter are almost imperceptible. This is

expected once energy unbalances between the sidebands are not significant for the states under study [25]. Nevertheless we carried out the analysis considering both scenarios in order to closely look at the influence of these parameters. Note that the value of $\delta^{(j)}$ is irrelevant to the parameters from equations (3.39) and (3.40) and we do not need to take the above considerations in the following analysis.

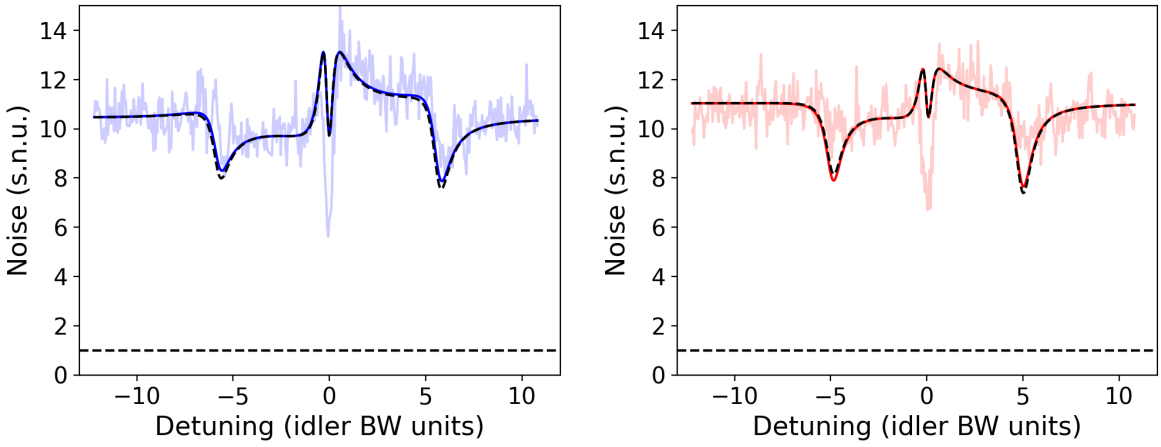


(a) (b)

Figure 4.10: Spectral density, equation (3.12), of the signal (a) and idler (b) fields. Blue and red lines are equivalent to $\delta^{(j)} = 0, j = \{s, i\}$. Black dashed lines are respective to $\delta^{(s)} = 0.1 \pm 0.3$ (a) and $\delta^{(i)} = -0.7 \pm 0.3$ (b).

The other parameters of the covariance matrix are determined by fitting equations (3.39) and (3.40) into the data set corresponding to equations (3.14) and (3.15). The three different data sets for the real and imaginary parts of $\left\langle \hat{I}_{\Omega}^{(s)} \hat{I}_{-\Omega}^{(i)} \right\rangle$ share the same coefficients, hence we can attribute bounds to the fitting routine forcing the equality of the parameters while simultaneously fitting both curves to the 6 data sets. In order to correctly preserve the measured subspace correlations, we set the extra bound given by

$$\Delta^2 \hat{p}_- = \frac{1}{2}\alpha^{(s)} + \frac{1}{2}\alpha^{(i)} - \mu, \tag{4.1}$$

where the amplitude squeezing ($\Delta^2 \hat{p}_-$) is retrieved from the subtraction subspace, as presented in figure 4.9 (b). In order to reduce uncertainties we calculate the squeezing value as the mean of the three sequential measurements. The resulting curve fits and the obtained parameters are respectively shown in figure 4.11 and in table 4.3.

The validity of the standard deviations generated by the fitting algorithm was checked with another function embedded in the lmfit package, which calculates the confidence intervals of the obtained results. We calculated the confidence intervals equivalent to multiples of the standard deviation and verified that they indeed follow the usual Gaussian distribution of the data points along the fitted curve.

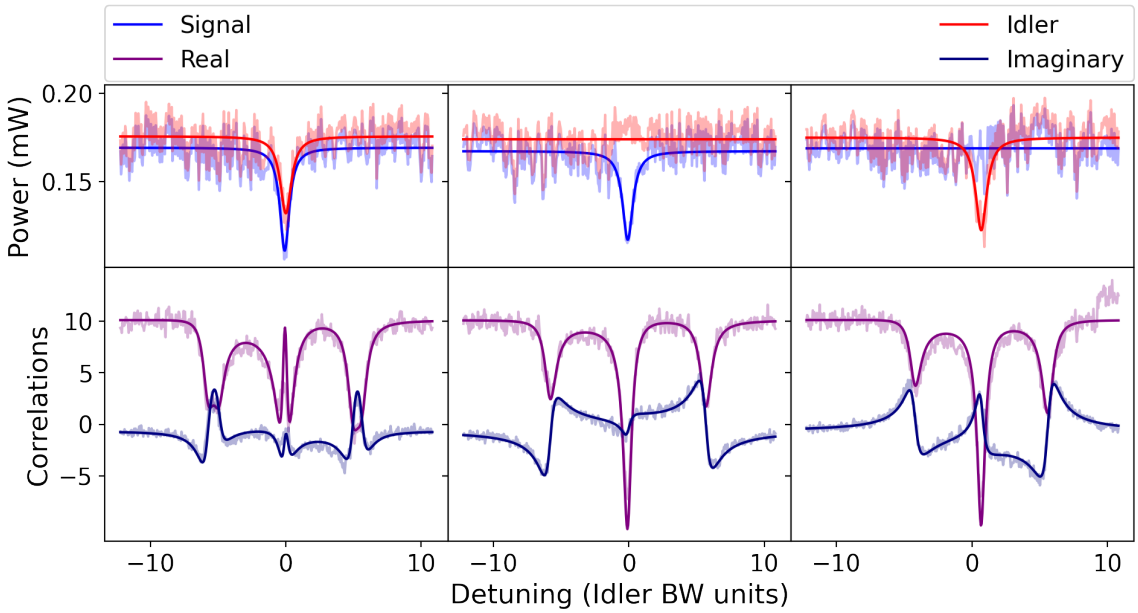


Figure 4.11: Curve fitting of the equations (3.39) and (3.40) into the respective data sets corresponding to equations (3.14) and (3.15) while synchronously sweeping both cavities and by sweeping one of the cavities while the other stays out of resonance. The demodulation frequency was set to 20 MHz. Signal and idler labels are indicating the reflected power of the cavities and real and imaginary are respectively indicating equations (3.39) and (3.40).

The results shown in tables 4.2 and 4.3 were achieved after guaranteeing the best achievable stationarity between the photocurrents, respecting equations (3.13) and (3.16). Otherwise, the overlapped demodulation channels would lead to a mixture of equations (3.14) and (3.15) in their output, shown to be significant for the high levels of noise present in our measurements. Stationarity can be checked by operating the photocurrents according to equations (3.13) and (3.16). We noticed a discrepancy on the experimental electronic phase and the theoretical one in preliminary tests of the system. As the double demodulation assumes a phase of 90 degrees between the sine and cosine channels, the first attempt of proper orthogonal demodulation was performed by configuring the function generator to this condition. Checking the photocurrents we noticed that stationarity was not being properly respected. We avoided this effect by fine tuning the delay between the sine and cosine signals coming from the function generator. The effects of this procedure on the stationarity conditions are shown in figure 4.12. The role of stationarity was well discussed in references [25, 136].

We presented the method to obtain all the coefficients and standard deviations of the four-mode covariance matrix in the symmetric and antisymmetric basis. Next we will explore the state properties that can be retrieved from the obtained results.

Table 4.3: Experimentally determined parameters of the analysis cavities.

| Parameter | Related Correlations | Mean Value | Standard Deviation |
|---|---|---|---|
| $\mu$ | $\left\langle \hat{p}_s^{(s)} \hat{p}_s^{(i)} \right\rangle = \left\langle \hat{q}_a^{(s)} \hat{q}_a^{(i)} \right\rangle$ | 10.1 | 0.2 |
| $\nu$ | $\left\langle \hat{q}_s^{(s)} \hat{q}_s^{(i)} \right\rangle = \left\langle \hat{p}_a^{(s)} \hat{p}_a^{(i)} \right\rangle$ | 0.57 | 0.09 |
| $\kappa$ | $\left\langle \hat{p}_s^{(s)} \hat{p}_a^{(i)} \right\rangle = \left\langle \hat{q}_s^{(s)} \hat{q}_a^{(i)} \right\rangle$ | $-0.50$ | 0.06 |
| $\lambda$ | $-\left\langle \hat{p}_s^{(a)} \hat{p}_s^{(i)} \right\rangle = -\left\langle \hat{q}_a^{(a)} \hat{q}_s^{(i)} \right\rangle$ | 1.84 | 0.06 |
| $\xi$ | $\left\langle \hat{p}_s^{(s)} \hat{q}_s^{(i)} \right\rangle = -\left\langle \hat{q}_a^{(s)} \hat{p}_a^{(i)} \right\rangle$ | $-1.45$ | 0.06 |
| $\zeta$ | $\left\langle \hat{q}_s^{(s)} \hat{p}_s^{(i)} \right\rangle = \left\langle \hat{p}_a^{(s)} \hat{q}_a^{(i)} \right\rangle$ | $-0.74$ | 0.06 |
| $\eta$ | $-\left\langle \hat{p}_s^{(s)} \hat{q}_a^{(i)} \right\rangle = \left\langle \hat{q}_a^{(s)} \hat{p}_s^{(i)} \right\rangle$ | $-0.66$ | 0.02 |
| $\tau$ | $-\left\langle \hat{q}_s^{(s)} \hat{p}_a^{(i)} \right\rangle = \left\langle \hat{p}_a^{(s)} \hat{q}_s^{(i)} \right\rangle$ | $-2.62$ | 0.09 |

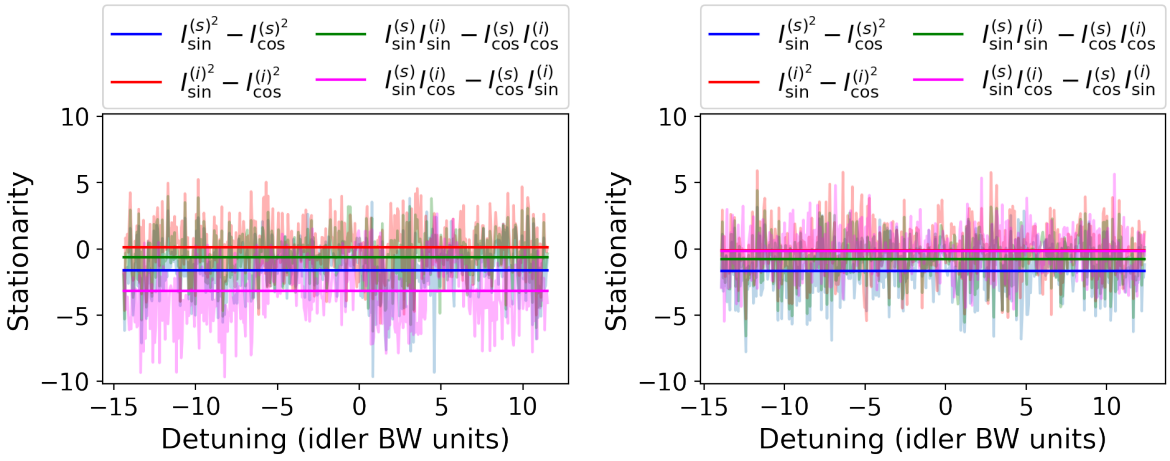


Figure 4.12: Stationarity conditions for 90 degrees delay (a) and for 86 degrees delay (b) between the sine and cosine demodulation signals as configured in the function generator. In figure (b) we note a significant improvement in the stationarity condition of equation (3.16). The mean values are implicit in the labels.

### 4.2.4 Physicality, Purity and Entanglement

In possession of the covariance matrix, the first thing that we evaluated is the validity of our state. As discussed in section 1.1, a covariance matrix that corresponds to valid physical density matrix must respect the uncertainty relation of equation 1.5. This is easily verified by computing the symplectic eigenvalues of the reconstructed matrix. Carrying the example presented in last section we have, for equation 1.6,

$$\mathbb{V}_D = \mathrm{Diag}\{1.78, 1.78, 3.37, 3.37, 14.69, 14.69, 17.93, 17.93\}. \tag{4.2}$$

Hence, we have a *bona fide* physical state.

The purity of the measured state can also be easily determined directly from the covariance matrix or from the determined symplectic $\nu_j, j = \{1, 2, 3, 4\}$ eigenvalues. Note that we grouped the degenerate values in our notation. As expected from the analysis of section 4.2.2 the measured state is highly mixed. According to equation (1.7), the purity of the example measurement is of $\mathfrak{p} = 4.01 \times 10^{-7}$.

With the covariance matrix in hand we can easily look at the PPT criteria, described in section 1.1, for the different bipartitions of the state. In order to have a more intuitive description we first transform the state to the $\pm\Omega$ sideband basis by applying the transformation given by

$$\mathbb{B}_{\pm\Omega} = \frac{1}{\sqrt{2}} \begin{bmatrix} 1 & 0 & 0 & 0 & 1 & 0 & 0 & 0 \\ 0 & 1 & 0 & 0 & 0 & 1 & 0 & 0 \\ 0 & 0 & 1 & 0 & 0 & 0 & 1 & 0 \\ 0 & 0 & 0 & 1 & 0 & 0 & 0 & 1 \\ 1 & 0 & 0 & 0 & -1 & 0 & 0 & 0 \\ 0 & 1 & 0 & 0 & 0 & -1 & 0 & 0 \\ 0 & 0 & 1 & 0 & 0 & 0 & -1 & 0 \\ 0 & 0 & 0 & 1 & 0 & 0 & 0 & -1 \end{bmatrix}. \tag{4.3}$$

We compiled the minimum symplectic eigenvalue resulting from the partial transposition of all partitions of the system in table 4.4. Some of the symmetric transpositions are omitted in order to maintain a concise table. As expected, there is no evidence of entanglement between the substates.

The optical states that we are retrieving from the integrated OPO are highly mixed and unentangled. Nevertheless, strong intensity correlations are still observable. This results were reproducible for several iterations of the exemplified measurement. Next, we will evaluate the behavior of the system for different oscillation conditions.

Table 4.4: Evaluation of the PPT criteria for the different modes of the system, where $s_\pm$ stands for the upper and lower signal sidebands and $i_\pm$ the upper and lower idler sidebands. In the notation, modes on one side of the $\times$ symbol are transposed while the modes on the other side of the $\times$ symbol remain unchanged.

| **Transposition** | **Minimum Symplectic Eigenvalue** |
|---|---|
| $[s_+ \times s_-, i_+, i_-]$ | 1.98 |
| $[s_- \times s_+, i_+, i_-]$ | 1.98 |
| $[i_+ \times s_+, s_-, i_-]$ | 2.17 |
| $[i_- \times s_+, s_-, i_+]$ | 2.17 |
| $[s_+, s_- \times i_+, i_-]$ | 2.28 |
| $[s_+, i_+ \times s_-, i_-]$ | 2.47 |
| $[s_+, i_- \times s_-, i_+]$ | 2.51 |

## 4.3 Noise Dependence on Pump Power

Once we have the methodology of data analysis defined, we can apply it to several different measurements. Since the system is stable when operating above threshold, we repeated the procedure described in last sections for different pump powers. The measurements were made in sequence in a period of 40 minutes to avoid experimental discrepancies due to misalignments or changes in the environmental conditions. We reconstructed a total of 23 covariance matrices, from which we explored the evolution of some properties with a growing pump power.

First, we observe the behavior of the individual spectral densities. Amplitude and phase fluctuations of signal and idler beams are shown in the respective figures 4.13 (a) and (b). The growth of quadrature noise increases tens of shot noise units. Hence, any unbalances between the beams caused by the dynamics of the system will lead to degradation of correlations. Figure 4.14 (a) shows the degradation of optical squeezing with the enhancing pump power. This is in contrast with similar observations in $\chi^{(2)}$ OPOs, where the amplitude correlations are robust against variations in the pump power [15]. As for the dynamics of the $\chi^{(3)}$ OPO developed in section 2.2.2, this robustness should also be present. Note that $\delta\hat{p}_-$ does not change in the dynamical equation (2.52). However, the unbalances of signal and idler beams are not accounted for in the exposed model. As no significant correlations are seen in the sum subspace, the increasing of phase fluctuations of signal and idler indicates the growth of phase sum fluctuations as well. This effect can be seen in figure 4.14 (b). Due to the high phase noise, the saturation of the detectors can be seen for the measurements with sideband powers superior to 1 mW in the same figure. All the measurements were corrected for the optical losses coming from

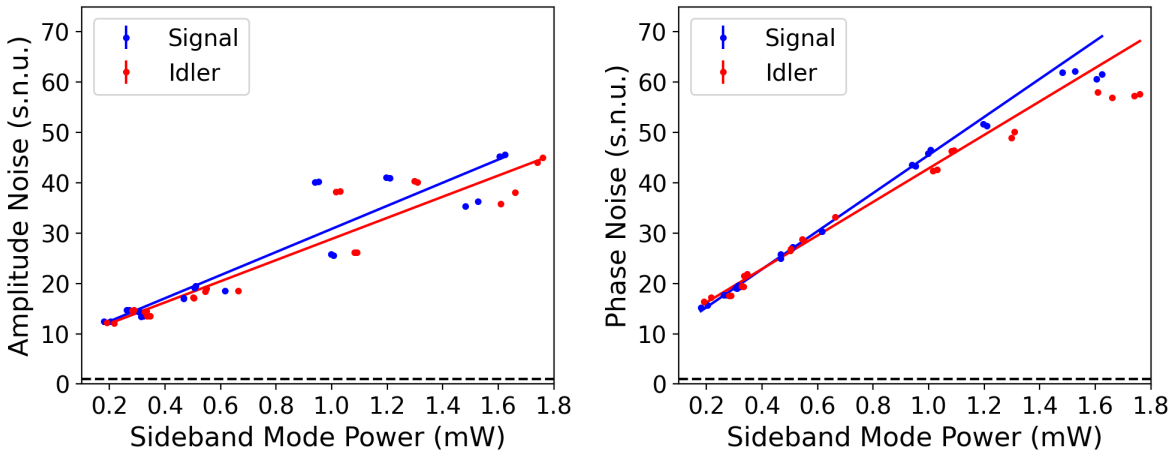


(a) (b)

Figure 4.13: Amplitude (a) and phase (b) noise for signal and idler fields as a function of the respective fields optical powers. The linear fits are included for a clear observation of the growth tendency.

different optical devices (diffraction grating, beam splitters, mirrors, lenses, waveplates), cavity visibilities and quantum efficiencies.

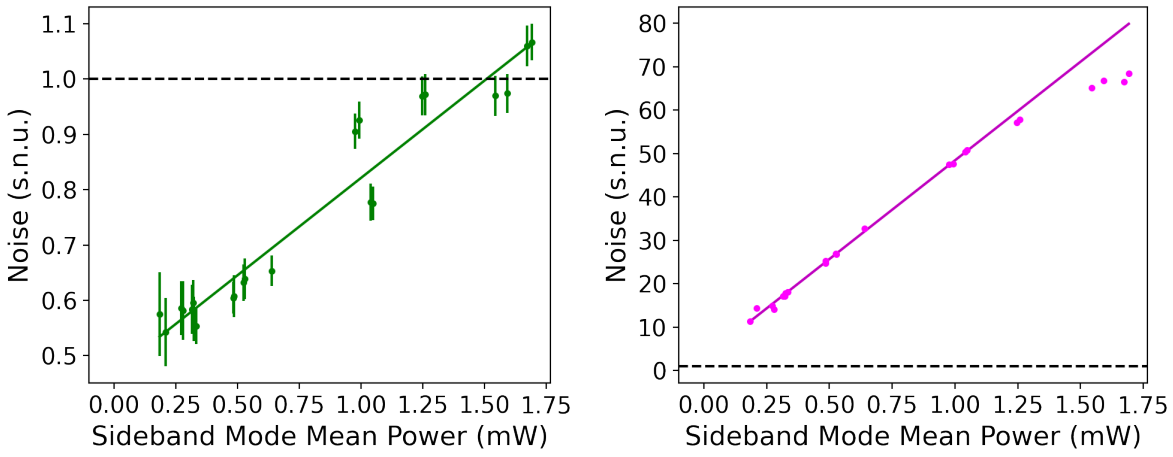


(a) (b)

Figure 4.14: Amplitude difference (a) and phase sum (b) noise as a function of the mean value of signal and idler optical powers. The linear fits are included for a clear observation of the growth tendency.

As done in last section, we can verify the physicality and the purity of our states by calculating the symplectic eigenvalues of the reconstructed covariance matrices. We compiled the minimum symplectic eigenvalue figure 4.15 (a), from which we can observe that all the considered states in the previous analysis are physical. Moreover, the fast increasing in the mixedness of the states with the increasing pump power can be observed in figure 4.15 (b). Following the PPT test carried out in section 4.2.4, we verify the mini-

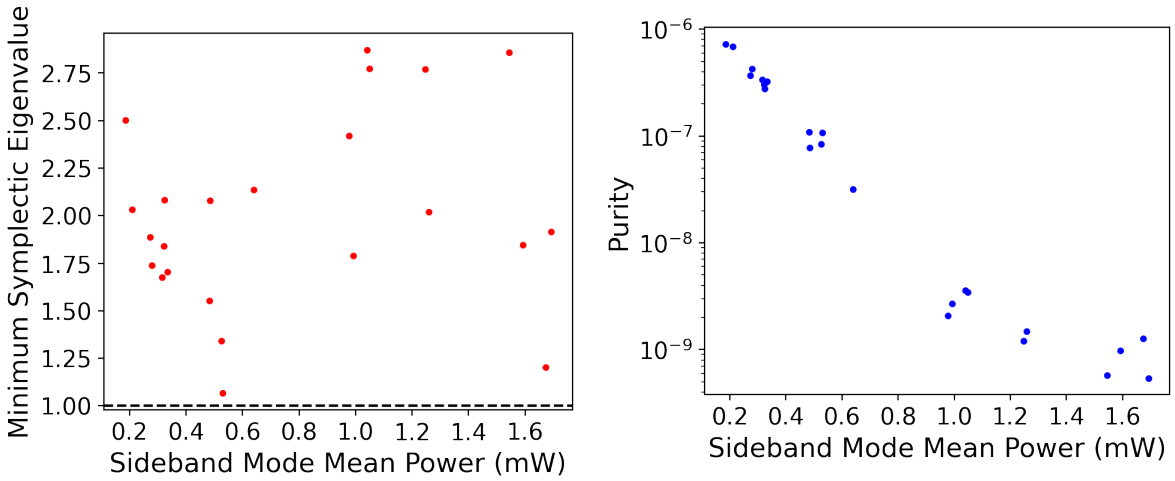


(a) (b)

Figure 4.15: Properties obtained from the symplectic eigenvalues of the covariance matrices. (a) Physicality of the states indicated by the greater than one minimum symplectic eigenvalues. (b) Purity of the states in logarithmic scale.

mum symplectic eigenvalues for the different transpositions of all reconstructed covariance matrices. The results are compiled in figure 4.16, where no evidence of entanglement is present.

Taking advantage of the shared analysis cavity we carried out similar measurements as the above for the pump field. The measurements were done maintaining the cavity in resonant condition operating below threshold. The lock system described in section 3.2.2 does not hold in this regime, since we do not have the depletion of the pump due to sideband modes excitation. Alternatively we maintained the resonant condition passively while performing the measurements. The resulting pump behavior is shown in figure 4.17. In order to accurately retrieve the behavior of the increasing pump we took degenerate measurements for each chosen intensity level, hence the clusters of points at the different intensities.

The approximately linear behavior of the fast increasing of pump phase noise with intensity is in agreement with previous evidence of photon scattering caused by phonons in $\chi^{(2)}$ cystals [137]. Furthermore, investigations of the influence of thermal noise in light propagating in waveguides are compatible to a thermorefractive origin [138]. The phase noise in microresonators was also evidenced in [139], where the phase noise is independent of the pump power, diverging from our results. While we do not have a conclusive physical source of the excess of noise measured, we do expect it to be of thermal nature. Therefore, the mitigation of the excessive phase noise may be achieved by cooling the system. This indicates a path for future works in our experiment, where temperature control may

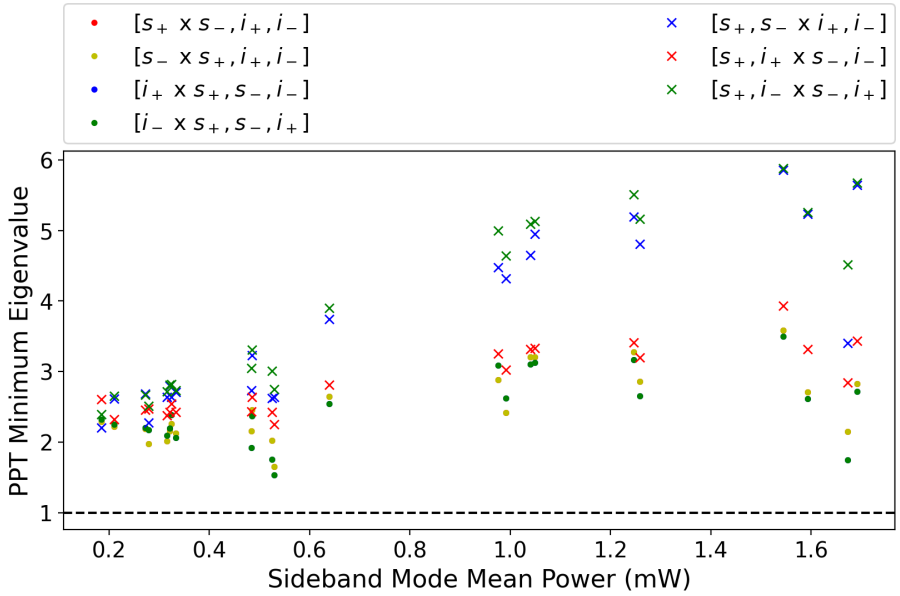


Figure 4.16: PPT test for different transpositions for the reconstructed covariance matrices. The dashed line indicating the value 1 represents the condition of physicality described in section 1.1. None of the substates are entangled since no minimum symplectic eigenvalue is below 1.

contribute for the generation of entangled states in the above threshold integrated OPO.

## 4.4 Phase Modulation Effects

As discussed in section 2.2.2, the dynamics of $\chi^{(3)}$ systems entails in self-phase and cross-phase modulations that distort the noise ellipse. This effect is noticeable through amplitude–phase correlations in each optical mode. We explore this property by reducing the four-mode covariance matrix into a two-mode representation, given by the spectral matrix [25]. In this semiclassical approach, we relate the field quadratures with complex Fourier photocurrent components, which effectively carries the same information of the reconstructed covariance matrices.

As described in [25], we define the two-mode spectral matrix as

$$\mathbb{S} = \left\langle \mathbf{x}_{\Omega}^{(j)} \cdot \left(\mathbf{x}_{-\Omega}^{(j)}\right)^{\mathrm{T}} \right\rangle, \tag{4.4}$$

where

$$\mathbf{x}_{\Omega}^{(s,i)} = \left[\hat{\mathcal{P}}_{\Omega}^{(s)}, \hat{\mathcal{Q}}_{\Omega}^{(s)}, \hat{\mathcal{P}}_{\Omega}^{(i)}, \hat{\mathcal{Q}}_{\Omega}^{(i)}\right]^{\mathrm{T}}. \tag{4.5}$$

The newly defined non-Hermitian operators are related to the symmetric and antisym-

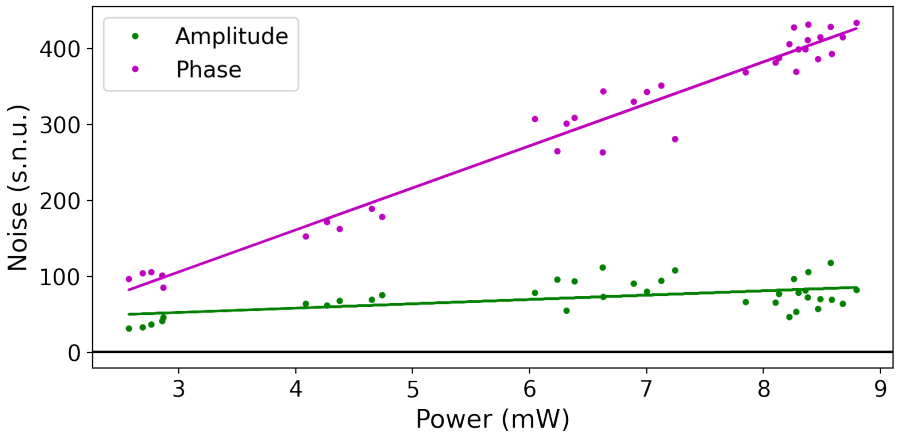


Figure 4.17: Amplitude and phase noise of the pump field quadratures as a function of the pump power. These measurements were taken for under threshold resonant condition. Linear fits are included for visual guidance.

metric quadratures as

$$\hat{\mathcal{P}}_{\Omega}^{(j)} = \frac{1}{\sqrt{2}}\left(\hat{p}_{\mathfrak{s}} + i\hat{q}_{\mathfrak{a}}\right), \tag{4.6}$$

$$\hat{\mathcal{Q}}_{\Omega}^{(j)} = \frac{1}{\sqrt{2}}\left(\hat{q}_{\mathfrak{s}} - i\hat{p}_{\mathfrak{a}}\right), \quad j = \{s, i\}. \tag{4.7}$$

Although they do not represent proper observable quadratures of the field, they reconstruct observable spectral densities when applied to equation (2.54). Explicitly developing equation (4.4) in terms of the covariance matrix parameters, the spectral matrix is written as

$$\mathbb{S} = \begin{bmatrix} \alpha^{(s)} & \gamma^{(s)} & \mu & \xi \\ \gamma^{(s)} & \beta^{(s)} & \zeta & \nu \\ \mu & \zeta & \alpha^{(i)} & \gamma^{(i)} \\ \xi & \nu & \gamma^{(i)} & \beta^{(i)} \end{bmatrix} + i \begin{bmatrix} 0 & \delta^{(s)} & \eta & \kappa \\ -\delta^{(s)} & 0 & \lambda & \tau \\ -\eta & -\lambda & 0 & \delta^{(i)} \\ -\kappa & -\tau & -\delta^{(i)} & 0 \end{bmatrix}. \tag{4.8}$$

The imaginary part of the matrix is related to correlations between the symmetric and antisymmetric operators, equivalent to correlations between individual sidebands of signal and idler. On the other hand, the real part gives us a description of signal and idler and their correlations equivalent to the one obtained from tomographies performed with homodyne detection schemes. In this picture we are ignoring the correlations between the symmetric or antisymmetric part of the field. Although not complete, this representation is sufficient to explore the dynamical effects on the sum and subtraction subspaces, as described by equation (2.52). One should note that in the absence of $\mathfrak{s}/\mathfrak{a}$ correlations the spectral matrix is a valid covariance matrix and completely maps the four-mode state into a half-dimensional description.

Taking the real part of $\mathbb{S}$, we can easily identify significant $\hat{p}^{(j)}/\hat{q}^{(j)}$, correlations as the $\gamma^{(j)}$ terms. We diagonalized the main diagonal $2 \times 2$ blocks to get into the rotated

frame. From the diagonalization processes we determine the rotation $2 \times 2$ matrices $(\mathbb{R}_\theta^{(j)})$ for each mode. We then rotate the spectral matrix into this new frame by applying the transformation

$$\mathbb{S}_\theta = \mathbb{R}_\theta \mathbb{S} \mathbb{R}_\theta^{-1}, \tag{4.9}$$

where

$$\mathbb{R}_\theta = \begin{bmatrix} \mathbb{R}_\theta^{(s)} & 0 \\ 0 & \mathbb{R}_\theta^{(i)} \end{bmatrix}. \tag{4.10}$$

The rotations are represented in the usual way as

$$\mathbb{R}_\theta^{(j)} = \begin{bmatrix} \cos\theta_j & \sin\theta_j \\ -\sin\theta_j & \cos\theta_j \end{bmatrix}. \tag{4.11}$$

The rotation angles of the signal and idler noise ellipses are compiled in figure 4.18, where it is evident that all our states are significantly affected by dynamical phase modulations. This effect mixes amplitude and phase quadratures and is one of the responsible effects for the amplitude degradation shown in figure 4.14 (a).

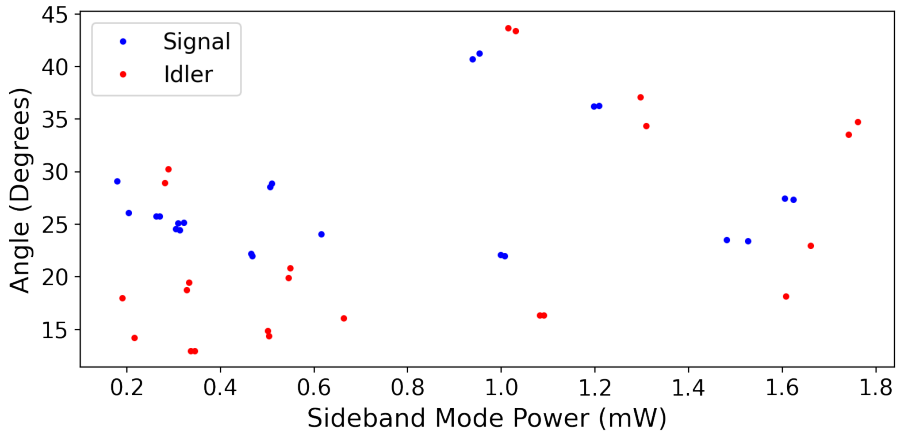


Figure 4.18: Rotation angles that independently aligns the axis of signal and idler noise ellipses, as illustrated in figure 2.9. All the measurements present appreciable angles, indicating the influence of phase modulations in the dynamics of the system.

The comparison of amplitude and phase noise between the original and the rotated frames are shown in the respective figures 4.19 and 4.20, where clear tendencies are seen for all points as the amplitude noises are reduced in contrast with an increasing phase noise. We also compared the amplitude difference and phase sum correlations between the original and the rotated frames in the respective figures 4.21 (a) and (b). As we can see, although phase sum (classical) correlation is retrieved, we have completely lost amplitude compression. This is explained by the influence of the excessive phase noise in this new "amplitude" quadrature. If the excessive noise is mitigated we expect stronger subtraction correlations in the rotated frame.

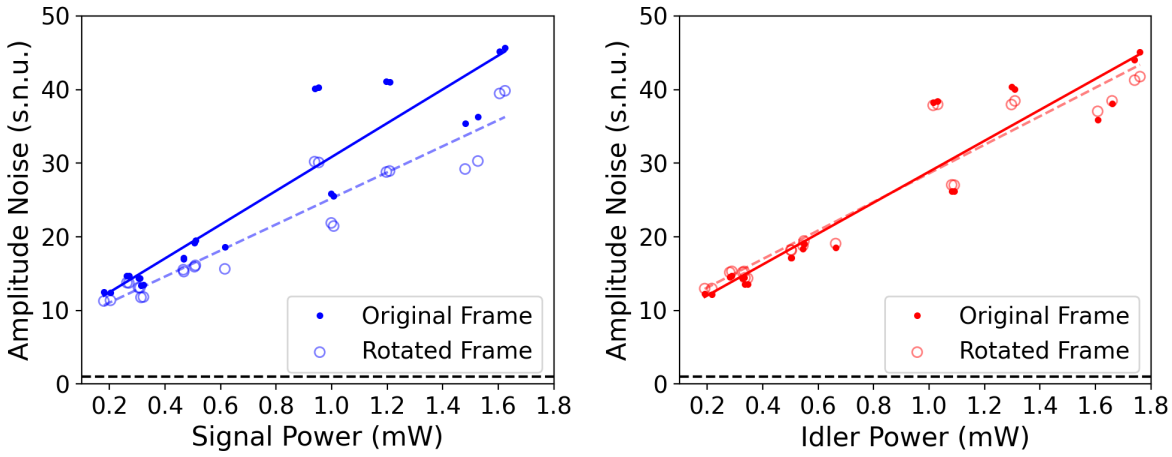


(a) (b)

Figure 4.19: Comparison of the amplitude noise between the original and the rotated frame for signal (a) and idler (b). The guiding lines are respective to the original frame (solid) and the rotated one (dashed).

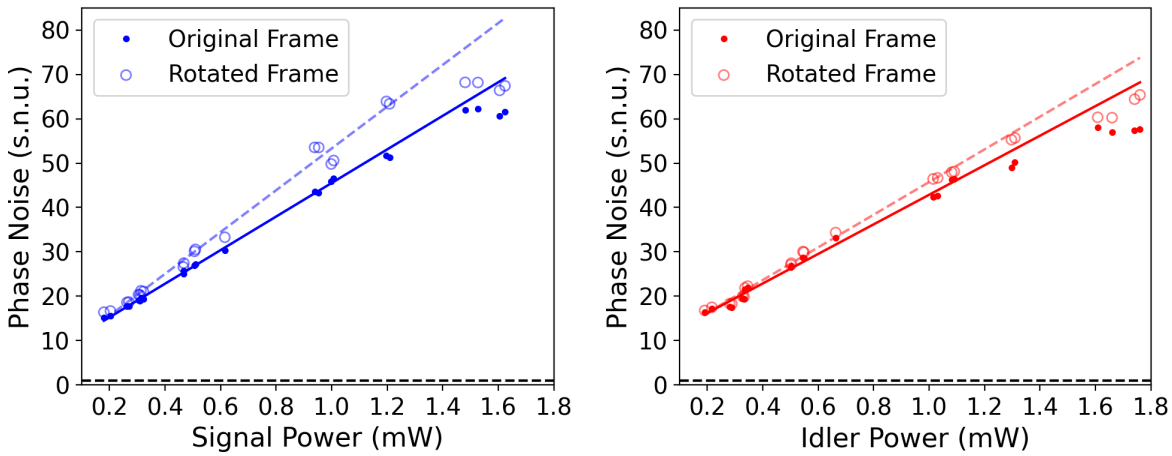


(a) (b)

Figure 4.20: Comparison of the phase noise between the original and the rotated frame for signal (a) and idler (b). The guiding lines are respective to the original frame (solid) and the rotated one (dashed).

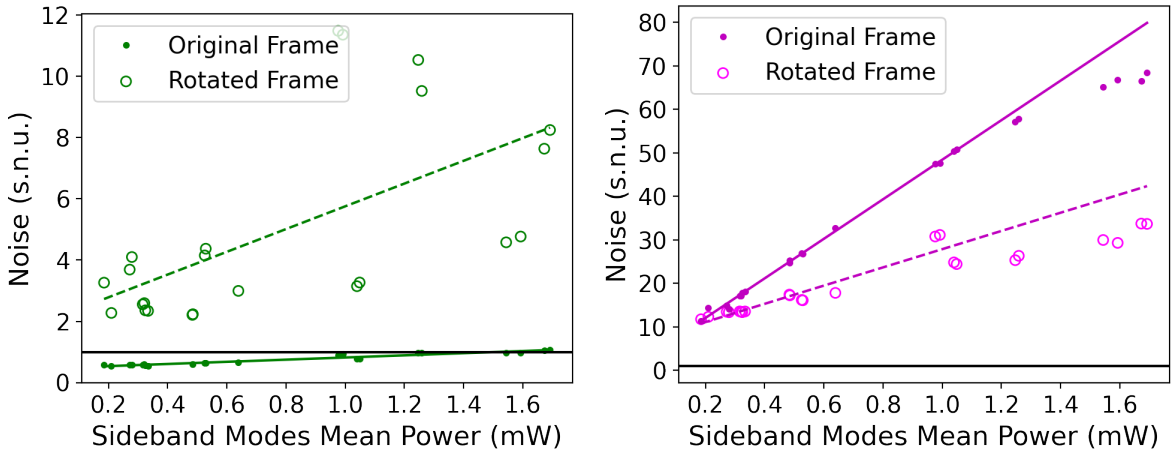


(a) (b)

Figure 4.21: Comparison of the amplitude subtraction and phase sum noises between the original and rotated frames. The amplitude squeezing is completely lost in the new frame.

• •

Several analysis were performed in the acquired data from the experimental system described in chapter 3. First, we checked the drastic reduction of the pump amplitude and phase fluctuations due to the filter cavity. The low noise pump field is very important to not introduce undesirable noise in the signal and idler fields. On the other hand, some excess of noise was still present due to the methods needed to control strong intensity fluctuations present in the filter cavity output.

The generated signal and idler fields by the OPO operating above threshold presented strong two-mode amplitude nonclassical correlations of up to $2.30 \pm 0.03$. We compared the amplitude squeezing using two different measurement methods in order to create confidence in our analysis. Very high fluctuations in the phase sum subspace was also observed. Furthermore, the expected degradation of squeezing and anti-squeezing with the introduction of optical losses was verified, which indicates that the measured nonclassical effect was not coming from possible electronic or computational artifacts.

When corrected for optical losses, we infer up to $4.9 \pm 0.7$ dB of on-chip amplitude squeezing. This value is bellow the expected 9.0 dB for the utilized microresonator, which is attributed to the pump excess of noise and the high phase noise that contaminates the amplitude quadrature owing to modulations induced by the third order nonlinear interactions. The high phase noise in the sum subspace, of $11.21 \pm 0.01$ dB ($13.2 \pm 0.5$ on-chip) for the same measurement of maximum squeezing, precluded any observation of entanglement.

We reconstructed the full four-mode covariance matrix of the state by simultaneously fitting equations (3.39) and (3.40) to six data sets acquired from a sequence of three measurements. Our analysis method allowed us to verify the validity of the errors generated by the computational routine applied. From the symplectic eigenvalues of the covariance matrix we guaranteed that the reconstructed state is physical and we quantified its highly mixed character. Moreover, the PPT criterion for quantum entanglement was applied in several bipartitions of the state. As expected from the excessive mixedness of the system, no evidence of entanglement was found.

We took advantage of the stability control of the experimental system to study how the covariance matrix change with increasing pump power. Enhancement of the amplitude and phase noise was observed for signal and idler. In this noisy regime, unbalances between the fields easily lead to the degradation of optical squeezing. In addition, phase modulation effects present in the $\chi^{(3)}$ dynamics mix the optical quadratures introducing

phase fluctuations in the amplitude quadrature. Another effect that may play an important role in the lack of robustness of amplitude squeezing is the distribution of energy to additional sideband modes due to the intracavity increasing power. The exploration of the quadrature noise and possible correlations between the additional fields are a subject of future research planned to be carried in the LMCAL.

We observed a fast growth of phase noise in the pump field as we increased the pump power while operating the OPO below threshold. The approximately linear tendency of the increasing phase fluctuations is in accordance to previous studies using second order nonlinear crystals [137]. Furthermore, thermorefractive effects were already evidenced in silicon nitride waveguides [138] and microresonators [139]. Hence, we do not discard the possibility of photon scattering by phonons to be responsible for this undesired excess of noise. As for the $\chi^{(2)}$ OPO, the cooling of the system may be a solution to mitigate this effect finally enabling the generation of bright two-mode entangled states from integrated $\chi^{(3)}$ OPOs operating above threshold.

# Conclusion

We reconstructed the covariance matrices of four-mode continuous variables states generated in an on-chip $\chi^{(3)}$ optical parametric oscillator operating above threshold. Up to our knowledge, this is the first full tomography of states generated in this condition. We reported the direct measurement of $2.30 \pm 0.03$ dB of amplitude difference squeezing, which reproduces previous results obtained for silicon nitride OPOs [110, 116]. Correcting to losses, we infer a total of $4.9 \pm 0.7$ dB of squeezing on-chip. This is the first integrated source of nonclassical light available in the LMCAL.

Nevertheless, observing entanglement remains a challenge, as enlightened by current results. The four-mode state is highly mixed with large excess of noise in the phase sum quadrature. Moreover, for stronger pump powers, the noise present in fields' quadratures increases and amplitude correlations are degraded as the dynamics of the system unbalances signal and idler. This lack of robustness of the $\chi^{(3)}$ amplitude correlations to variations of the pump intensity are in contrast to the $\chi^{(2)}$ scenario [15]. We expect that the origin of the excess of noise is of thermal nature [137–139]. Hence, cooling the chip may enable the measurement of entanglement in future work. Our results shine light on one of the bottlenecks hindering the deterministic generation of entangled states in silicon photonics OPOs. Investigations on the behavior of the pump noise as a function of temperature are currently being carried as the beginning of the next project of integrated OPOs in our laboratory.

Reducing the complexity of the covariance matrix, only considering the symmetrical basis, we identified cross correlations between different quadratures of the field. This effect is expected due to self- and cross-phase modulations present in $\chi^{(3)}$ nonlinear interactions [101]. With the mitigation of the excess of noise in the state we expect to observe better correlations on rotated frames, including entanglement, as theoretically predicted in [21].

Tripartite entanglement between signal, idler and pump is also predicted in [21]. Furthermore, secondary (or even further modes) modes are excited by enhancing the pump power, which also may present strong correlations [107]. Our system can be further expanded to include analysis cavities for the pump and the additional modes. Therefore,

the built experimental setup has potential to be employed in several future investigations to be carried in the LMCAL.

# Bibliography


[1] Antonio Acín, Immanuel Bloch, Harry Buhrman, Tommaso Calarco, Christopher Eichler, Jens Eisert, Daniel Esteve, Nicolas Gisin, Steffen J Glaser, Fedor Jelezko, et al. The quantum technologies roadmap: a European community view. *New Journal of Physics*, 20(8):080201, 2018.

[2] H Jeff Kimble. The quantum internet. *Nature*, 453(7198):1023, 2008.

[3] Hans-A Bachor and Timothy C Ralph. *A guide to experiments in quantum optics*. John Wiley & Sons, 2019.

[4] Daniel F Walls and Gerard J Milburn. *Quantum optics*. Springer Science & Business Media, 2007.

[5] Nicolas J Cerf, Gerd Leuchs, and Eugene S Polzik. *Quantum information with continuous variables of atoms and light*. World Scientific, 2007.

[6] Alexander I Lvovsky. Squeezed light. *Photonics: Scientific Foundations, Technology and Applications*, 1:121–163, 2015.

[7] Alessio Serafini. *Quantum continuous variables: a primer of theoretical methods*. CRC press, 2017.

[8] Benjamin J Lawrie, Paul D Lett, Alberto M Marino, and Raphael C Pooser. Quantum sensing with squeezed light. *ACS Photonics*, 6(6):1307–1318, 2019.

[9] Junaid Aasi, Joan Abadie, BP Abbott, Richard Abbott, TD Abbott, MR Abernathy, Carl Adams, Thomas Adams, Paolo Addesso, RX Adhikari, et al. Enhanced sensitivity of the LIGO gravitational wave detector by using squeezed states of light. *Nature Photonics*, 7(8):613–619, 2013.

[10] Olivier Pfister. Continuous-variable quantum computing in the quantum optical frequency comb. *Journal of Physics B: Atomic, Molecular and Optical Physics*, 53(1):012001, 2019.

[11] Robert Raussendorf and Hans J Briegel. A one-way quantum computer. *Physical Review Letters*, 86(22):5188, 2001.

[12] Jianwei Wang, Fabio Sciarrino, Anthony Laing, and Mark G Thompson. Integrated photonic quantum technologies. *Nature Photonics*, 14(5):273–284, 2020.

[13] Emanuele Pelucchi, Giorgos Fagas, Igor Aharonovich, Dirk Englund, Eden Figueroa, Qihuang Gong, Hübel Hannes, Jin Liu, Chao-Yang Lu, Nobuyuki Matsuda, et al. The potential and global outlook of integrated photonics for quantum technologies. *Nature Reviews Physics*, 4(3):194–208, 2022.

[14] AS Villar, LS Cruz, KN Cassemiro, M Martinelli, and P Nussenzveig. Generation of bright two-color continuous variable entanglement. *Physical review letters*, 95(24):243603, 2005.

[15] Alessandro S Villar, Katiúscia N Cassemiro, Kaled Dechoum, Antonio Z Khoury, Marcelo Martinelli, and Paulo Nussenzveig. Entanglement in the above-threshold optical parametric oscillator. *JOSA B*, 24(2):249–256, 2007.

[16] AS Coelho, FAS Barbosa, KN Cassemiro, AS Villar, M Martinelli, and P Nussenzveig. Three-color entanglement. *Science*, 326(5954):823–826, 2009.

[17] FAS Barbosa, AS Coelho, AJ De Faria, KN Cassemiro, AS Villar, P Nussenzveig, and M Martinelli. Robustness of bipartite Gaussian entangled beams propagating in lossy channels. *Nature Photonics*, 4(12):858–861, 2010.

[18] FAS Barbosa, Antonio Sales Coelho, LF Muñoz-Martínez, L Ortiz-Gutiérrez, AS Villar, P Nussenzveig, and M Martinelli. Hexapartite entanglement in an above-threshold optical parametric oscillator. *Physical review letters*, 121(7):073601, 2018.

[19] A Guerrero, RL Celis, P Nussenzveig, M Martinelli, AM Marino, and HM Florez. Continuous Variable Entanglement in an Optical Parametric Oscillator Based on a Nondegenerate Four Wave Mixing Process in Hot Alkali Atoms. *arXiv preprint arXiv:2204.02920*, 2022.

[20] M Martinelli, CL Garrido Alzar, PH Souto Ribeiro, and P Nussenzveig. Classical and quantum properties of optical parametric oscillators. *Brazilian journal of physics*, 31:597–615, 2001.

[21] C González-Arciniegas, Nicolas Treps, and P Nussenzveig. Third-order nonlinearity OPO: Schmidt mode decomposition and tripartite entanglement. *Optics letters*, 42(23):4865–4868, 2017.

[22] Amy C Turner, Christina Manolatou, Bradley S Schmidt, Michal Lipson, Mark A Foster, Jay E Sharping, and Alexander L Gaeta. Tailored anomalous group-velocity dispersion in silicon channel waveguides. *Optics express*, 14(10):4357–4362, 2006.

[23] TJ Kippenberg, SM Spillane, and KJ Vahala. Kerr-nonlinearity optical parametric oscillation in an ultrahigh-Q toroid microcavity. *Physical review letters*, 93(8):083904, 2004.

[24] Xingchen Ji, Felippe AS Barbosa, Samantha P Roberts, Avik Dutt, Jaime Cardenas, Yoshitomo Okawachi, Alex Bryant, Alexander L Gaeta, and Michal Lipson. Ultra-low-loss on-chip resonators with sub-milliwatt parametric oscillation threshold. *Optica*, 4(6):619–624, 2017.

[25] Felippe AS Barbosa, Antonio S Coelho, Katiuscia N Cassemiro, Paulo Nussenzveig, Claude Fabre, Alessandro S Villar, and Marcelo Martinelli. Quantum state reconstruction of spectral field modes: Homodyne and resonator detection schemes. *Physical Review A*, 88(5):052113, 2013.

[26] Felippe AS Barbosa, Antonio S Coelho, Katiuscia N Cassemiro, Paulo Nussenzveig, Claude Fabre, Marcelo Martinelli, and Alessandro S Villar. Beyond spectral homodyne detection: complete quantum measurement of spectral modes of light. *Physical review letters*, 111(20):200402, 2013.

[27] Michael A Nielsen and Isaac Chuang. Quantum computation and quantum information, 2002.

[28] Frank Arute, Kunal Arya, Ryan Babbush, Dave Bacon, Joseph C Bardin, Rami Barends, Rupak Biswas, Sergio Boixo, Fernando GSL Brandao, David A Buell, et al. Quantum supremacy using a programmable superconducting processor. *Nature*, 574(7779):505–510, 2019.

[29] Han-Sen Zhong, Hui Wang, Yu-Hao Deng, Ming-Cheng Chen, Li-Chao Peng, Yi-Han Luo, Jian Qin, Dian Wu, Xing Ding, Yi Hu, et al. Quantum computational advantage using photons. *Science*, 370(6523):1460–1463, 2020.

[30] Yulin Wu, Wan-Su Bao, Sirui Cao, Fusheng Chen, Ming-Cheng Chen, Xiawei Chen, Tung-Hsun Chung, Hui Deng, Yajie Du, Daojin Fan, et al. Strong quantum computational advantage using a superconducting quantum processor. *Physical review letters*, 127(18):180501, 2021.

[31] Lars S Madsen, Fabian Laudenbach, Mohsen Falamarzi Askarani, Fabien Rortais, Trevor Vincent, Jacob FF Bulmer, Filippo M Miatto, Leonhard Neuhaus, Lukas G Helt, Matthew J Collins, et al. Quantum computational advantage with a programmable photonic processor. *Nature*, 606(7912):75–81, 2022.

[32] Akira Furusawa, Jens Lykke Sørensen, Samuel L Braunstein, Christopher A Fuchs, H Jeff Kimble, and Eugene S Polzik. Unconditional quantum teleportation. *science*, 282(5389):706–709, 1998.

[33] Seth Lloyd and Samuel L Braunstein. Quantum computation over continuous variables. In *Quantum information with continuous variables*, pages 9–17. Springer, 1999.

[34] Ulrik L Andersen, Gerd Leuchs, and Christine Silberhorn. Continuous-variable quantum information processing. *Laser & Photonics Reviews*, 4(3):337–354, 2010.

[35] Gerardo Adesso, Sammy Ragy, and Antony R Lee. Continuous variable quantum information: Gaussian states and beyond. *Open Systems & Information Dynamics*, 21(01n02):1440001, 2014.

[36] John Williamson. On the algebraic problem concerning the normal forms of linear dynamical systems. *American journal of mathematics*, 58(1):141–163, 1936.

[37] Matteo GA Paris, Fabrizio Illuminati, Alessio Serafini, and Silvio De Siena. Purity of Gaussian states: Measurement schemes and time evolution in noisy channels. *Physical Review A*, 68(1):012314, 2003.

[38] Tania Golubeva, Yu Golubev, Claude Fabre, and Nicolas Treps. Quantum state of an injected TROPO above threshold: purity, Glauber function and photon number distribution. *The European Physical Journal D*, 46(1):179–193, 2008.

[39] Albert Einstein, Boris Podolsky, and Nathan Rosen. Can quantum-mechanical description of physical reality be considered complete? *Physical review*, 47(10):777, 1935.

[40] E. Schrödinger. Discussion of Probability Relations between Separated Systems. *Mathematical Proceedings of the Cambridge Philosophical Society*, 31(4):555–563, 1935.

[41] Niels Bohr. Can quantum-mechanical description of physical reality be considered complete? *Physical review*, 48(8):696, 1935.

[42] John S Bell. On the einstein podolsky rosen paradox. *Physics Physique Fizika*, 1(3):195, 1964.

[43] John S Bell. On the problem of hidden variables in quantum mechanics. *Reviews of Modern Physics*, 38(3):447, 1966.

[44] Reinhard F Werner and Michael M Wolf. Bound entangled Gaussian states. *Physical review letters*, 86(16):3658, 2001.

[45] Rajiah Simon. Peres-Horodecki separability criterion for continuous variable systems. *Physical Review Letters*, 84(12):2726, 2000.

[46] Lu-Ming Duan, Géza Giedke, Juan Ignacio Cirac, and Peter Zoller. Inseparability criterion for continuous variable systems. *Physical Review Letters*, 84(12):2722, 2000.

[47] Charles H Bennett, Gilles Brassard, Claude Crépeau, Richard Jozsa, Asher Peres, and William K Wootters. Teleporting an unknown quantum state via dual classical and Einstein-Podolsky-Rosen channels. *Physical review letters*, 70(13):1895, 1993.

[48] Holger F Hofmann, Toshiki Ide, Takayoshi Kobayashi, and Akira Furusawa. Fidelity and information in the quantum teleportation of continuous variables. *Physical Review A*, 62(6):062304, 2000.

[49] Akira Furusawa and Nobuyuki Takei. Quantum teleportation for continuous variables and related quantum information processing. *Physics reports*, 443(3):97–119, 2007.

[50] Marek Żukowski, Anton Zeilinger, Michael A Horne, and Artur K Ekert. "Event-ready-detectors"Bell experiment via entanglement swapping. *Physical Review Letters*, 71(26):4287, 1993.

[51] Peter Van Loock and Samuel L Braunstein. Unconditional teleportation of continuous-variable entanglement. *Physical Review A*, 61(1):010302, 1999.

[52] H-J Briegel, Wolfgang Dür, Juan I Cirac, and Peter Zoller. Quantum repeaters: the role of imperfect local operations in quantum communication. *Physical Review Letters*, 81(26):5932, 1998.

[53] J Eisert, DE Browne, S Scheel, and MB Plenio. Distillation of continuous-variable entanglement with optical means. *Annals of Physics*, 311(2):431–458, 2004.

[54] Nicolas Gisin, Grégoire Ribordy, Wolfgang Tittel, and Hugo Zbinden. Quantum cryptography. *Reviews of modern physics*, 74(1):145, 2002.

[55] Feihu Xu, Xiongfeng Ma, Qiang Zhang, Hoi-Kwong Lo, and Jian-Wei Pan. Secure quantum key distribution with realistic devices. *Reviews of Modern Physics*, 92(2):025002, 2020.

[56] Charles H Bennett and Gilles Brassard. Quantum cryptography: Public key distribution and coin tossing. *arXiv preprint arXiv:2003.06557*, 2020.

[57] Artur K Ekert. Quantum cryptography based on Bell's theorem. *Physical review letters*, 67(6):661, 1991.

[58] Timothy C Ralph. Security of continuous-variable quantum cryptography. *Physical Review A*, 62(6):062306, 2000.

[59] Ch Silberhorn, Natalia Korolkova, and Gerd Leuchs. Quantum key distribution with bright entangled beams. *Physical review letters*, 88(16):167902, 2002.

[60] Juan Yin, Yu-Huai Li, Sheng-Kai Liao, Meng Yang, Yuan Cao, Liang Zhang, Ji-Gang Ren, Wen-Qi Cai, Wei-Yue Liu, Shuang-Lin Li, et al. Entanglement-based secure quantum cryptography over 1,120 kilometres. *Nature*, 582(7813):501–505, 2020.

[61] Kejin Wei, Wei Li, Hao Tan, Yang Li, Hao Min, Wei-Jun Zhang, Hao Li, Lixing You, Zhen Wang, Xiao Jiang, et al. High-speed measurement-device-independent quantum key distribution with integrated silicon photonics. *Physical Review X*, 10(3):031030, 2020.

[62] S Tanzilli, Wolfgang Tittel, Hugues De Riedmatten, Hugo Zbinden, Paolo Baldi, M DeMicheli, Da B Ostrowsky, and Nicolas Gisin. PPLN waveguide for quantum communication. *The European Physical Journal D-Atomic, Molecular, Optical and Plasma Physics*, 18(2):155–160, 2002.

[63] H Jin, FM Liu, P Xu, JL Xia, ML Zhong, Y Yuan, JW Zhou, YX Gong, W Wang, and SN Zhu. On-chip generation and manipulation of entangled photons based on reconfigurable lithium-niobate waveguide circuits. *Physical review letters*, 113(10):103601, 2014.

[64] Jie Zhao, Chaoxuan Ma, Michael Rüsing, and Shayan Mookherjea. High quality entangled photon pair generation in periodically poled thin-film lithium niobate waveguides. *Physical review letters*, 124(16):163603, 2020.

[65] Ken-ichi Harada, Hiroki Takesue, Hiroshi Fukuda, Tai Tsuchizawa, Toshifumi Watanabe, Koji Yamada, Yasuhiro Tokura, and Sei-ichi Itabashi. Generation of high-purity entangled photon pairs using silicon wire waveguide. *Optics express*, 16(25):20368–20373, 2008.

[66] Joshua W Silverstone, Raffaele Santagati, Damien Bonneau, Michael J Strain, Marc Sorel, Jeremy L O'Brien, and Mark G Thompson. Qubit entanglement between ring-resonator photon-pair sources on a silicon chip. *Nature communications*, 6(1):1–7, 2015.

[67] Liangliang Lu, Lijun Xia, Zhiyu Chen, Leizhen Chen, Tonghua Yu, Tao Tao, Wenchao Ma, Ying Pan, Xinlun Cai, Yanqing Lu, et al. Three-dimensional entanglement on a silicon chip. *npj Quantum Information*, 6(1):1–9, 2020.

[68] Sven Ramelow, Alessandro Farsi, Stéphane Clemmen, Daniel Orquiza, Kevin Luke, Michal Lipson, and Alexander L Gaeta. Silicon-nitride platform for narrowband entangled photon generation. *arXiv preprint arXiv:1508.04358*, 2015.

[69] Poolad Imany, Jose A Jaramillo-Villegas, Ogaga D Odele, Kyunghun Han, Daniel E Leaird, Joseph M Lukens, Pavel Lougovski, Minghao Qi, and Andrew M Weiner. 50-GHz-spaced comb of high-dimensional frequency-bin entangled photons from an on-chip silicon nitride microresonator. *Optics express*, 26(2):1825–1840, 2018.

[70] Xiyuan Lu, Qing Li, Daron A Westly, Gregory Moille, Anshuman Singh, Vikas Anant, and Kartik Srinivasan. Chip-integrated visible–telecom entangled photon pair source for quantum communication. *Nature physics*, 15(4):373–381, 2019.

[71] Rolf T Horn, Piotr Kolenderski, Dongpeng Kang, Payam Abolghasem, Carmelo Scarcella, Adriano Della Frera, Alberto Tosi, Lukas G Helt, Sergei V Zhukovsky, John E Sipe, et al. Inherent polarization entanglement generated from a monolithic semiconductor chip. *Scientific reports*, 3(1):1–5, 2013.

[72] Jianwei Wang, Alberto Santamato, Pisu Jiang, Damien Bonneau, Erman Engin, Joshua W Silverstone, Matthias Lermer, Johannes Beetz, Martin Kamp, Sven Höfling, et al. Gallium arsenide (GaAs) quantum photonic waveguide circuits. *Optics Communications*, 327:49–55, 2014.

[73] Trevor J Steiner, Joshua E Castro, Lin Chang, Quynh Dang, Weiqiang Xie, Justin Norman, John E Bowers, and Galan Moody. Ultrabright Entangled-Photon-Pair Generation from an Al Ga As-On-Insulator Microring Resonator. *PRX Quantum*, 2(1):010337, 2021.

[74] Philip Sibson, Chris Erven, Mark Godfrey, Shigehito Miki, Taro Yamashita, Mikio Fujiwara, Masahide Sasaki, Hirotaka Terai, Michael G Tanner, Chandra M Natarajan, et al. Chip-based quantum key distribution. *Nature communications*, 8(1):1–6, 2017.

[75] Daniel Llewellyn, Yunhong Ding, Imad I Faruque, Stefano Paesani, Davide Bacco, Raffaele Santagati, Yan-Jun Qian, Yan Li, Yun-Feng Xiao, Marcus Huber, et al. Chip-to-chip quantum teleportation and multi-photon entanglement in silicon. *Nature Physics*, 16(2):148–153, 2020.

[76] Henry Semenenko, Philip Sibson, Andy Hart, Mark G Thompson, John G Rarity, and Chris Erven. Chip-based measurement-device-independent quantum key distribution. *Optica*, 7(3):238–242, 2020.

[77] Caterina Vigliar, Stefano Paesani, Yunhong Ding, Jeremy C. Adcock, Jianwei Wang, Sam Morley-Short, Davide Bacco, Leif K. Oxenløwe, Mark G. Thompson, John G. Rarity, and Anthony Laing. Error-protected qubits in a silicon photonic chip. *Nature Physics*, 17(10):1745–2481, 2021.

[78] Jintian Lin, Fang Bo, Ya Cheng, and Jingjun Xu. Advances in on-chip photonic devices based on lithium niobate on insulator. *Photonics Research*, 8(12):1910–1936, 2020.

[79] Xiaojiong Chen, Zhaorong Fu, Qihuang Gong, and Jianwei Wang. Quantum entanglement on photonic chips: a review. *Advanced Photonics*, 3(6):064002, 2021.

[80] Genta Masada, Kazunori Miyata, Alberto Politi, Toshikazu Hashimoto, Jeremy L O'brien, and Akira Furusawa. Continuous-variable entanglement on a chip. *Nature Photonics*, 9(5):316, 2015.

[81] Genta Masada and Akira Furusawa. On-chip continuous-variable quantum entanglement. *Nanophotonics*, 5(3):469–482, 2016.

[82] Daniel J Blumenthal, Rene Heideman, Douwe Geuzebroek, Arne Leinse, and Chris Roeloffzen. Silicon nitride in silicon photonics. *Proceedings of the IEEE*, 106(12):2209–2231, 2018.

[83] Kevin Luke, Yoshitomo Okawachi, Michael RE Lamont, Alexander L Gaeta, and Michal Lipson. Broadband mid-infrared frequency comb generation in a $Si_3N_4$ microresonator. *Optics letters*, 40(21):4823–4826, 2015.

[84] Kazuhiro Ikeda, Robert E Saperstein, Nikola Alic, and Yeshaiahu Fainman. Thermal and Kerr nonlinear properties of plasma-deposited silicon nitride/silicon dioxide waveguides. *Optics express*, 16(17):12987–12994, 2008.

[85] Ruifang Dong, Joel Heersink, Joel F Corney, Peter D Drummond, Ulrik L Andersen, and Gerd Leuchs. Experimental evidence for Raman-induced limits to efficient squeezing in optical fibers. *Optics letters*, 33(2):116–118, 2008.

[86] Kevin Luke, Avik Dutt, Carl B Poitras, and Michal Lipson. Overcoming $Si_3N_4$ film stress limitations for high quality factor ring resonators. *Optics express*, 21(19):22829–22833, 2013.

[87] S Zhu, AW Yu, D Hawley, and R Roy. Frustrated total internal reflection: a demonstration and review. *American Journal of Physics*, 54(7):601–607, 1986.

[88] Amnon Yariv. Universal relations for coupling of optical power between microresonators and dielectric waveguides. *Electronics letters*, 36(4):321–322, 2000.

[89] Amnon Yariv. Critical coupling and its control in optical waveguide-ring resonator systems. *IEEE Photonics Technology Letters*, 14(4):483–485, 2002.

[90] Hermann A Haus. *Waves and fields in optoelectronics*. Prentice-Hall,, 1984.

[91] AA Savchenkov, AB Matsko, M Mohageg, DV Strekalov, and L Maleki. Parametric oscillations in a whispering gallery resonator. *Optics letters*, 32(2):157–159, 2007.

[92] Andrey B Matsko, Anatoliy A Savchenkov, Dmitry Strekalov, Vladimir S Ilchenko, and Lute Maleki. Optical hyperparametric oscillations in a whispering-gallery-mode resonator: Threshold and phase diffusion. *Physical Review A*, 71(3):033804, 2005.

[93] Luca Razzari, David Duchesne, Marcello Ferrera, Roberto Morandotti, S Chu, BE Little, and DJ Moss. CMOS-compatible integrated optical hyper-parametric oscillator. *Nature Photonics*, 4(1):41–45, 2010.

[94] Tobias J Kippenberg, Alexander L Gaeta, Michal Lipson, and Michael L Gorodetsky. Dissipative Kerr solitons in optical microresonators. *Science*, 361(6402), 2018.

[95] Alexander L Gaeta, Michal Lipson, and Tobias J Kippenberg. Photonic-chip-based frequency combs. *nature photonics*, 13(3):158–169, 2019.

[96] Yanne K Chembo and Curtis R Menyuk. Spatiotemporal Lugiato-Lefever formalism for Kerr-comb generation in whispering-gallery-mode resonators. *Physical Review A*, 87(5):053852, 2013.

[97] Yanne K Chembo. Quantum dynamics of Kerr optical frequency combs below and above threshold: Spontaneous four-wave mixing, entanglement, and squeezed states of light. *Physical Review A*, 93(3):033820, 2016.

[98] Tobias Hansson and Stefan Wabnitz. Frequency comb generation beyond the Lugiato–Lefever equation: multi-stability and super cavity solitons. *JOSA B*, 32(7):1259–1266, 2015.

[99] Robert W Boyd. *Nonlinear optics*. Elsevier, 2003.

[100] Jacob S Levy, Mark A Foster, Alexander L Gaeta, and Michal Lipson. Harmonic generation in silicon nitride ring resonators. *Optics express*, 19(12):11415–11421, 2011.

[101] Giulia Ferrini, I Fsaifes, T Labidi, F Goldfarb, Nicolas Treps, and F Bretenaker. Symplectic approach to the amplification process in a nonlinear fiber: role of signal-idler correlations and application to loss management. *JOSA B*, 31(7):1627–1641, 2014.

[102] Mark A Foster, Amy C Turner, Jay E Sharping, Bradley S Schmidt, Michal Lipson, and Alexander L Gaeta. Broad-band optical parametric gain on a silicon photonic chip. *Nature*, 441(7096):960, 2006.

[103] Avik Dutt. *On-chip quantum and nonlinear optics: from squeezing to spectroscopy*. PhD thesis, Cornell University, 2017.

[104] Tryggve Bååk. Silicon oxynitride; a material for GRIN optics. *Applied optics*, 21(6):1069–1072, 1982.

[105] Ardavan F Oskooi, David Roundy, Mihai Ibanescu, Peter Bermel, John D Joannopoulos, and Steven G Johnson. MEEP: A flexible free-software package for electromagnetic simulations by the FDTD method. *Computer Physics Communications*, 181(3):687–702, 2010.

[106] Vilson R Almeida and Michal Lipson. Optical bistability on a silicon chip. *Optics letters*, 29(20):2387–2389, 2004.

[107] Carlos Andres Gonzalez Arciniegas. *Properties of the light emitted by a silicon on-chip optical parametric oscillator (OPO)*. PhD thesis, Universidade de São Paulo, 2017.

[108] Leonard Mandel and Emil Wolf. *Optical coherence and quantum optics*. Cambridge university press, 1995.

[109] M Brambilla, F Castelli, LA Lugiato, F Prati, and G Strini. Nondegenerate four-wave mixing in a cavity: instabilities and quantum noise reduction. *Optics communications*, 83(5-6):367–389, 1991.

[110] Avik Dutt, Kevin Luke, Sasikanth Manipatruni, Alexander L Gaeta, Paulo Nussenzveig, and Michal Lipson. On-chip optical squeezing. *Physical Review Applied*, 3(4):044005, 2015.

[111] Yun Zhao, Xingchen Ji, Bok Young Kim, Prathamesh S Donvalkar, Jae K Jang, Chaitanya Joshi, Mengjie Yu, Chaitali Joshi, Renato R Domeneguetti, Felippe AS Barbosa, et al. Visible nonlinear photonics via high-order-mode dispersion engineering. *Optica*, 7(2):135–141, 2020.

[112] Zhenghao Yin, Kenta Sugiura, Hideaki Takashima, Ryo Okamoto, Feng Qiu, Shiyoshi Yokoyama, and Shigeki Takeuchi. Frequency correlated photon generation at telecom band using silicon nitride ring cavities. *Optics Express*, 29(4):4821–4829, 2021.

[113] Nicholas C Harris, Gregory R Steinbrecher, Mihika Prabhu, Yoav Lahini, Jacob Mower, Darius Bunandar, Changchen Chen, Franco NC Wong, Tom Baehr-Jones, Michael Hochberg, et al. Quantum transport simulations in a programmable nanophotonic processor. *Nature Photonics*, 11(7):447–452, 2017.

[114] Xiaogang Qiang, Xiaoqi Zhou, Jianwei Wang, Callum M Wilkes, Thomas Loke, Sean O'Gara, Laurent Kling, Graham D Marshall, Raffaele Santagati, Timothy C Ralph, et al. Large-scale silicon quantum photonics implementing arbitrary two-qubit processing. *Nature photonics*, 12(9):534–539, 2018.

[115] Renato R Domeneguetti, Yun Zhao, Xingchen Ji, Marcelo Martinelli, Michal Lipson, Alexander L Gaeta, and Paulo Nussenzveig. Parametric sideband generation in CMOS-compatible oscillators from visible to telecom wavelengths. *Optica*, 8(3):316–322, 2021.

[116] Avik Dutt, Steven Miller, Kevin Luke, Jaime Cardenas, Alexander L Gaeta, Paulo Nussenzveig, and Michal Lipson. Tunable squeezing using coupled ring resonators on a silicon nitride chip. *Optics letters*, 41(2):223–226, 2016.

[117] Varun D Vaidya, B Morrison, LG Helt, R Shahrokshahi, DH Mahler, MJ Collins, K Tan, J Lavoie, A Repingon, M Menotti, et al. Broadband quadrature-squeezed vacuum and nonclassical photon number correlations from a nanophotonic device. *Science advances*, 6(39):eaba9186, 2020.

[118] Zijiao Yang, Mandana Jahanbozorgi, Dongin Jeong, Shuman Sun, Olivier Pfister, Hansuek Lee, and Xu Yi. Microresonator-based squeezed optical frequency comb. In *2021 IEEE Photonics Conference (IPC)*, pages 1–2. IEEE, 2021.

[119] Yun Zhao, Yoshitomo Okawachi, Jae K Jang, Xingchen Ji, Michal Lipson, and Alexander L Gaeta. Near-degenerate quadrature-squeezed vacuum generation on a silicon-nitride chip. *Physical Review Letters*, 124(19):193601, 2020.

[120] Y Zhang, M Menotti, K Tan, VD Vaidya, DH Mahler, LG Helt, L Zatti, M Liscidini, B Morrison, and Z Vernon. Squeezed light from a nanophotonic molecule. *Nature communications*, 12(1):1–6, 2021.

[121] Robert Cernansky and Alberto Politi. Nanophotonic source of quadrature squeezing via self-phase modulation. *APL Photonics*, 5(10):101303, 2020.

[122] Jaime Cardenas, Carl B Poitras, Kevin Luke, Lian-Wee Luo, Paul Adrian Morton, and Michal Lipson. High coupling efficiency etched facet tapers in silicon waveguides. *IEEE Photonics Technology Letters*, 26(23):2380–2382, 2014.

[123] Alessandro S Villar. The conversion of phase to amplitude fluctuations of a light beam by an optical cavity. *American Journal of Physics*, 76(10):922–929, 2008.

[124] Pablo Jaime Palacios Avila. *Fonte de luz coerente na banda C de telecomunicações e uso em chips de* $Si_3N_4$. PhD thesis, Universidade de São Paulo, 2018.

[125] TW Hansch and B Couillaud. Laser frequency stabilization by polarization spectroscopy of a reflecting reference cavity. *Optics communications*, 35(3):441–444, 1980.

[126] Vilson R Almeida, Roberto R Panepucci, and Michal Lipson. Nanotaper for compact mode conversion. *Optics letters*, 28(15):1302–1304, 2003.

[127] Antonio R Zanatta and Ivan B Gallo. The thermo optic coefficient of amorphous SiN films in the near-infrared and visible regions and its experimental determination. *Applied Physics Express*, 6(4):042402, 2013.

[128] D Geuzebroek, EJ Klein, H Kelderman, and A Driessen. Wavelength tuning and switching of a thermooptic microring resonator. In *proc. ECIO*, volume 395. Citeseer, 2003.

[129] William MJ Green, Hendrik F Hamann, Lidija Sekaric, Michael J Rooks, and Yurii A Vlasov. Ultra-compact reconfigurable silicon optical devices using micron-scale localized thermal heating. In *OFC/NFOEC 2007-2007 Conference on Optical Fiber Communication and the National Fiber Optic Engineers Conference*, pages 1–3. IEEE, 2007.

[130] Tulio Brito Brasil, Valeriy Novikov, Hugo Kerdoncuff, Mikael Lassen, and Eugene Polzik. Two-colour high-purity Einstein-Podolsky-Rosen photonic state. *arXiv preprint arXiv:2110.00066*, 2021.

[131] Roy J Glauber. The quantum theory of optical coherence. *Physical Review*, 130(6):2529, 1963.

[132] Harry Nyquist. Thermal agitation of electric charge in conductors. *Physical review*, 32(1):110, 1928.

[133] Herwig Kogelnik and Tingye Li. Laser beams and resonators. *Applied optics*, 5(10):1550–1567, 1966.

[134] Fei Liu, Lijuan Gu, Shangran Xie, Xiangge He, Duo Yi, Min Zhang, and Qingchang Tao. Acousto-optic modulation induced noises on heterodyne-interrogated interferometric fiber-optic sensors. *Journal of Lightwave Technology*, 36(16):3465–3471, 2018.

[135] Matt Newville, Renee Otten, Andrew Nelson, Antonino Ingargiola, Till Stensitzki, Dan Allan, Austin Fox, Faustin Carter, Michał, Glenn, Yoav Ram, MerlinSmiles, Li Li, Christoph Deil, Stuermer, Alexandre Beelen, Oliver Frost, gpasquev, Allan L. R. Hansen, Alexander Stark, Tim Spillane, Shane Caldwell, Anthony Polloreno, andrewhannum, Jose Borreguero, Jonathan Fraine, deep 42-thought, Benjamin F. Maier, Ben Gamari, and Anthony Almarza. lmfit/lmfit-py 0.9.12. November 2018.

[136] FAS Barbosa, AS Coelho, KN Cassemiro, M Martinelli, P Nussenzveig, and AS Villar. Assumption-free measurement of the quantum state of light: Exploring the sidebands of intense fields. *Physical Review A*, 102(6):063705, 2020.

[137] JES César, AS Coelho, KN Cassemiro, AS Villar, M Lassen, P Nussenzveig, and M Martinelli. Extra phase noise from thermal fluctuations in nonlinear optical crystals. *Physical Review A*, 79(6):063816, 2009.

[138] Nicolas Le Thomas, Ashim Dhakal, Ali Raza, Frédéric Peyskens, and Roel Baets. Impact of fundamental thermodynamic fluctuations on light propagating in photonic waveguides made of amorphous materials. *Optica*, 5(4):328–336, 2018.

[139] Guanhao Huang, Erwan Lucas, Junqiu Liu, Arslan S Raja, Grigory Lihachev, Michael L Gorodetsky, Nils J Engelsen, and Tobias J Kippenberg. Thermorefractive noise in silicon-nitride microresonators. *Physical Review A*, 99(6):061801, 2019.